

ABSTRACT

Title of Document: AN OPTICAL MEMS SENSOR FOR ON-CHIP
CATECHOL DETECTION

Peter Hume Dykstra, Master of Science, 2008

Directed By: Professor Reza Ghodssi
Department of Electrical and Computer Engineering
The Institute for Systems Research

This thesis reports the successful design, fabrication and testing of an optical MEMS sensor for the detection of the toxic phenol, catechol. Catechol's presence in food and drinking water poses a health concern due to its harmful effects on cell respiration. By-products of catechol oxidation have demonstrated increased absorbance changes in a chitosan film in the UV and near UV range. Our reported sensor utilizes patterned SU-8 waveguides and a microfluidic channel to deliver catechol samples to an electrodeposited chitosan film for absorbance measurements at 472 nm. Concentrations as low as 1 mM catechol are detected while control experiments including ascorbic acid display no measurable response. By using optical detection methods, our device does not suffer from many of the problems which plague conventional electrochemical based sensors.

AN OPTICAL MEMS SENSOR FOR ON-CHIP CATECHOL DETECTION

By

Peter Hume Dykstra

Thesis submitted to the Faculty of the Graduate School of the
University of Maryland, College Park, in partial fulfillment
of the requirements for the degree of
Master of Science
2008

Advisory Committee:
Professor Reza Ghodssi, Chair
Professor Gregory Payne
Professor Christopher Davis

© Copyright by
Peter Hume Dykstra
2008

Dedication

To my family and my fiancé Laura for everything

Acknowledgements

First off, I would like to thank my advisor, Professor Reza Ghodssi, for supporting this research and lending his guidance over the past two years. His direction made this work possible.

I would also like to thank the staff of the Maryland Fablab facility, Jonathan Hummel, John Abrahams, Tom Loughran and Bill O’Conner for their immeasurable assistance with the tools used during the fabrication process. This work would not have been possible without their help.

I also extend thanks to my collaborators on this research, Prof. Gregory Payne and Prof. Liangli Yu for their guidance and support. I also thank the National Science Foundation (NSF) and the R. W. Deutsch Foundation for funding this research. A very special thanks goes to George Hao for assisting me with many of my experiments and procedures.

I would also like to especially thank my colleague, Stephan Koev, who has acted as my mentor during the past few years. Many aspects of this project were supported with Stephan’s help and I cannot thank him enough for everything that he has done for me.

Last but not least, I would like to thank all of my colleagues at the MEMS Sensors and Actuators Lab (MSAL) for their support.

Table of Contents

Dedication	ii
Acknowledgements	iii
Table of Contents	iv
List of Tables	vi
List of Figures	vii
1 Introduction and Motivation	1
1.1 Traditional Biophotonics Techniques	2
1.1.1 Fluorescence	2
1.1.2 Bioluminescence	3
1.1.3 Absorbance	4
1.2 Catechol Detection.....	5
1.2.1 Phenols	6
1.2.2 Electrochemical Detection	8
1.2.3 Optical Detection	10
1.3 Lab-on-a-Chip Devices	12
1.3.1 MEMS Technology.....	12
1.3.2 Optical Integration in MEMS	13
1.3.3 Microfluidics	15
1.4 Biofunctionalization.....	17
1.4.1 Traditional Techniques	17
1.4.2 Chitosan Patterning Techniques	19
1.4.3 Amine conjugation.....	21
2 Device Design.....	22
2.1 Design Iterations	22
2.1.1 Previous Research.....	23
2.1.2 Absorbance Test Chip Design	24
2.1.3 Final Microfluidic Design.....	26
2.2 Waveguides.....	28
2.2.1 Materials	29
2.2.2 Light Propagation and Loss	32
2.2.3 Facet Roughness	39
2.3 Channel Design.....	41
2.4 Electrode Design.....	42
2.4.1 Cr/Au Electrodes.....	42
2.4.2 Indium Tin Oxide (ITO) Sidewall	44
2.5 Fiber Clamp Structures	46

3	Device Fabrication	48
3.1	Process Flow	48
3.2	Electrode Patterning.....	52
3.3	SU-8 Recipe Development	53
3.3.1	SU-8 Uniformity	54
3.3.2	SU-8 Adhesion.....	56
3.4	ITO Patterning	59
3.4.1	AZ9245 Sidewall Profile	60
3.4.2	ITO Conductivity	61
3.5	Die-level Processes	63
3.5.1	Chitosan Deposition.....	63
3.5.2	PDMS Bonding	66
3.5.3	Optical Fiber Preparation.....	67
4	Testing and Results	68
4.1	Slide Absorbance	68
4.1.1	Testing Apparatus	68
4.1.2	Slide Absorbance Results	70
4.2	MEMS Sensor Testing.....	73
4.2.1	Testing Apparatus	73
4.2.2	Total Optical Loss	75
4.2.3	Preliminary Optical Testing.....	77
4.2.4	Catechol Detection Results	80
5	Discussion	86
5.1	Data Discrepancies.....	86
5.1.1	Electrode Area Variations.....	86
5.1.2	Flow Rate Dependence	87
5.1.3	Metal Contamination	88
5.2	Sensor Comparison	89
6	Conclusion & Future Work.....	91
	APPENDIX.....	94
	REFERENCES	97

List of Tables

Table 2.1: Dimensions of important device structures.	28
Table 2.2: Reflection at interfaces	33
Table 3.1: Device process flow	48
Table 3.2: Metal Sputtering Conditions.....	52
Table 3.3: Metal Patterning Procedure	53
Table 3.4: SU-8 recipe	54
Table 3.5: Recipe for AZ9245 photoresist and ITO patterning	59
Table 4.1: Power budget through the device.	76

List of Figures

Figure 1.1: (a) Fluorescence through promotion of an electron to a higher energy state. (b) Demonstration of the Stokes Shift between absorbed and emitted light	3
Figure 1.2: The molecular structure of (a) phenol, (b) catechol and (c) caffeic acid which is found in many fruits and vegetables.....	6
Figure 1.3: Catechol becomes an o-quinone following oxidation and is reverted back to its original form following reduction.....	8
Figure 1.4: Catechol from solution diffuses through the polymer matrix and is oxidized by the PPO enzyme then reduced at the electrode surface [25].	10
Figure 1.5: Chitosan films patterned through catechol oxidation. The dark areas are due to the absorbing O-quinones present [31].	11
Figure 1.6: Photo of device displaying on-chip integration of a dye laser, SU-8 waveguides, fluid channel and photodiodes for light intensity detection [39].	14
Figure 1.7: (a) Photoresist is patterned onto a blank wafer to create the mold. (b) PDMS is cured over the mold and lifted off (c). The PDMS is plasma bonded to a glass substrate (d).....	16
Figure 1.8: Antibody with labeled Fc and Fab regions. Only the molecules specifically coded for the particular antibody will bind as shown in the figure.	18
Figure 1.9: Chitosan structure in both its soluble and insoluble forms [71].....	19
Figure 1.10: Electrodeposition of chitosan occurs at the surface of a negatively biased cathode due to the increase of the pH above the pKa value [78]......	20
Figure 2.1: 3-D schematic of early biophotonics device [80]. Excitation light is delivered top-down while the waveguide collects the resulting fluorescence and scattered excitation.....	23
Figure 2.2: Mask design for test chips using L-Edit software. Green: SU-8, Brown: Gold, Grey: ITO.....	25
Figure 2.3: Picture of test chip demonstrating the in-plane coupling of red light at 633 nm.	25
Figure 2.4: L-edit mask design of the final microfluidic device. The chip size is 32 mm x 24.4 mm. Green: SU-8, Brown: Gold, Grey: ITO	27

Figure 2.5: 3-d schematic of the final device used for absorbance testing through the chitosan film.....	28
Figure 2.6: Cross section of strip SU-8 waveguide showing the different cladding materials. Note that the SU-8 index is higher than that of the cladding which allows it to act as a waveguide.	29
Figure 2.7: Transmittance of SU-8 films from UV to near IR [87].....	31
Figure 2.8: Coupling efficiency vs waveguide width assuming a channel length of 300 μm and a propagating wavelength of 472 nm.....	36
Figure 2.9: Digital photo of blue light attenuation through an SU-8 waveguide.	38
Figure 2.10: Exponential decay of light intensity as it propagates through the SU-8 waveguide.	38
Figure 2.11: SEM image of the input waveguide facet displaying the roughness.....	40
Figure 2.12: Side view of channel with control and sensing electrodes shown. The ITO film is patterned over the sensing electrode and up the wall.	43
Figure 2.13: Attenuation of light through ITO based on wavelength. Data is used from [97].	45
Figure 2.14: Fiber clamp structure shown with optical fiber placed in the groove. ...	46
Figure 3.1: Fully packaged device	52
Figure 3.2: (a) end of fiber clamp on a Pyrex wafer showing SU-8 residues in the channel and (b) the same area on a silicon wafer showing clean channels.	56
Figure 3.3: Discoloration around the edges of the SU-8 signifies poor adhesion.	58
Figure 3.4: SEM image of an SU-8 sidewall displaying the adhesion crack between the resist and the wafer that has formed.....	58
Figure 3.5: SEM displaying patterned photoresist on the sidewall.	60
Figure 3.6: SEM image of ITO patterned on the SU-8 sidewall.	61
Figure 3.7: IV plots for ITO strips 240 μm x 2000 μm with and without the adhesion promoter present on the wafer.	62
Figure 3.8: SEM images of chitosan deposition with an applied current of (a) 0.35 μA , (b) 0.5 μA , (c) 1.0 μA and (d) 1.5 μA for a 10 minute reaction time.	65

Figure 3.9: Microscope image of sidewall focused at the top of the SU-8 resist (a) before and (b) after chitosan deposition.....	66
Figure 4.1: Red circles indicate the location of the chitosan film on both (a) the ITO slide and (b) within the full testing setup.....	69
Figure 4.2: Absorbance spectrums taken through chitosan films conjugated with o-quinones from catechol oxidation for various times.....	70
Figure 4.3: Absorbance through chitosan film for different reaction times at a wavelength of 472 nm.....	71
Figure 4.4: Absorbance spectrums through chitosan films subjected to various catechol concentrations.....	72
Figure 4.5: Absorbance vs catechol concentration at 472 nm displaying a linear-like response.....	73
Figure 4.6: Block diagram of testing setup for the MEMS sensor.	74
Figure 4.7: Photo showing full testing setup.	75
Figure 4.8: Intensity of the blue laser is shown as a clear peak with a narrow spectral width centered at 472 nm.....	77
Figure 4.9: Intensity of laser over one hour period after laser has been switched on.	78
Figure 4.10: Measured intensity through device showing no difference between buffer solutions with and without catechol.....	80
Figure 4.11: Absorbance over time results for various catechol concentrations and control solutions.....	81
Figure 4.12: Decrease in laser intensity after 10 minute oxidation reaction. Note the difference chitosan makes for the catechol solutions while the control solutions are unaffected.....	82
Figure 4.13: Absorbance vs. concentration plot displaying the non-linear relationship between the two.	83
Figure 4.14: Intensity change from the oxidation of 0.1 M catechol in the absence of chitosan. The detection displays high repeatability.	84
Figure 4.15: Absorbance over time using devices without the chitosan film for various catechol concentrations.	85

Figure 5.1: Absorbance spectra for a chitosan film neutralized in the presence of aluminum foil..... 88

Figure 6.1: Cross section of alternate device design to reduce device variability..... 92

1 Introduction and Motivation

This thesis presents the design, fabrication and testing of a MEMS chemical sensor for the detection of the phenol catechol. The sensor demonstrates a fully enclosed, microfluidic device that uses in-plane light coupling for interrogation. The in-plane nature of the device is desired as it allows for the possible future integration of on-chip detectors for the transduction of the light signal to a voltage.

The motivation behind the work involves addressing the need for monitoring the safety of the world's food and water supply. As industry grows around the world, the waste that is created can contaminate the water supply. This is even more of a problem in developing countries where water filtration systems are not as efficient as those in the United States. Certain phenols like catechol are common pollutants from factories and can have hazardous health effects if consumed. Although laboratory analysis can be performed on water samples to achieve accurate data regarding the contents, the work is expensive, time consuming and requires multiple trained personnel. One promising solution is to have portable, cheap sensors that can give information regarding the concentration of specific contaminants to the user on-site. The device covered in this thesis delivers one of these possible solutions by providing a portable, easy-to-use device for catechol detection in liquid samples.

The thesis is organized in such a way so as to first cover the basics of biophotonics, catechol, and lab-on-a-chip devices. The design and fabrication steps of the reported MEMS biosensor follows with an emphasis on what has been added to the prior generations of this platform. The testing and results sections will compare data obtained from the device and data obtained from larger scale experiments. The

conclusion will include the future work that is planned to further increase the effectiveness and sensitivity of the device.

1.1 Traditional Biophotonics Techniques

Light is very often used in biosensing to provide data concerning the location of target molecules or to display a visual response from a chemical reaction. Two primary detection methods are absorbance change and luminescence intensity. Luminescence has many different forms but the two most commonly used in biosensors are either fluorescence or bioluminescence depending on whether an excitation light is required or not for the luminescence event to take place.

1.1.1 Fluorescence

Fluorescence involves the absorption of a photon at one wavelength which in turn causes emission of another photon at a higher wavelength as shown in figure 1.1. The difference in the wavelength between the excitation and emitted light is known as the Stokes Shift. A higher Stokes shift is desirable as it makes the excitation light much easier to filter out from the total collected light. The time it takes for an electron that has been excited to a higher state to relax back to its ground state is on the order of 100 nanoseconds or shorter which separates fluorescence from phosphorescence in which the electrons relax over a longer period of time thus emitting light for up to an hour in some cases after being excited [1]. Fluorescence is used extensively in biosensors since excitation light can easily “flood” an entire area and the fluorescence resulting from either tagged molecules or genetically altered proteins can be measured or used as a tool for relaying the position of the biomolecules. This

procedure is performed by a specially designed fluorescent microscope which will illuminate the stage at one wavelength, but collect light at a different wavelength through filtering. This is a highly practiced technique for biological analysis [2, 3].

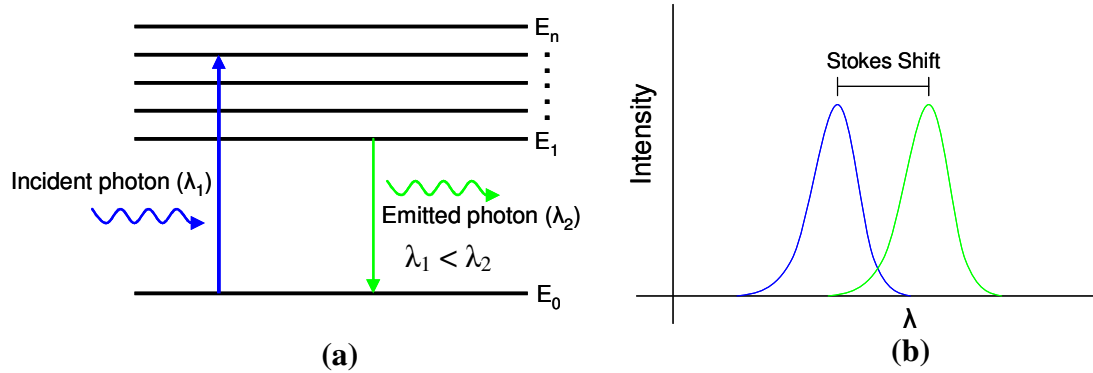


Figure 1.1: (a) Fluorescence through promotion of an electron to a higher energy state. (b) Demonstration of the Stokes Shift between absorbed and emitted light

Biomolecules can be tagged with a variety of different fluorophores such as the Alexa Fluor series from Molecular Probes or the DyLight Fluors from Thermo Fisher Scientific [4]. These fluorophores have been manufactured to span the range of the visible light spectrum (400 – 700 nm). The fluorophores are conjugated to either the primary amino groups ($-\text{NH}_2$) or thiol groups ($-\text{SH}$) of proteins, DNA and amino acids for sequencing and detection applications [5, 6].

1.1.2 Bioluminescence

Bioluminescence is not used as commonly as fluorescence in biosensing. This derives from the fact that only a few biological species exhibit bioluminescence and only do so under specific chemical reactions. Nonetheless, the use of some of these organisms for detecting the presence of the reagents that cause the bioluminescence has been performed. Bioluminescence holds one distinct advantage over fluorescence based detection in that no excitation light is required to achieve luminescence.

However, it still suffers from being more of a qualitative measurement of a reaction taking place.

The bioluminescence of many bacterial species has been shown to degrade in intensity when in the presence of phenols or other toxic media such as heavy metals [7]. This response to dangerous compounds has led to the investigation of using bioluminescent bacteria in sensors. Other sensor ideas have been proposed to test for the presence of the chemicals which trigger the luminescence. For instance, the luciferase from the common firefly is created from the combination of luciferin and ATP, the levels of which can control the intensity of the luminescence [8]. *Vibrio Harveyi*, a species of bioluminescent marine bacteria, display luminescence in the near-UV range in the presence of the autoinducer AI-2 [9]. The AI-2 is of particular interest to the medical community as it is used by bacterial cells to ultimately form a pathogenic bio-film, a dense matrix of bacteria and polysaccharides [10]. By using the *Vibrio Harveyi* cells to monitor the levels of AI-2 production, drugs can be screened for inhibiting the formation of the disease-causing bio-films.

1.1.3 Absorbance

Absorbance is another commonly used optical detection technique both for laboratory analysis and on-chip studies. Absorbance through a medium can be directly related to the concentration of the absorbing species present as related by the Beer-Lambert law shown in equation 1.1 [11].

$$\begin{aligned} A &= \epsilon l c \\ A &= \log\left(\frac{I_0}{I}\right) \end{aligned} \tag{1.1}$$

Where ϵ is the molar absorptivity, l is the optical path length through the absorbing medium, c is the concentration of the absorbing species and I_0 is the intensity of the input light (baseline). By measuring the change in light intensity before and after the introduction of absorbing species, the concentration can be accurately calculated due to the linear relationship between absorbance and concentration. The molar absorptivity can be calculated empirically by measuring the absorbance of known concentrations.

Absorbance can be measured across a broad range of wavelengths quickly by using a tool known as a spectrophotometer. Fluid cuvette spectrophotometry is a well established method for determining not only concentration of a particular species, but also the chemical composition of certain organic molecules based on the detected absorbance bands. The cuvette is a small, transparent square container which holds the solution for analysis and is placed into individual cells of the spectrophotometer to analyze the absorbance spectrum through the liquid. This procedure has been conducted for the analysis of various biomolecules [12-14].

The device described in this thesis uses absorbance measurements to detect different concentrations of the phenol catechol. Thus, absorbance as it pertains to the device's particular dimensions and application will be discussed further later.

1.2 Catechol Detection

Different methods have been devised for detecting the concentration levels of catechol and other similar phenols. The task is difficult because of the existence of numerous different phenols, not all of which are harmful. Providing adequate

selectivity for detecting one phenol over another is a challenge for any proposed sensor.

1.2.1 Phenols

Phenols are a class of organic compounds which contain a hydrocarbon (benzene) ring with one or more hydroxyl (-OH) groups. Phenol is also the name of the simplest type of phenol with a chemical formula $C_6H_5(OH)$. Phenols with two hydroxyl groups, such as catechol, are called Benzenediols. Catechol has a chemical formula of $C_6H_4(OH)_2$ and its structure is shown along with some other common phenols in figure 1.2.

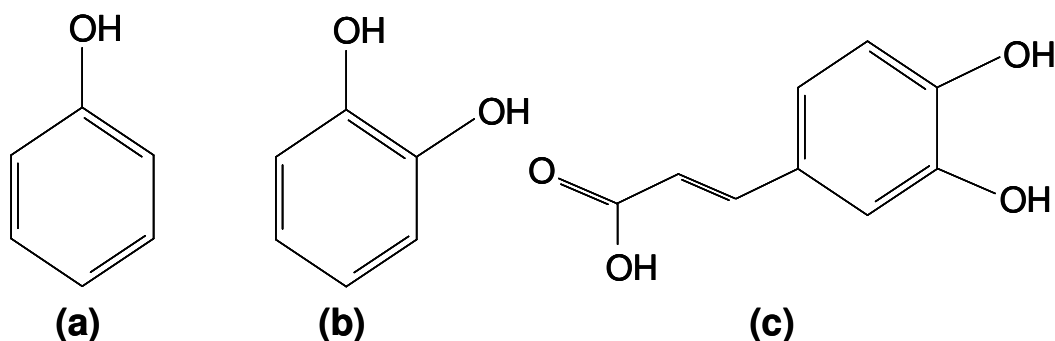


Figure 1.2: The molecular structure of (a) phenol, (b) catechol and (c) caffeic acid which is found in many fruits and vegetables.

There are hundreds of different types of phenols found to occur naturally in fruits, nuts and grains [15-18]. Phenols are antioxidants meaning they will oxidize very readily and thus slow or prevent oxidation reactions occurring to other compounds. For many phenols, this is a very beneficial process as it helps to reduce free radicals in the cells which can cause damage. A lack of sufficient antioxidants in the cells can lead to a condition known as oxidative stress as the free radicals damage vital cell structures.

Simple phenol structures like catechol react differently when in the cell. Catechol is a relatively non-polar molecule which allows it to be easily taken up by the cells but not easily expelled. The unbalanced accumulation of any foreign species in the cells can lead to the destruction of the cell. Furthermore, upon oxidation, catechol acts very similar to the aforementioned free radicals and will bind to critical cell components such as lipids, proteins and DNA [19]. The binding destroys the functionality of the component in the cell. Catechol was deemed a federal hazardous pollutant in 1993 and studies have shown that it may even have carcinogenic effects on cells [20-22].

Upon oxidation, the hydrogen atoms are pulled off the catechol and it becomes an orthobenzoquinone or *o*-quinone for short. The *o*-quinone acts as an oxidizing agent and will revert back to the original catechol structure after being reduced. The oxidation or reduction process can be either chemically or electrochemically stimulated. This process is shown in figure 1.3. The *o*-quinone is highly unstable and will readily bond to any nucleophilic surface. The toxicity to cells results from these *o*-quinones binding to vital cell structures, but this readily binding nature can be taken advantage of to detect the concentration of the *o*-quinones as they bind to a particular surface. This detection methodology will be discussed in more detail later as it pertains to the device described in the thesis.

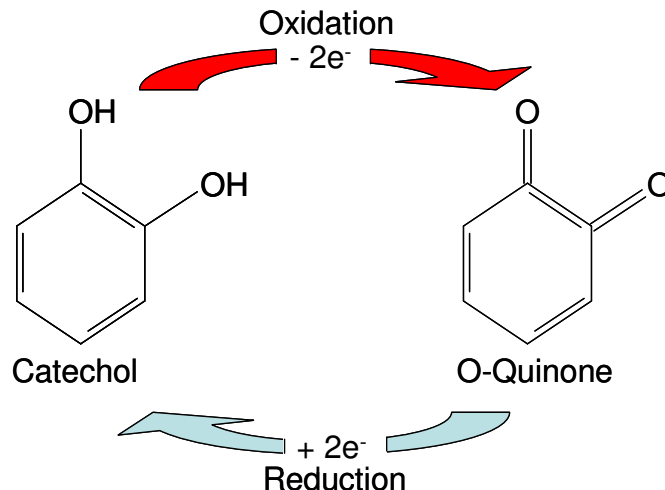


Figure 1.3: Catechol becomes an o-quinone following oxidation and is reverted back to its original form following reduction.

1.2.2 Electrochemical Detection

The oxidation of phenols like catechol or of many other types of organic molecules can be electrically stimulated at the anode surface during an electrochemical reaction. This controlled reaction can be measured as a current change which results from the oxidation of the target molecules. The amplitude of the measured current is directly proportional to the concentration of the oxidized analytes in the solution. In order to achieve the most stable measurements, three electrodes are typically employed for measuring the extent of the oxidation reaction taking place. The three electrodes are referred to as the working electrode, reference electrode and auxiliary or counter electrode. The reaction in question takes place at the surface of the working electrode due to current that is passed between the working and counter electrodes. The reference electrode is comprised of a material with a very stable and well known electric potential. The most commonly used reference electrode material is silver/silver chloride (Ag/AgCl) due to its stability and low cost. The potential difference between the reference and working electrodes is kept constant via a device

called a potentiostat. The change in resistance due to the exchange of electrons between the working electrode and the oxidizing analyte will manifest itself as a current reading since the potential is kept constant. Three-electrode electrochemical sensing has become one of the dominant methods for accurately detecting concentrations of numerous chemicals [23, 24].

Many groups have employed the described electrochemical scheme strictly for catechol detection. In an effort to amplify the resulting signal and achieve selectivity, an oxidizing enzyme such as polyphenol oxidase (PPO) or laccase is used to chemically oxidize the catechol in the vicinity of the working electrode. The enzymes are immobilized within a polymer matrix that is deposited over the surface of the electrode. When using the enzyme for the oxidation, the working electrode is biased at a negative potential and thus acts as the cathode while the counter electrode is the anode. The catechol is chemically oxidized by the enzyme, then is reduced at the electrode surface, after which the recovered catechol molecule can be oxidized again by the enzyme and the process repeats. This cyclical reaction allows for the detection of very low concentrations. The process is described graphically in figure 1.4.

Very low concentrations of catechol in the nano-molar range have been detected while using PPO enzyme immobilized in polymer matrices such as calcium carbonate [25], polypyrrole [26] or organoclay [27]. Other electrical sensing techniques have used electrophoresis in an attempt to separate the catechol from any other compounds present before performing the electrochemical oxidation [28]. Layer by layer (LbL) deposited films have also been demonstrated that sandwich the enzymes between layers of trapped catechol for detection [29].

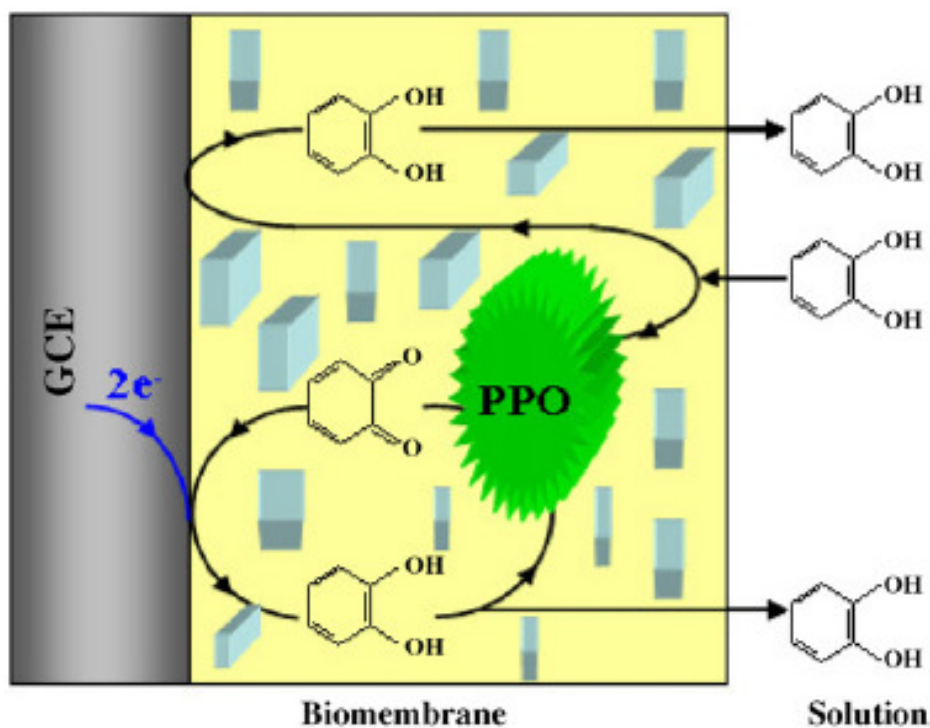


Figure 1.4: Catechol from solution diffuses through the polymer matrix and is oxidized by the PPO enzyme then reduced at the electrode surface [25].

1.2.3 Optical Detection

Another approach to detect the presence of catechol is to use optical absorbance measurements. The *o*-quinones generated upon catechol oxidation display a characteristically high absorbance in the UV and near UV range of the electromagnetic spectrum. These *o*-quinones can be covalently bonded to amine groups found on a polysaccharide film of chitosan to confer this absorbance property to the film. Chitosan as it relates to being a biological functionalization layer in sensors will be discussed in more detail in section 1.4.

Prior research performed at the University of Maryland has quantified the effects that the oxidation of catechol and other phenol types have on these chitosan films. Dr. Gregory Payne pioneered this discovery in 1995 with research involving

absorbance changes in chitosan films laced with the enzyme tyrosinase and in the presence of varying concentrations of catechol and phenol [30]. It was later discovered that the generated *o*-quinones not only altered the absorbance properties of the film, but mechanical and conductivity properties as well [31]. Further FTIR analysis confirmed that the *o*-quinones were in fact bonding to the exposed amine groups found on chitosan's polymer chains [32]. Figure 1.5 demonstrates some of the patterned chitosan films.

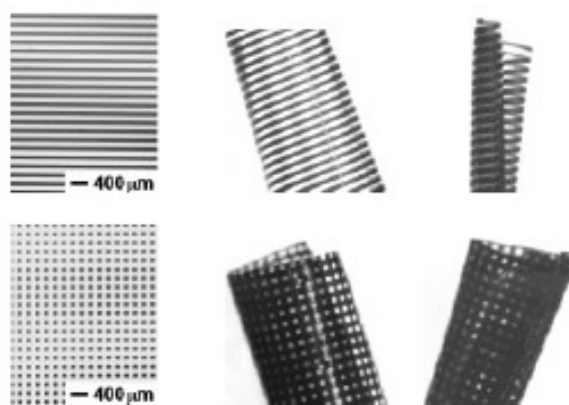


Figure 1.5: Chitosan films patterned through catechol oxidation. The dark areas are due to the absorbing O-quinones present [31].

Other groups have also used the absorbance property of the O-quinones for catechol detection. Chitosan with laccase enzyme have been cast onto slides and used to measure the absorbance changes when subjected to varying concentrations of catechol. In an attempt to amplify the absorbance effect for small concentrations, MBTH (3-methyl-2-benzothiazolinone hydrazone) is added as well. The MBTH couples with the O-quinones to generate an azo-dye product which results in a strong absorbance around 500 nm [33, 34]. Other unique methods of optical

detection have been utilized by measuring the fluorescence detected due to a change in dissolved oxygen content as the phenol oxidizes in a controlled chamber [35].

1.3 Lab-on-a-Chip Devices

The ability to perform typical laboratory testing procedures all on a single chip has many advantages. Lab-on-a-chip devices deliver low cost, high throughput sensors that can be even more sensitive than their macro-scale counterparts. They allow even untrained users to gather data and to take the sensing capabilities out into the field. Described further in this section is a more in depth look into the components of many typical lab-on-a-chip sensors.

1.3.1 MEMS Technology

At the forefront of sensor technology are devices fabricated using standard MEMS techniques. Micro-electromechanical Systems (MEMS) use wafer level technology that has already been standardized by the IC industry. This means that MEMS are typically cost-effective and can be monolithically integrated with MOSFET technology to complete a total analysis system. Numerous devices can be fabricated on a single 4 or 6 inch wafer utilizing common techniques such as surface or bulk micromachining to create mechanical structures [36]. The bulk wafer material ranges from the standard silicon, to III-V compounds like indium phosphide for photonics applications, to Pyrex glass used commonly as a substrate for microfluidic devices.

1.3.2 Optical Integration in MEMS

Optical measurements are used extensively on the micro scale for a variety of applications. The integration of light with devices of such a small size can lead to problems including adequate filtering of unwanted optical sources, and focusing the light onto such small dimensions [37, 38]. Laser diodes and LEDs spanning the spectrum from the UV to IR range typically provide the optical sources either integrated onto the chip itself or focused into optical fibers which then carry the light to the device. The light is usually confined within patterned waveguides which guide the light to the active area of the chip for sensing.

On-chip lasers are typically expensive and difficult to fabricate, requiring layers of doped III-V materials. It is also difficult to monolithically include waveguides on chip which line up with the collimated light output of the laser. A possible solution is to use polymer or fluid dye lasers doped with fluorescent materials such as Rhodamine 6G [39, 40]. Figure 1.6 demonstrates how a fluid dye laser made from SU-8 can be easily integrated with patterned waveguides to create numerous optical sensing sites in a microfluidic channel. The dye in the channel is pumped using a Nd:YAG laser while a bragg grating defined in SU-8 selects a single wavelength to be coupled into the bus waveguide. Other examples of integrated dye lasers have also demonstrated tuning of the wavelength by either mechanically altering the distance between the bragg gratings or changing the refractive index of the solvent solution containing the dye molecules [41].

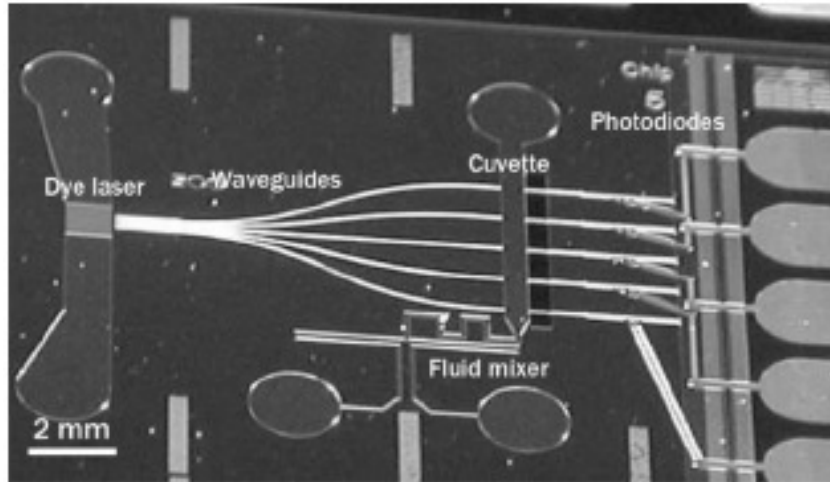


Figure 1.6: Photo of device displaying on-chip integration of a dye laser, SU-8 waveguides, fluid channel and photodiodes for light intensity detection [39].

Single and multimode optical fibers are also commonly used to introduce and collect light to and from a micro scale device. Tapered fibers allow for better coupling efficiency into smaller waveguide core diameters as shown in [42, 43]. Fibers can also be attached to the chip itself and butt-coupled to the polymer waveguide core for efficient light transmission [44, 45]. The careful alignment of the fibers to the waveguide core can be challenging.

Polymer waveguides are used extensively for guiding the light on chip due to their ease of fabrication and relatively low cost [46]. The most used polymer material for optical waveguides is SU-8 due to the many thicknesses it can be spun at and for its high refractive index making it a good candidate for optical transmission. SU-8 has been used not only for the fabrication of single and multimodal waveguides, but also for lenses with high numerical apertures and very short focal lengths [47-49].

Other unique methods for optical integration include using erbium-doped silicon or quantum dots. Erbium trivalent ions emit photons at a wavelength of 1550 nm when excited at higher energies which is a very useful wavelength for

telecommunications as it is the wavelength in which silica fibers experience the lowest material absorption [50]. Using silicon in photonics has many useful advantages including the ease of its integration with standard MOS technology [51, 52]. Quantum dots are III-V or II-VI materials grown so that all three dimensions are no larger than about 10 nm. The quantum confinement of the density of states in three dimensions causes quantum dots to emit light directly based on their size which is utilized for numerous biological applications [53, 54].

1.3.3 Microfluidics

Lab-on-a-chip devices employ fluidic channels typically on the micron or even nano scale for the efficient delivery of very small sample volumes to the sensing area. Fluids confined to such small dimensions flow in uniform layers with no disruption between layers. This phenomenon is known as laminar flow and is highly desired in many sensing applications as fluid turbulence can disrupt the biological activity being studied and cause unwanted noise to the collected signal.

Microfluidic channels are typically patterned using a photosensitive polymer such as SU-8 for tall channels or simple photoresists on the order of a few microns in thickness [55, 56]. Other methods include dry etching channels in the glass substrate itself [57, 58] or using a molding process to pattern channels in an elastic polymer, PDMS (Polydimethylsiloxane). This mold process for microfluidic devices was pioneered by George Whitesides' group and the procedure is shown in figure 1.7. The first step involves patterning a mold of the desired channels on a wafer, then curing the PDMS over the mold [59, 60]. Afterwards the PDMS film is peeled off and maintains the pattern from the mold. The PDMS layer with patterned channels can be

bonded with high strength using oxygen plasma to any glass substrate while the mold can be reused again and again for further patterning.

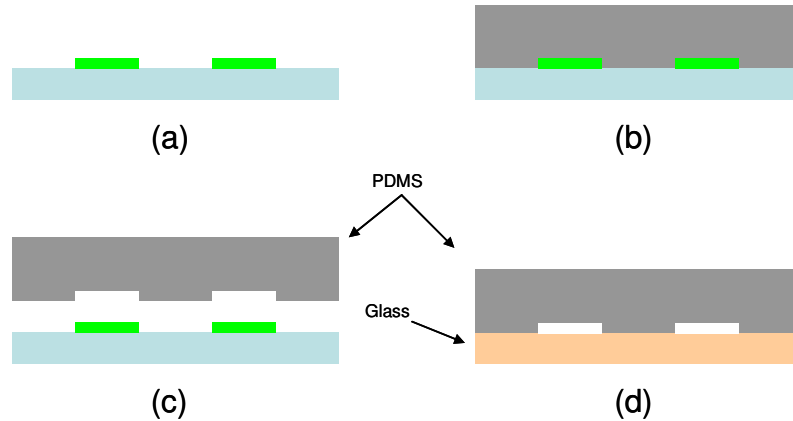


Figure 1.7: (a) Photoresist is patterned onto a blank wafer to create the mold. (b) PDMS is cured over the mold and lifted off (c). The PDMS is plasma bonded to a glass substrate (d).

Carefully controlling the liquids on chip using fabricated pumps and valves can promote these devices to being fully functional systems. Mechanical valves have been demonstrated, but the fabrication is complex and their reliability over time is questionable. The previously mentioned molding technique with PDMS has also been employed for the creation of valves using pressure channels patterned in a second layer of PDMS. The pressure channels lie orthogonal to the fluidic channel below and can seal the fluidic channel when pressurized gas is applied through them [61]. Pumps are inherently more complicated to implement than valves, especially on the micro scale. Micropumps are typically electrostatic, piezoelectric or pneumatic [62-64]. However, due to the fabrication difficulties and low achievable pumping pressures, an external syringe pump is still widely employed for many microfluidic devices.

1.4 Biofunctionalization

Biosensors must utilize creative methods in order to spatially and temporally control the reactions that are of interest in the MEMS device. Specialized interfaces in specific areas of the device work as a linking mechanism between the materials of the device and the biological agents being studied. These interfaces can allow for the specific binding of a particular molecule, or provide numerous active sites for the binding of complementary molecular structures.

1.4.1 Traditional Techniques

One of the more common practices for the immobilization of biological reagents in a microfluidic device is to use immunoassays. An immunoassay is a test which can measure the concentration of a biological substance based on its binding interaction with a complementary antibody. Antibodies bind selectively to their particular antigen very similar to a lock and key. Figure 1.8 shows a visualization of an antibody which includes an Fc region which can be bound to certain receptors and proteins and an Fab region which binds to the complementary antigens [65]. Antibodies can be used in lab-on-a-chip devices to screen for the presence of particular antigens which are usually tagged using fluorophores for detection. Likewise, the antibodies themselves can be tagged and the quenching of the fluorescent signal upon binding can be detected [66]. It is also fairly common practice to coat carboxyl functionalized microbeads of polystyrene (~75 microns diameter) with antibodies to increase the effective surface area dramatically [54, 67]. Other methods include detecting phase shifts resulting from the antibody-antigen binding reaction using surface plasmon resonance imaging [68].

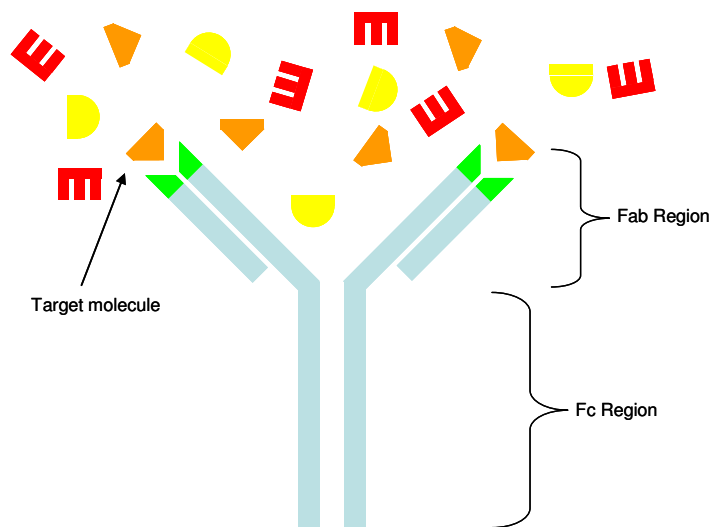


Figure 1.8: Antibody with labeled Fc and Fab regions. Only the molecules specifically coded for the particular antibody will bind as shown in the figure.

Thin films of various materials can also act as binding sites for different types of biological molecules. For instance, molecules with thiol (-SH) groups like those found on cysteine amino acids have been shown to bind to gold patterned surfaces creating what is known as a self assembled monolayer (SAM) [69]. Other films include deposited polysaccharides which can contain numerous active binding sites for biomolecules along the lengths of the polymer chains. Chitosan is a polysaccharide worthy of particular note and is very well suited for fabrication in micro devices.

Chitosan is an aminopolysaccharide due to the presence of amine groups (-NH₂) on every repeating sugar residue of its structure. The high amine group density makes chitosan very attractive as a functionalization layer. Chitosan has been well characterized in literature for a variety of botanical and medical applications due to its swelling capabilities and biocompatibility [70, 71]. Chitosan is derived from the partial deacetylation of chitin, an abundant material found in the shells of numerous

species of marine life and insects. Chitosan is cationic while dissolved in solution, but will become deprotonated and no longer water soluble as the pH rises above a pKa of about 6.5 [72]. Figure 1.9 gives the general structure of soluble vs insoluble chitosan. The proceeding sections will detail more about the chitosan patterning and amine conjugation techniques.

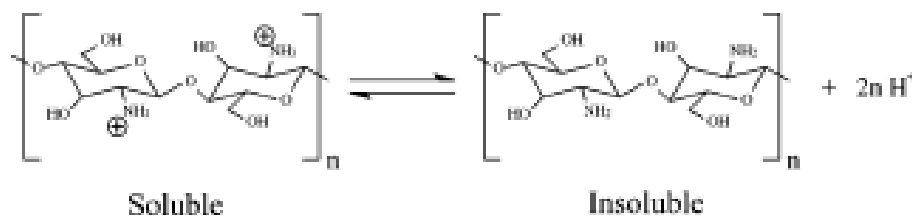


Figure 1.9: Chitosan structure in both its soluble and insoluble forms [71].

1.4.2 Chitosan Patterning Techniques

Many methods have been developed for patterning chitosan films and gels (thick films) for use in lab-on-a-chip devices. Chitosan films can be cast onto devices by simply allowing droplets of the solution to dry. This solution casting method results in fairly uniform films with thickness proportional to the % W/V of the chitosan solution used. This technique is typically used for performing experiments on glass slides and is rarely seen for micro devices due to the lack of spatially selective deposition. Patterning of chitosan films through the use of a photoresist mask and reactive ion etching has also been reported [73]. This etching process allows for the fabrication of structures composed entirely of chitosan, but the potential surface damage to the amine groups due to the processing is a concern. Nanoimprinting of chitosan has been demonstrated to create highly localized areas of chitosan with dimensions as low as 150 nm [74]. A mold made from PDMS is placed

over a droplet of chitosan with heat and pressure applied to create patterned areas of chitosan after the mold is removed. Disadvantages of this technique include the necessity for a planar surface to begin with and the application of heat and pressure which could also damage the surface morphology of the chitosan.

A promising patterning technique utilizes chitosan's unique ability of becoming insoluble at pH higher than 6.5. Electrodeposition of chitosan deposits a thin film on a negatively biased electrode [75, 76]. This deposition occurs due to the highly localized rise in pH at the surface of the cathode due to the reduction of the hydrogen ions as shown in figure 1.10. The deposition rate is based on a variety of conditions including the amplitude of the applied current density, the geometry of the electrodes used, the starting pH of the chitosan solution and the molecular weight of the chitosan. Electrodeposition has been employed in the fabrication of sensors fabricated at the University of Maryland over the past few of years [77-79].

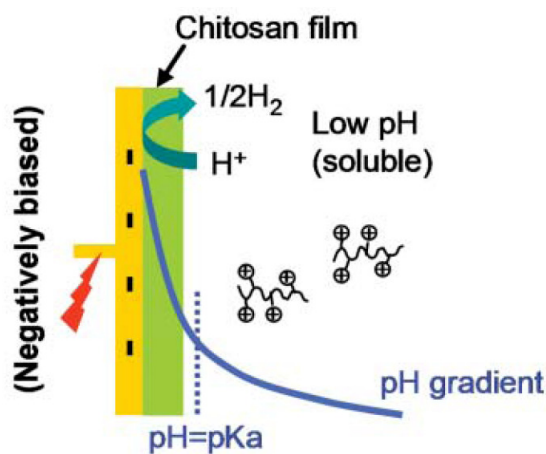


Figure 1.10: Electrodeposition of chitosan occurs at the surface of a negatively biased cathode due to the increase of the pH above the pKa value [78].

1.4.3 Amine conjugation

There are different methods utilized for the conjugation of biomolecules to the chitosan amine groups. Most molecules themselves may not actively bind to the amine group, and so they can be “tagged” using tyrosine. When subjected to tyrosinase, the tyrosine tag becomes activated and will readily bind to the chitosan amines much in the same way as the previously mentioned *o*-quinones generated from catechol oxidation [80].

DNA can be selectively bound to amine terminated probe DNA strands for hybridization experiments. However, an amine group will not bond to another amine group without some sort of linking molecule between the two of them much like puzzle pieces fitting together. Glutaraldehyde is used to form covalent bonds between the amine groups of the chitosan and those of the probe DNA [75]. In this way, any similar molecules with amine-terminated ends can bind to the glutaraldehyde at the chitosan surface.

2 Device Design

This chapter will cover not only the previous iterations of the current biophotonics platform, but also the theory associated with its design. A few of the aspects of the current device including the sidewall patterning procedure of the indium tin oxide and the dimensions of the waveguides and fiber clamps were devised previously in a device which detected fluorescently labeled species attached to a sidewall patterned film of chitosan [81]. The work was continued through a demonstration of DNA hybridization using the previously designed devices [82]. These previously established methods were modified for the current design and new procedures were established in order to encapsulate the microfluidic channel and use the waveguides for absorbance measurements. The theory behind light propagation and sources of attenuation through the device will also be carefully examined in this chapter. The choice of materials and dimensions used for each component of the device will be discussed as well.

2.1 Design Iterations

The biophotonics platform underwent three distinct iterations to reach the final design. The first stage involved the preliminary research conducted before work on the current catechol sensor began. The second involved test chips that were designed to better understand the nature of the absorbance experiments. The final stage combined the catechol detection with some established elements from previous research to create the final device.

2.1.1 Previous Research

The idea of using chitosan patterned on the side of a waveguide facet for optical interrogation purposes has been previously demonstrated and can be found in [81, 83]. The device utilized a single patterned SU-8 waveguide with one end coupled to an optical fiber and the other end covered with a thin chitosan film. Excitation light was applied from the top onto the active area and the fluorescence was captured in the waveguide as seen in figure 2.1.

Utilizing in-plane excitation was abandoned since the collected light saturated the detector and made it difficult to measure the fluorescence intensity. This device was used to demonstrate not only detection of amine conjugated fluorophores, but later fluorescently tagged DNA which were attached to covalently bound probe DNA at the chitosan surface [82].

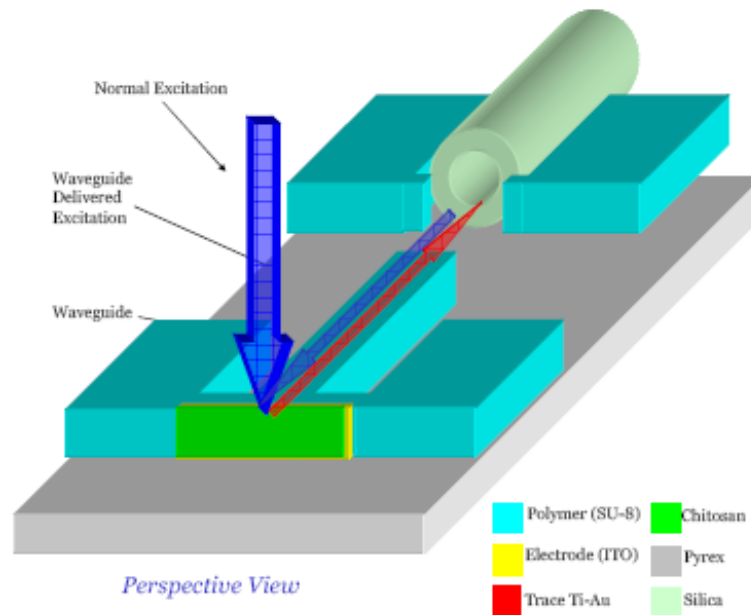


Figure 2.1: 3-D schematic of early biophotonics device [80]. Excitation light is delivered top-down while the waveguide collects the resulting fluorescence and scattered excitation.

The biophotonics device developed for this thesis shares some similarities to this first generation platform. The same materials are used on the waveguide facet to facilitate the chitosan deposition and the dimensions of the waveguides have been kept the same in order to easily couple to 62.5 μm core multimode optical fibers. However, the fabrication parameters were changed to reduce film stress of the SU-8 and is described in more detail in section 3.3. The exact dimensions of the waveguide are not critical so long as they are much larger than the wavelength of light that is propagating as will be discussed in more detail in section 2.2.2.

2.1.2 Absorbance Test Chip Design

The first chips that were designed for absorbance measurements are similar to previous iterations, except that polymer waveguides have been patterned on either side of the channel in order to couple light in-plane through the device. This design did not have enclosed channels to simplify testing procedures.

Figure 2.2 displays the L-edit mask design for the test chips. Notice that the design employs two different configurations for the electrode at the waveguide facets. One design uses only one sidewall while the other design allows for both sidewalls to be covered with the ITO. This was done to determine if having chitosan on both waveguide facets contributed to a higher absorbance signal following catechol oxidation compared to only having a single chitosan sidewall. The working electrodes were linked together to allow for a single chitosan deposition step to deposit a film in both locations. For clarity, the electrodes with the ITO are called working electrodes while the other larger electrode is the counter electrode.

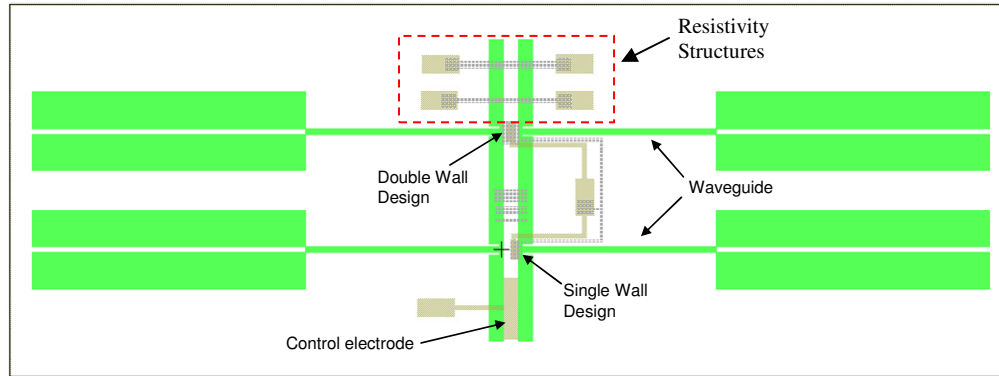


Figure 2.2: Mask design for test chips using L-Edit software. Green: SU-8, Brown: Gold, Grey: ITO

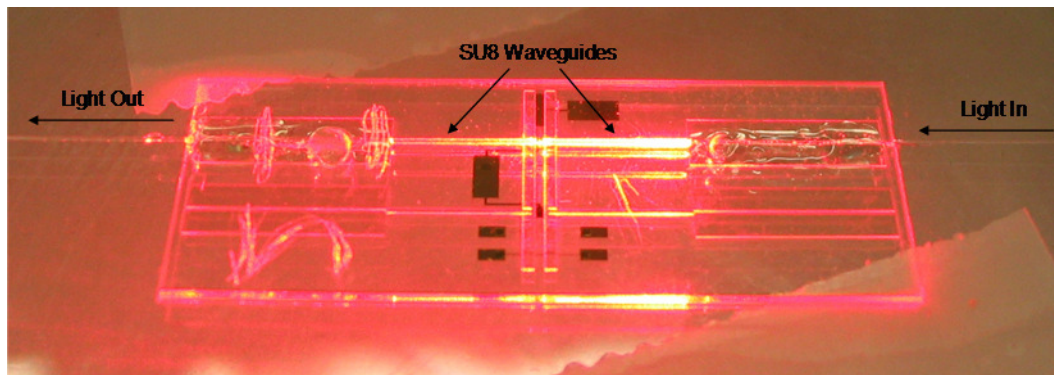


Figure 2.3: Picture of test chip demonstrating the in-plane coupling of red light at 633 nm.

The design also includes test structures at the top meant to measure the resistivity of the ITO that is patterned across the SU-8 walls. These chips were fabricated on a pyrex substrate and diced for individual testing.

Preliminary coupling tests were performed using multimode optical fibers attached to both ends using UV cured epoxy and transmitting red light at 633 nm from a free-space diode laser through the device as seen in figure 2.3. By measuring the input intensity compared to the output intensity using a spectrometer (USB2000, Ocean Optics, USA) the total loss through the device including any coupling losses is

around -25 dB. This calculation is in good agreement with the transmission mode losses calculated by Powers et al. for the original device design [81].

Testing of these chips with a chitosan film deposited in the channel was carried out with the help of Vildana Hodzic at the University of Maryland. No appreciable absorbance signal could be detected from oxidizing catechol using these chips. It was discovered that this was due to the design of the working electrode. The large working electrode in the channel also allows for a chitosan film to form on the bottom of the channel. Once crosslinking of the chitosan film due to the oxidation of the catechol occurs, the film shrinks by approximately 40% to 50%. This shrinkage causes more light to propagate through the open air than before the oxidation occurred, introducing a large source of error in the absorbance measurement. To avoid this problem, the working electrode must be patterned as close to the sidewall as possible to reduce the amount of chitosan that is deposited along the bottom of the channel.

2.1.3 Final Microfluidic Design

The final device design was developed using the data obtained from the test chips. The L-edit mask file for the design is shown in figure 2.4. The major changes to the structure include patterned inlet and outlet ports for the enclosed microfluidic channel and a much larger device footprint of patterned SU-8 in order to form a planar surface for a polymer capping layer to sit. The electrode design was also redesigned to prevent the dependence of the absorbance measurement on the chitosan thickness. The working and counter electrodes were placed directly across from one another with the working electrode as close to the SU-8 wall as possible.

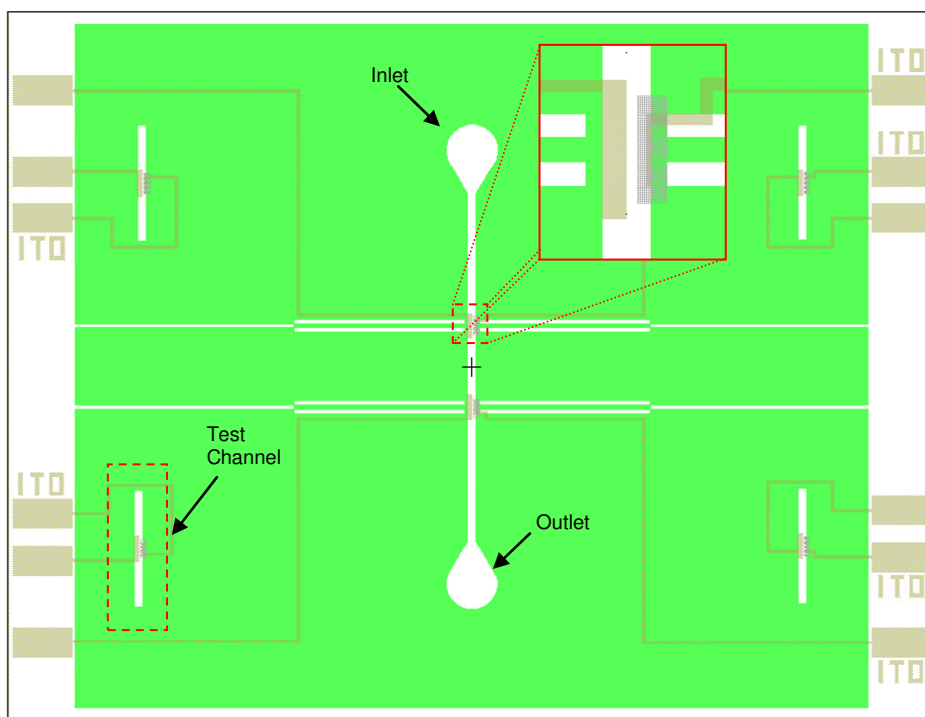


Figure 2.4: L-edit mask design of the final microfluidic device. The chip size is 32 mm x 24.4 mm. Green: SU-8, Brown: Gold, Grey: ITO

As can be seen from the blown up section of the channel electrodes in figure 2.4, the working electrode on the right still extends a short distance into the channel due to lithography constraints, but it is much less than from previous designs. At the four corners of the device are test channels which were used to characterize the chitosan deposition conditions. Two distinct sensing sites have been patterned on the same chip to demonstrate the ability to incorporate an array of sensors in a single channel. Large electrode contact pads were patterned around the perimeter of the chip to be easily accessed using probes. The critical device dimensions are given in table 2.1 and a 3-D schematic of the final device can be seen in figure 2.5. The design of each component in the final device will be presented in the proceeding sections.

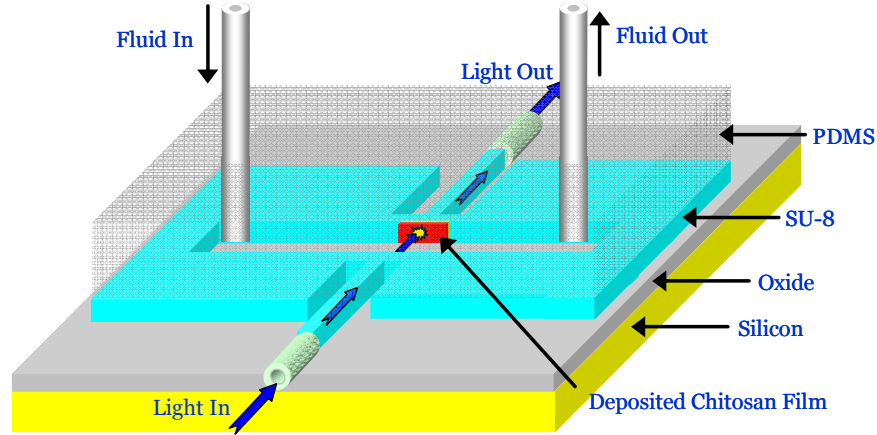


Figure 2.5: 3-d schematic of the final device used for absorbance testing through the chitosan film.

Table 2.1: Dimensions of important device structures.

Structure	Size (μm)
Waveguide	100 x 125 x 6000
Channel	300 x 100 x 15000
Counter Electrode	150 x 865
Working Electrode	30 x 450
ITO Area	182 x 670

2.2 Waveguides

Possibly the most important component of any photonics platform is the waveguide which couples the light through the device. The choice of materials, size, and surface roughness all play a large part in how the light propagates through the device. This section will also analyze other sources of optical loss including divergence as the light moves across the channel from one waveguide to the next and scattering due to roughness.

2.2.1 Materials

Choosing the right materials is important in order to minimize the optical loss. Light remains contained within a waveguide due to total internal reflection (TIR). A typical waveguide consists of a higher index core and surrounding lower index cladding to allow for total internal reflection to occur. For a strip waveguide like the ones employed here, the cladding material will vary since the waveguides will be patterned on a substrate and have a different material on top which acts as the capping layer to the microfluidic channel. Figure 2.6 displays a cross section of the waveguide showing the different cladding materials and their index of refraction.

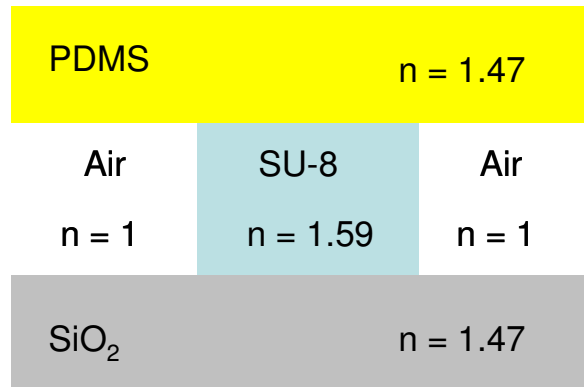


Figure 2.6: Cross section of strip SU-8 waveguide showing the different cladding materials. Note that the SU-8 index is higher than that of the cladding which allows it to act as a waveguide.

It should be noted that due to the relatively large size of the waveguides compared to the wavelength of light being used, ray optics assumptions can be used to model the light gathering ability of the waveguides. The waveguides are assumed to contain numerous possible modes and determining the energy contained in each mode is not necessary for conducting the absorbance experiments.

Total internal reflection is defined using Snell's law given in equation 2.1. The critical angle from equation 2.2 is the lowest angle that propagating rays can make to the normal of the core-cladding interface for total internal reflection to occur.

$$n_{core} \sin \theta_{core} = n_{clad} \sin \theta_{clad} \quad (2.1)$$

$$\theta_c = \arcsin\left(\frac{n_{clad}}{n_{core}}\right) \quad (2.2)$$

It is desirable to achieve as low of a critical angle as possible in order to contain light more efficiently within the waveguide. This can be achieved by carefully choosing the index of refraction of the materials. The cladding material used for the device is silicon dioxide and PDMS, both of which have an index of refraction of 1.47. The material chosen for the waveguide must then have an index that is higher than 1.47, and preferably much higher, in order to achieve a small critical angle. There are many other desired aspects of the waveguide material:

- 1) Low absorption at visible wavelengths (400 – 700 nm)
- 2) Ability to fabricate with thicknesses over 100 um. This is important in order to butt-couple the large multimode fibers to the waveguide facets.
- 3) Good sidewall profile. The roughness of the sidewalls directly leads to scattering and energy attenuation.
- 4) High refractive index as discussed previously

Polymers provide the best choice for the waveguide material due to their low absorption at visible wavelengths and ease of fabrication. Most polymers can be patterned using UV light or by using a photoresist mask and an oxygen plasma etch. The most common polymers used for waveguide cores in photonics devices are PDMS [84], PMMA [85], BCB [86] and SU-8 [87]. Of these, SU-8 has the highest

index of refraction ($n = 1.59$) at the wavelength of interest (472 nm) and it is capable of being spun at thicknesses as high as 500 μm [88]. PDMS can be made thicker but only has an index of refraction of 1.47 which would require special doping to increase. PMMA also has a relatively low index of refraction at 472 nm ($n = 1.49$) and BCB is incapable of being spun at thicknesses exceeding about 26 μm [89]. SU-8 is chemically inert to nearly all solutions which makes it ideal for patterning the microfluidic channel.

The critical angle given an SU-8 core and PDMS cladding interface is 67.6° which means that light rays which are incident to the waveguide facet at angles less than 37.3° will remain within the waveguide due to total internal reflection. These numbers were calculated using Snell's law and assuming that the index of refraction of air is exactly 1. Since the optical fibers will be butt-coupled directly up against the SU-8 waveguide facets, it can be reasonably assumed that all the light entering the waveguide from the fiber will make angles less than 37.3° to the normal of the facet without taking roughness into account.

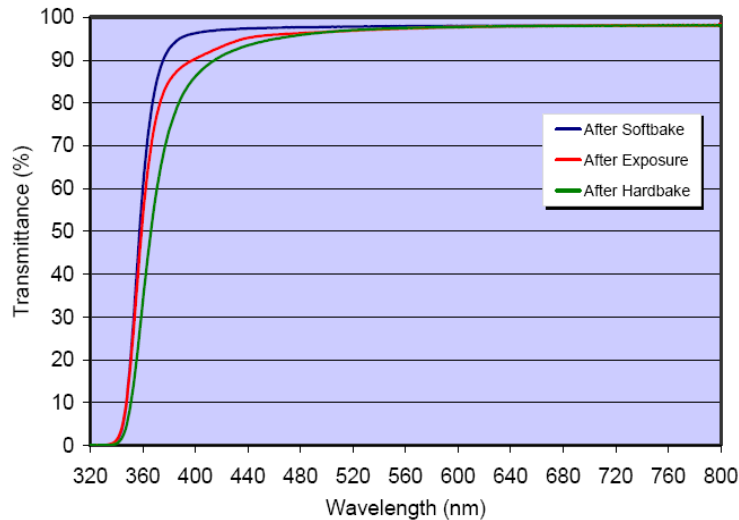


Figure 2.7: Transmittance of SU-8 films from UV to near IR [87]

The transmission through SU-8 at visible wavelengths (those between 400 and 700 nm) is very high as seen in figure 2.7. The resist only experiences high absorption in the UV range which is consistent with nearly all photosensitive polymers. The polymer waveguides can be considered very “thick” films of 1.2 cm in length, and therefore may experience a larger absorbance than thin films. This effect will be analyzed more closely in the next section.

2.2.2 Light Propagation and Loss

This section will examine in more detail the major loss mechanisms as the light is coupled through the device. Reducing the loss is important for achieving an acceptable signal to noise ratio at the output. The detector will undoubtedly have some noise associated with it due to either thermal or shot noise and the laser source can fluctuate in output power. The laser is also found to drift over time especially for the first 30 minutes after being turned on most likely due to temperature instability. The sources of loss investigated here include losses due to reflection at the different interfaces, losses due to beam divergence as the light traverses the channel from one waveguide to the next, and waveguide loss due to material absorption and scattering.

Since the light travels through materials of different refractive indices, reflection as well as refraction will occur at each interface. The Fresnel equations are used to describe the percentage of light that will be reflected away based on the index of refraction of the two materials at the interface. This reflection percentage is given in equation 2.3.

$$R = \frac{(n_1 - n_2)^2}{(n_1 + n_2)^2} \quad (2.3)$$

This equation is a simplified form of Fresnel's equation since it assumes that the rays are normally incident at the dielectric interface [50]. This assumption is valid to make for our device because the optical fibers are butt-coupled to the waveguides meaning the incident light approaches the waveguide facet at a near-zero angle. Table 2.2 shows the reflectance expected at each interface through the device from optical input to output. There are two SU-8 – Air interfaces; one for each waveguide facet coupled to the optical fibers. The other interfaces all exist in the microfluidic channel.

Table 2.2: Reflection at interfaces

Interface	Reflection
Air - SU-8	6.2%
SU-8 - Water	0.8%
Water - Chitosan	0.4%
Chitosan - ITO	2.0%
ITO - SU-8	0.8%
SU-8 - Air	6.2%
TOTAL	15.49%

Note that the total percentage of light lost is NOT the addition of the loss from each of the reflections. Rather, it is calculated from the sequential loss at each interface for a given input optical power. Reflectance overall is kept low throughout the device and the loss incurred here is minimal compared to losses due to other mechanisms as will be discussed next.

A propagating wavefront like that delivered from a laser source can be approximated as a beam with a Gaussian energy profile. The waist of the Gaussian beam will expand if the light propagates unconfined through some medium. If this expansion is too large, then much of the input light could be lost as the beam

traverses the microfluidic channel of the device from one waveguide to the next. Waveguides with dimensions that far exceed that of the wavelength of captured light contain many thousands of possible modes of propagation and it would be nearly impossible to characterize exactly which modes are being expressed at any given time. In order to calculate the capturing efficiency as the beam crosses the channel, it is assumed that the light leaving the polymer waveguide is defined by the fundamental Gaussian profile.

A Gaussian beam along a single axis is defined as shown in equation 2.4.

$$E_x = E_0 * e^{\frac{-x^2}{w(z)^2}} \quad (2.4)$$

Where $w(z)$ is defined as the size of the beam waist for a given propagation distance z . The expansion of the beam waist as the wave propagates in the z direction is given by equations 2.5 and 2.6.

$$w(z) = w_o \sqrt{1 + \left(\frac{z}{z_o}\right)^2} \quad (2.5)$$

With

$$z_o = \frac{\pi w_o^2}{\lambda} \quad (2.6)$$

Where w_o is the initial beam waist before propagating a distance of z . With these equations, we can calculate how much the propagating beams will expand as they cross the channel. In order to determine the power coupling efficiency, an overlap integral of the energy before and after traversing the channel is taken as shown in equation 2.7.

$$\eta = \frac{\left| \int_{-\infty}^{\infty} E_1(x, y) * E_2^*(x, y) dx dy \right|^2}{\int_{-\infty}^{\infty} E_1(x, y) * E_1^*(x, y) dx dy \int_{-\infty}^{\infty} E_2(x, y) * E_2^*(x, y) dx dy} \quad (2.7)$$

Where $E(x, y)$ is the electromagnetic field strength in the x and y directions as the beam propagates in the z direction. By using the Gaussian beam formula for $E(x, y)$, the efficiency is found to be related to the beam waist before and after traversing the channel as demonstrated in equation 2.8.

$$\eta = \frac{2w(z) * w_0}{w(z)^2 + w_0^2} \quad (2.8)$$

Where $w(z)$ and w_0 are defined the same as above. The initial waist of the beam is approximated to be half the width of the polymer waveguide which the light exits from. This is a valid approximation to make for dielectric strip waveguides as shown in [90]. In the situation of these devices, w_0 is $62.5 \mu\text{m}$ in the x -direction while it is $50 \mu\text{m}$ in the y -direction. The efficiency is calculated to be near unity (0.99) for waveguides of our dimensions and a channel length of $300 \mu\text{m}$. The high coupling efficiency is a direct result of using such large core waveguides. The efficiency reduces dramatically as the waveguide width becomes smaller than about $10 \mu\text{m}$ for a propagating wavelength of 472 nm as shown in figure 2.8.

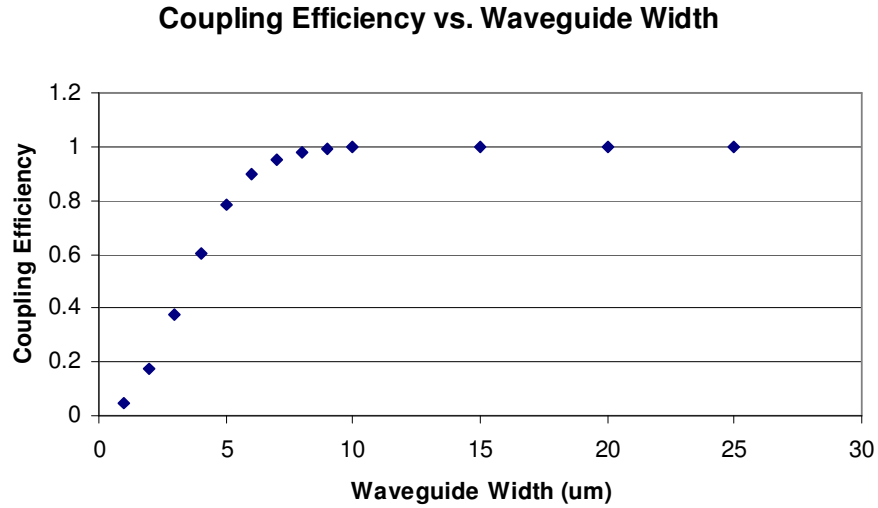


Figure 2.8: Coupling efficiency vs waveguide width assuming a channel length of 300 μm and a propagating wavelength of 472 nm.

While divergence has been shown to have little effect on the loss through the device, waveguide losses due to absorption and scattering are certain to be much higher. Material absorption occurs as the beam propagates through the SU-8 waveguide. The roughness of the waveguide surfaces will cause scattering. Absorption occurs as light travels through any dielectric medium and is due to energy being absorbed in order to excite an electron to the next available energy state. For materials with small or negligible bandgaps such as metals and silicon, the energy required to promote an electron into the conduction band is low and thus absorption is very high for light energies in the visible spectrum. This explains why many insulators like glass and most polymers with their large bandgaps appear transparent to visible light, though these materials will absorb higher IR wavelengths due to molecular vibrations. SU-8 exhibits high absorption in the UV range where the energy releases a catalytic acid that is used to crosslink the polymer chains. However, even visible wavelengths still exhibit some absorption and especially those closer to the UV range such as the one used here (472 nm) cannot be neglected.

Waveguide loss also occurs due to the roughness on the sides of the waveguide. The top and bottom of the SU-8 are fairly smooth, but due to the lithography, the sides contain many small jagged edges at the micron scale. These angular irregularities can cause incident angles of the propagating light to be smaller than the critical angle thus causing light leakage from the waveguide.

In order to calculate the total waveguide loss, a common technique is to use the cutback method in which the light transmittance is calculated for waveguides of different lengths and a curve fit is made to the transmitted intensity vs. the length of the waveguide [91]. However, the data received using this method will also include any coupling losses incurred as the fibers are aligned to the waveguides and these losses may not be the same from trial to trial. For this work, a different approach is used which involves image analysis of the light being leaked around the edges of the waveguide to determine the loss through the SU-8.

Figure 2.9 demonstrates a photograph taken of a test waveguide with the blue laser source coupled to one end through an optical fiber. The blue light rapidly decreases in intensity as it travels down the waveguide due to the losses previously described. By using ImageJ, an image processing software, the relative intensity of the light through a given area can be plotted vs. the number of pixels which designate the width of the chosen area. A stray light baffle is used at the waveguide input in order to reduce the glow generated from the high input intensity. Light is also seen coupled into parallel patterned waveguides from the scattered light at the input. A microscope slide is placed in the picture as a reference size in order to convert pixels to centimeters. The graph of relative intensity vs # of pixels is shown in figure 2.10.

The exponential decay of the intensity is what is expected as described by Beer's law for light traveling through an attenuating medium as shown in equation 2.9.

$$I = I_0 * e^{-\alpha x} \quad (2.9)$$

Where α is the attenuation coefficient.

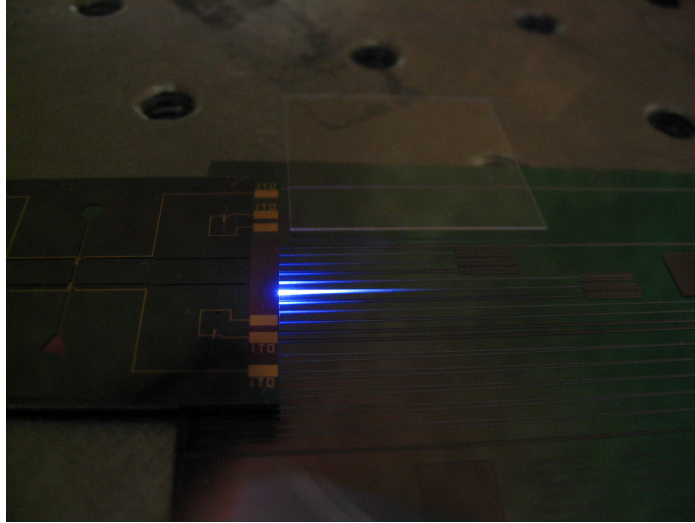


Figure 2.9: Digital photo of blue light attenuation through an SU-8 waveguide.

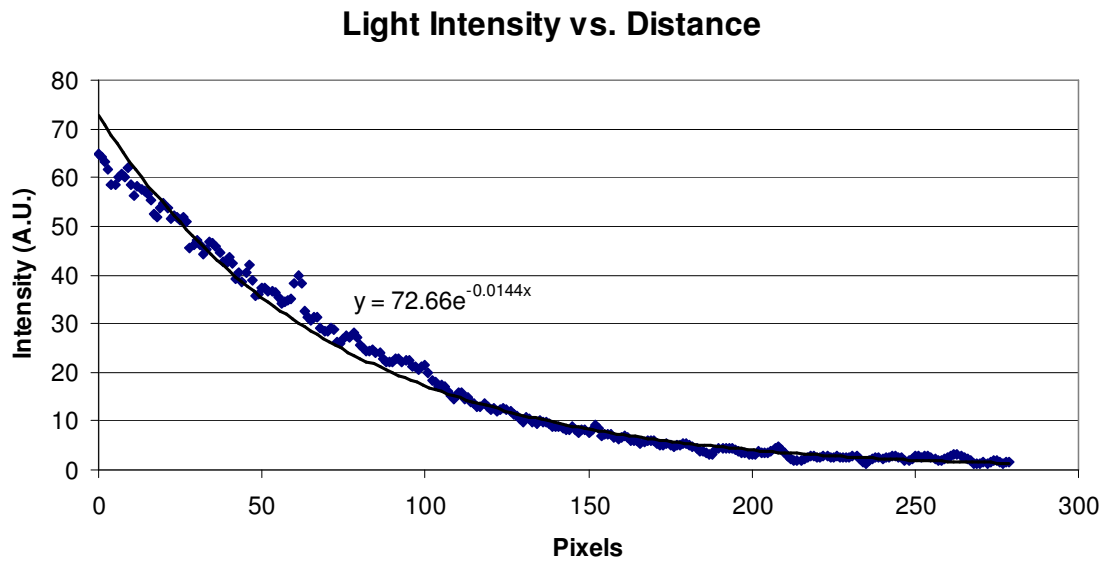


Figure 2.10: Exponential decay of light intensity as it propagates through the SU-8 waveguide.

By fitting an exponential decay function to the data, the attenuation coefficient is found to be 4.87 cm^{-1} . Expressing waveguide loss in terms of decibels per centimeter is a more common metric and an attenuation of 4.87 cm^{-1} corresponds to 21.15 dB/cm of loss. This calculated loss includes both losses due to absorption and those due to waveguide roughness. Values of literature absorption for SU-8 at a wavelength of 472 nm vary between 5-10 dB/cm [92, 93]. From these values, it is assumed that just a little more than half of the total waveguide loss is due to the roughness of the waveguide edges. This roughness can be vastly improved through the use of more advanced fabrication techniques such as proton beam [85] or E-beam lithography [94]. These methods are expensive, time consuming, and are not compatible with batch fabrication processes, which is why the best approach taken is to use chrome masks with high contrast for patterning the SU-8 resist. The improvement in sidewall smoothness achieved through the use of chrome masks over less expensive printed transparency masks has been demonstrated in more detail previously [81].

2.2.3 Facet Roughness

This roughness at the edges of the waveguides will also manifest itself at each of the waveguide facets. Facet roughness can lead to the most significant losses incurred in the whole device due to light scattering as it impinges upon the interface. Figure 2.11 displays an SEM image taken of the input waveguide facet. The dark clumps seen in the corners are photoresist residue. The striations in the polymer are clearly visible due to roughness in the mask design, even when using a chrome mask for the lithography.

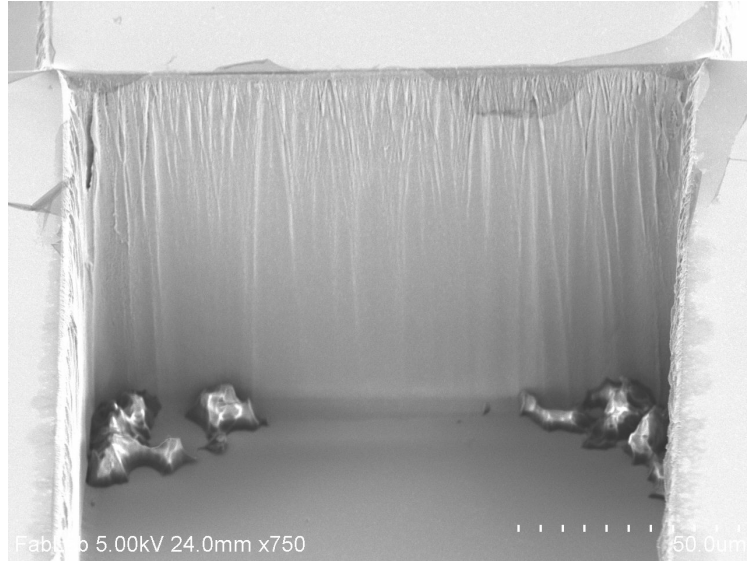


Figure 2.11: SEM image of the input waveguide facet displaying the roughness.

Scattering occurs due to the surface defects that are on the order of the size of the wavelength of light. The loss incurred due to the scattering can be related to the wavelength through Rayleigh scattering as shown in equation 2.10.

$$\alpha_R = \frac{C}{\lambda^4} \quad (2.10)$$

Where C is a constant based on the material properties. Typically, Rayleigh scattering is used to determine the attenuation over distance as light propagates through a waveguide such as an optical fiber. In our case, the scattering is occurring due to numerous local imperfections right at the facet interface. Equation 2.10 explains why much more scattering occurs for our lower wavelength of 472 nm as compared to more commonly used red light at 633 nm.

Determining the loss which occurs specifically from the facet roughness can be difficult, but can be approximated by calculating the total loss through the device.

Final loss calculations through the fabricated devices are discussed later in section 4.2.2.

2.3 Channel Design

When designing the microfluidic channel dimensions, the width is the only critical dimension. The height is set by the thickness of the polymer (100 μm) and the length does not play a significant role in the device operation.

The width is important during the patterning of the sidewall electrode. If the width is too small, the photoresist cannot adequately cover the sidewall during the patterning procedure and the fabrication will fail. The lowest allowable width was determined from previous work to be 150 μm [81]. The loss due to divergence as calculated previously is minimal and remains very low at channel widths of up to 1 mm.

In this case, the most important consideration is minimizing liquid pressure in the channel. Because the channels are capped by a layer of PDMS without any external pressure being applied, excessive liquid pressure may break the bond and cause the device to leak. The liquid pressure for a given length is defined by Poiseuille's Law and given in equation 2.11 [95].

$$\Delta P/L = \frac{128\nu Q}{\pi d^4} \quad (2.11)$$

Where ν is the fluid viscosity, Q is the volumetric flow rate and d is the diameter of the channel. For cross sectional areas that are non-circular, the hydraulic diameter can be used from equation 2.12.

$$D_h = \frac{4A}{U} \quad (2.12)$$

Where A is the cross sectional area of the channel and U is the channel perimeter. From these equations, it can be seen that smaller channel dimensions and high flow rates will increase the pressure difference. A channel size width of 300 μm was chosen to maximize the exposure of the liquid to the working electrode while minimizing the pressure. At this width, the pressure difference in the channel is calculated to be around 2 Pa/mm assuming the liquid viscosity of water and an applied flow rate of 100 $\mu\text{l/hr}$. This pressure is very low and is not enough to break the bond of the PDMS capping layer to the device.

2.4 Electrode Design

All of the patterned electrodes in the device except for the indium tin oxide, are gold due to gold's high conductivity and chemical inertness. However, gold films have poor adhesion to most substrates and so an underling layer of chrome is deposited first for adhesion. This section focuses on the design of the electrodes in the system with an emphasis on the ITO sidewall and how it is electrically connected to the rest of the system.

2.4.1 Cr/Au Electrodes

All of the large electrodes patterned at the edge of the chip are the contact electrodes. These electrodes were made large enough so as to easily place probes down on them by eye. Their dimensions are 2 mm by 1 mm.

The contact electrodes are connected to the channel electrodes via thin strips of patterned metal which run underneath the SU-8 structures. The channel electrodes consist of a large counter electrode and a smaller working electrode. The counter electrode is used to act as either the anode during the deposition of the chitosan or as the cathode during the electrochemical oxidation of the catechol molecules. The smaller gold working electrode is only present to make contact with the ITO layer that will be deposited over the top of it and up the sidewall. This is displayed more clearly in figure 2.12. The alignment of these electrodes with the channel is crucial because any changes to the exposed areas of the electrodes will alter the deposition rate of the chitosan as well as the oxidation rate of the catechol.

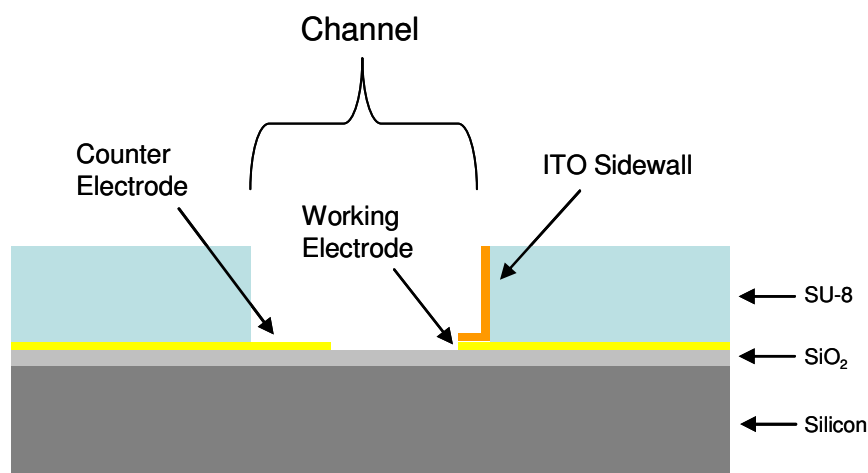


Figure 2.12: Side view of channel with control and sensing electrodes shown. The ITO film is patterned over the sensing electrode and up the wall.

The counter electrode is made larger than the working electrode to create a higher current density at the cathode surface during the chitosan deposition which results in a higher deposition rate. The electrodes were spaced directly across from one another in the channel for two reasons. The close proximity of the electrodes works to increase both the deposition rate of the chitosan and the oxidation rate of the

catechol due to the lower resistance which increases the surface potential. The second reason is to facilitate easier chitosan deposition since a single droplet of chitosan can be used to cover both electrodes for a reduced sample volume as described more in section 3.5.1.

2.4.2 Indium Tin Oxide (ITO) Sidewall

Indium Tin Oxide is a wide-bandgap semiconductor which combines relatively high conductivity with optical transparency for visible wavelengths. It is used for a variety of device applications including liquid crystal and flat panel displays, organic light emitting diodes and solar cells [96, 97]. It is also commonly used as bragg reflectors in lasers and other such applications due to its high reflectivity of light in the IR range. There is always a trade-off between the conductivity and the transparency of ITO films. The conductivity is determined from the number of charged carriers which are either electron or oxygen vacancies, but more carriers also increases photon absorption.

ITO can be readily implemented with MEMS devices using standard microfabrication techniques. It can be sputtered to create thin films and etched using a standard etching chemistry of hydrochloric acid or any other strong acid.

A plot of the attenuation through ITO vs wavelength is shown in figure 2.13 with data used from [98].

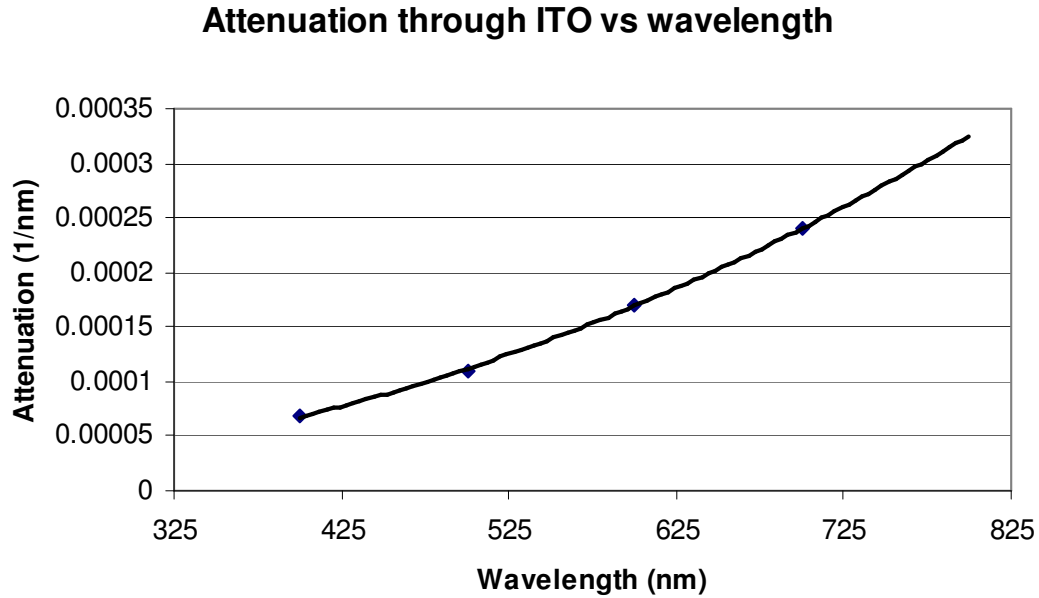


Figure 2.13: Attenuation of light through ITO based on wavelength. Data is used from [97].

It should be noted that the general trendline that is plotted would not accurately describe the attenuation in the UV range. The absorbance through ITO sharply increases for UV wavelengths of light. However, from this observed trend in the visible range of wavelengths, blue light at 472 nm has an attenuation of $1 \times 10^{-4} \text{ nm}^{-1}$. Since the ITO film thickness for our device is about 200 nm, this corresponds to an absorbance of .0087 or a transmittance of 98%. Although transmittances through ITO can vary based on the specific deposition parameters, this analysis indicates that the loss due to absorbance through the ITO is not a concern and is far less than other loss mechanisms in the device. The sheet resistance of the ITO is discussed in more detail in the fabrication section as it is strongly related to certain fabrication procedures used.

2.5 Fiber Clamp Structures

In order to make the coupling of the fibers to the SU-8 waveguides easier, structures were designed to hold the fibers in place while an adhesive strip of tape was placed to secure the fiber. The clamp structures have been used in past designs of the biophotonics platform [82, 83]. The fiber sits in a patterned groove in the SU-8 that is made about 25 μm wider than the diameter of the fiber itself. This is due to swelling of the SU-8 which typically occurs during the fabrication. Figure 2.14 shows a fiber sitting within one of these fiber clamp structures. It is important during the fabrication to keep the fiber channels as clear as possible since any debris can cause misalignment of the fiber end with the waveguide facet.

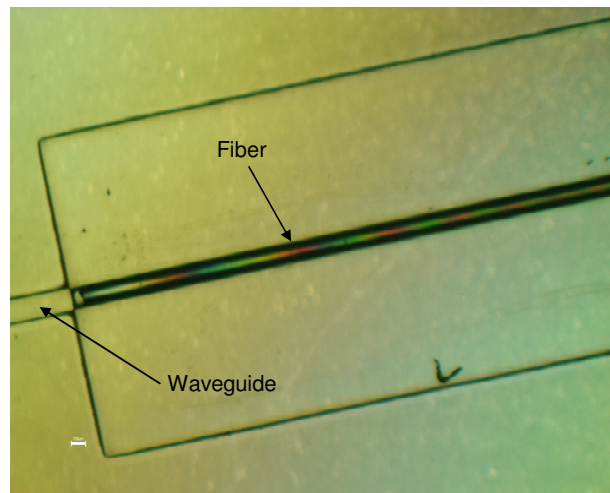


Figure 2.14: Fiber clamp structure shown with optical fiber placed in the groove.

2.6 Capping Layer

In order to seal the microfluidic channel, a capping layer is needed. A transparent material is ideal in order to receive visual confirmation of the liquid flow and any other actions taking place in the channel. Typical hard layers usually

incorporate a glass cover with a flexible polymer film on one side in order to effectively seal over the patterned structures of the chip. It can be difficult to drill small enough holes through the glass and this type of capping layer usually requires some sort of external pressure applied in order to seal. For our device, we used a thick layer of the flexible polymer PDMS. The PDMS effectively seals over any non-uniform surface and the relatively large size of our channels yields a low liquid pressure which is not sufficient to break the bond between the PDMS and the SU-8. Furthermore, it is much easier to create liquid inlet and outlet ports through the PDMS. Metal capillaries can be inserted through the polymer which seals around the intruding capillary and prevents any leakage.



3 Device Fabrication


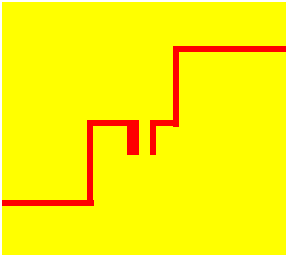

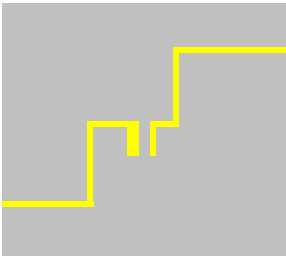

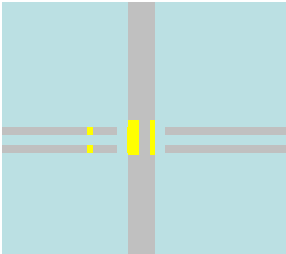
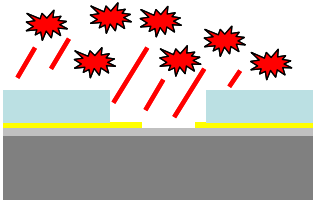
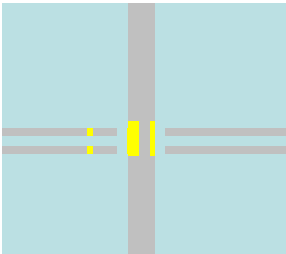
This section will describe in detail all of the fabrication procedures for the device. All of the fabrication steps were performed either at the cleanroom in the MEMS Sensors and Actuators laboratory, or at the FabLab in the Jeong H. Kim building at the University of Maryland in College Park. The first section will display the entire process flow from start to finish while the proceeding sections will discuss each of the main fabrication steps in more detail.

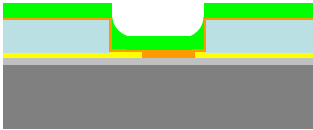
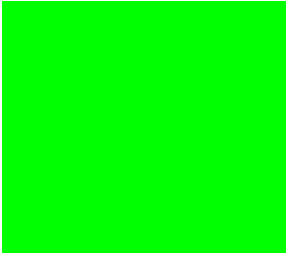

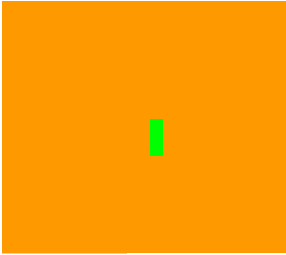

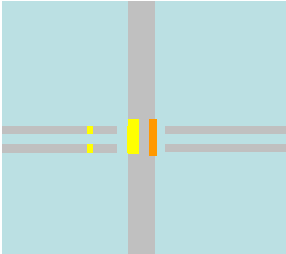

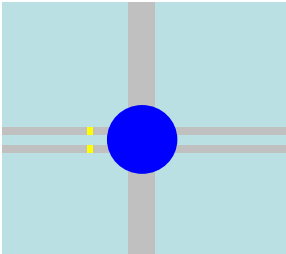
3.1 Process Flow


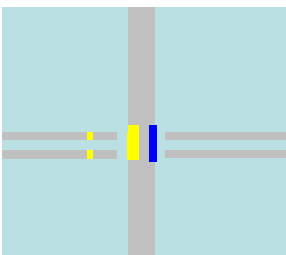
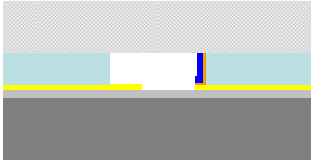
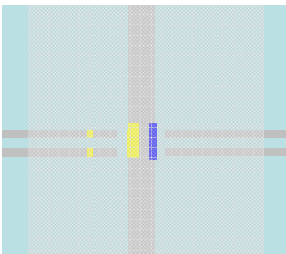
Table 3.1 gives the full process flow with cross sections and top views of the device during each fabrication step. Note that the views are not to scale and do not display an accurate representation of the entire chip. For clarity, only a blown up section of the sensing area in the channel is shown.

Table 3.1: Device process flow

Side View	Top View	Description
<p>(1)</p> 		<p>Begin with <100> orientation silicon wafer with 1 μm thermal oxide grown on top surface.</p>

Side View	Top View	Description
(2)		
		200 Å of Cr and 2000 Å of Au are sputtered on the wafer. Shipley 1813 photoresist is patterned on top using Mask 1 (Appendix).
(3)		
		Exposed gold is etched using Transene Au etchant. Photoresist is then stripped in acetone.
(4)		
		Spin AP300 adhesion promoter then spin SU-8 on the wafer and pattern using mask 2 (Appendix) to create the channel and waveguides
(5)		
		Etch the AP300 using BOE and clean the wafer extensively using Acetone, Methanol and IPA

Side View	Top View	Description
(6)		
		Sputter 200 nm of ITO over wafer, then spin photoresist (AZ9245) which also covers the sidewall as seen in the side view.
(7)		
		Pattern the photoresist using mask 3 (Appendix) so that only a sidewall portion of the resist remains in the channel
(8)		
		Etch the exposed ITO using 1:1 HCl:DI water then strip the photoresist using acetone.
(9)		
		Place a droplet of chitosan over the electrodes in the channel and apply a voltage bias between the electrodes as shown

Side View	Top View	Description
(10)		
		After voltage application, wash the remaining chitosan away in DI water leaving behind a sidewall deposited film
(11)		
		A layer of PDMS is bonded over the channel using methanol to complete the device

Following the fabrication procedure detailed in Table 3.1, optical fibers are secured in place on either end of the device using an adhesive strip. The liquid inlet and outlet ports are formed by first puncturing two holes in the PDMS layer using a needle, then placing metal capillaries with an outer diameter of 400 μm and inner diameter of 200 μm into the holes. The elastic nature of the PDMS allows the polymer to seal around the capillaries and no leakage occurs around the edges. Tygon flexible tubing with inner diameter of 380 μm is placed around the ends of the capillaries, again, with no leakage detected. The complete packaged device is shown in figure 3.1.

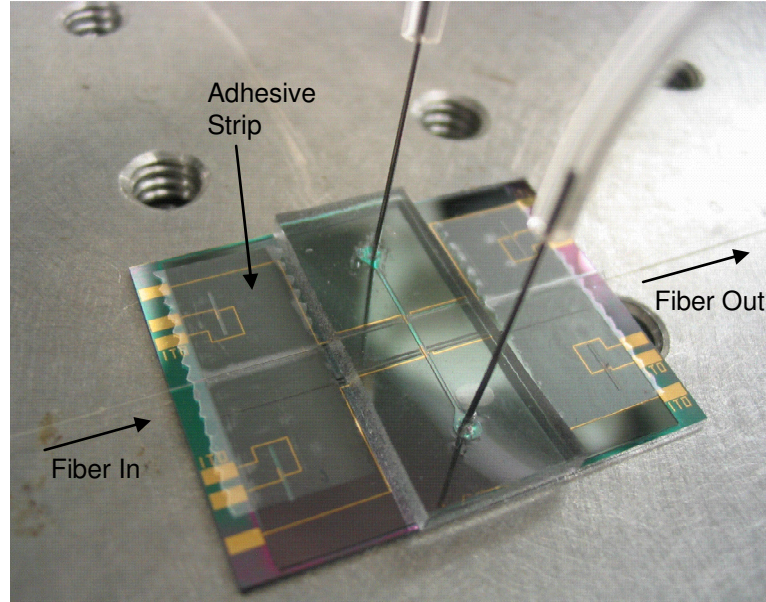


Figure 3.1: Fully packaged device

3.2 Electrode Patterning

This section discusses in more detail the deposition and patterning of the metal layers on the device. The metal was sputtered onto the silicon wafers using an AJA Magnetron sputtering system at the University of Maryland Fablab. Argon plasma excited at 200 watts using a DC power supply was used to bombard the metal targets. The wafer surface was cleaned prior to sputtering the metal using the argon plasma excited at 20 W and a chamber pressure of 5 mTorr for 5 minutes. The sputtering conditions for each metal are shown below in table 3.2.

Table 3.2: Metal Sputtering Conditions

	Chrome	Gold
Chamber Pressure	10 mTorr	10 mTorr
Argon Gas Pressure	20 sccm	20 sccm
Supplied DC Power	200 W	200 W
Sputter Rate	12 nm/min	30 nm/min
Final Thickness	20 nm	200 nm

Following the metal deposition, the wafers were patterned in the MSAL cleanroom. Standard lithography practices were performed using Shipley 1813 photoresist which achieves a final thickness of 1.6 μm after being spun on the wafer using a Spincoater P6700 from Specialty Coating Systems Inc. Hotplates from Torrey Pines Scientific were used for all of the baking steps. All of the lithography steps for the metal patterning are described in more detail in table 3.3.

Table 3.3: Metal Patterning Procedure

Step	Parameters	Description
Spin Photoresist	3000 RPM, 30 sec	Achieves thickness of 1.6 μm across the wafer
Bake	100 C, 60 sec	Evaporates solvent from resist
Expose	190 mJ/cm ² @ 405 nm	Expose resist using Mask 1 (Appendix A)
Develop	30 sec	Use Microposit 351 developer, rinse with DI water afterwards
Etch Au	2 min, mild agitation	Etch exposed gold using Transcene Au etchant
Etch Cr	30 sec, mild agitation	Etch exposed chrome using Transcene Cr etchant
Strip Photoresist		Rinse with acetone, methanol, IPA

3.3 SU-8 Recipe Development

Most of the work in fabricating the devices went into developing the final SU-8 recipe. The standard procedure for patterning SU-8 as suggested by Microchem was found to be insufficient. The reasons involved both problems with the final uniformity of the film, and more importantly, the adhesion of the SU-8 to the wafer.

The many problems encountered involving the SU-8 delaminating from the wafer were attributed both to the relatively large footprint of the devices and also to the large mismatch in the coefficient of thermal expansion of both the SU-8 and silicon. Table 3.4 details the final SU-8 processing recipe while the following sections give more detail into the uniformity and adhesion problems encountered throughout its development.

Table 3.4: SU-8 recipe

Step	Parameters	Description
Spin Adhesion Promoter	5000 RPM, 60 sec	AP300 promotes better adhesion of SU-8 to oxide surface
Bake	150 C, 15 min	Evaporates AP300 residues
Spin SU-8	600 RPM Ramp: 5 sec Time: 10 sec 1150 RPM Ramp: 3 sec Time: 27 sec	Spin parameters used to create uniform film ~ 100 μm thick
Pre-Bake	55 C Ramp: 300 C/hr Time: 120 min	Pre-bake used to evaporate solvent. Let wafer cool afterwards for 2 hours
Exposure	2500 mJ/cm^2 @ 405 nm	Expose using Mask 2 (appendix A)
Post-Bake	55 C Ramp: 300 C/hr Time: 90 min	Crosslinks the exposed resist. Let wafer cool afterwards for 2 hours
Develop	10 min, agitation	Develop resist in PGMEA developer. Rinse with IPA afterwards
Etch TiO_2	BOE 50:1, 3-5 min	Etch rest of adhesion promoter residues

3.3.1 SU-8 Uniformity

Uniformity of a thick resist such as SU-8 across a wafer is always a challenge to achieve. At best, one can expect variations on the order of about 10 μm from the

center of the wafer out to about a centimeter from the edge. The resist on the outer edge of the wafer is usually much thicker due to the “edge bead effect”. This effect is caused by the spinning process since the resist is spread radially outward on the wafer and thus can accumulate at the edge. However, the uniformity of the SU-8 during the processing of these devices was found to vary radically during the early stages of development. In some cases, the thickness could vary by as much as 50 μm . Sealing the PDMS layer over the channel is difficult if the resist is highly non-uniform, and furthermore there are constraints on how tall the waveguides can be. The thickness of the SU-8 must lie between 90 μm and 125 μm . If it is too thin, the fiber core will not completely line up with the waveguide facet. If it is too thick, the fiber will “float” in the clamp structure and cannot be adequately secured.

At first, the uniformity issues were attributed to the hotplates themselves. The surfaces were old and had areas with caked on photoresist. An irregular temperature profile across the wafer can cause the resist to have a final non-uniform thickness. In an attempt to circumvent this problem, a box furnace was used for the baking procedures of a few of the wafers. However, it was difficult to get the wafer to sit perfectly flat in the furnace, and as a result, the resist would slope slightly to one side.

The eventual solution to the problem was to use silicon wafers with an oxide coating instead of Pyrex glass wafers. Originally, the attempted fabrication of the devices used Pyrex wafers as the substrate. The switch to using silicon wafers alleviated the uniformity issue because the silicon acted as a good thermal conductor and spread the heat applied from the hotplate evenly across the whole wafer.

Using silicon wafers was also found to have another key advantage. Much better lithography contrast with the SU-8 was achieved on the silicon wafers as opposed to the Pyrex wafers. Figure 3.2 shows microscope images of the fiber channels patterned on a Pyrex and silicon substrate. The residues which appear with the Pyrex wafer are most likely due to reflections of the UV light through the wafer which can cause some of the SU-8 to crosslink even under areas where the mask is opaque overhead. In the channels, the residues ranged from 2 to 5 μm in thickness which is enough to disrupt the fibers from sitting cleanly in the channel.

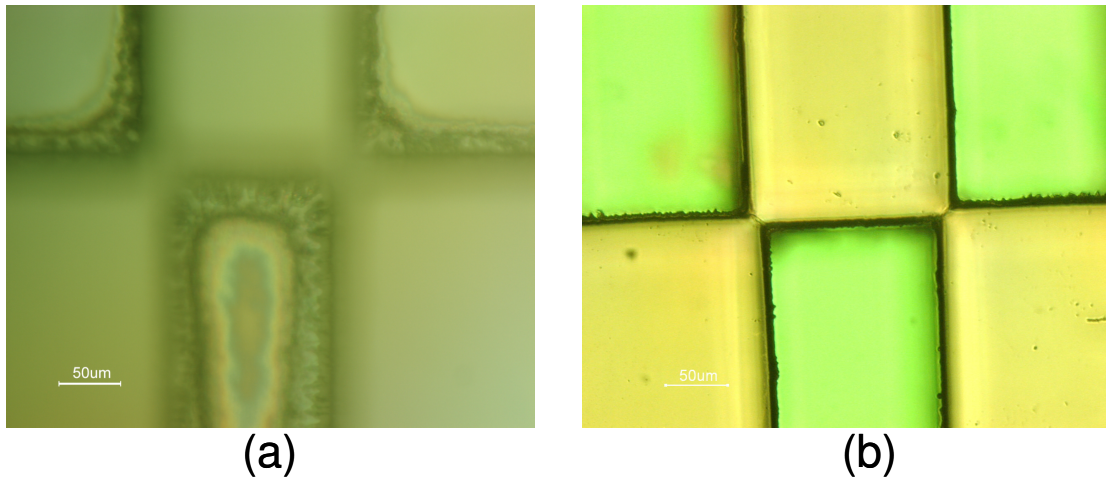


Figure 3.2: (a) end of fiber clamp on a Pyrex wafer showing SU-8 residues in the channel and (b) the same area on a silicon wafer showing clean channels.

3.3.2 SU-8 Adhesion

The largest challenge faced during the fabrication of the devices was ensuring that the SU-8 did not delaminate during the processing. Further complicating this is that even if just the edge of the SU-8 is not making contact with the wafer, it can break the electrical connection between the ITO sidewall and the electrode patterned in the channel.

Adhesion of SU-8 to oxide surfaces is known to be poor, which is why an adhesion promoter (AP300, Silicon Resources, CA) is first spun on the wafer before the SU-8 is applied. The baking of the AP300 is performed to remove residues that are otherwise left behind and the procedure was developed previously for the first generation of biophotonics devices [81].

In some cases, the SU-8 adhesion would appear to be fine after the patterning and development of the resist itself. However, after patterning the ITO, the adhesion would suddenly fail at numerous points around the wafer. The adhesion problems are believed to be related to the large difference in the coefficient of thermal expansion between the SU-8 and the silicon wafer. The coefficient of thermal expansion is related to the stretching of the material due to temperature changes as shown in equation 3.1.

$$\alpha = \frac{1}{L_0} \frac{\delta L}{\delta T} \quad (3.1)$$

Where L_0 is the original length, L is the new length and T is the temperature. Heating and cooling of a material causes the bond lengths between atoms in the crystal structure to either expand or contract which will cause stress between two materials that undergo different levels of stretching. The CTE of SU-8 is 50 ppm/°C while silicon is only 3 ppm/°C [99]. It is for this reason that every heating step during the processing is slowly ramped to the final temperature and allowed to cool slowly. Also, the heating of the SU-8 resist was lowered to 55° C for both the pre-bake and post-bake steps to avoid higher temperatures as much as possible. In some cases, the poor adhesion of the SU-8 to the wafer can be seen under the microscope as shown in

figure 3.3. However, other times the poor adhesion may only exist at the edges and can only be detected using SEM imaging as seen in figure 3.4.

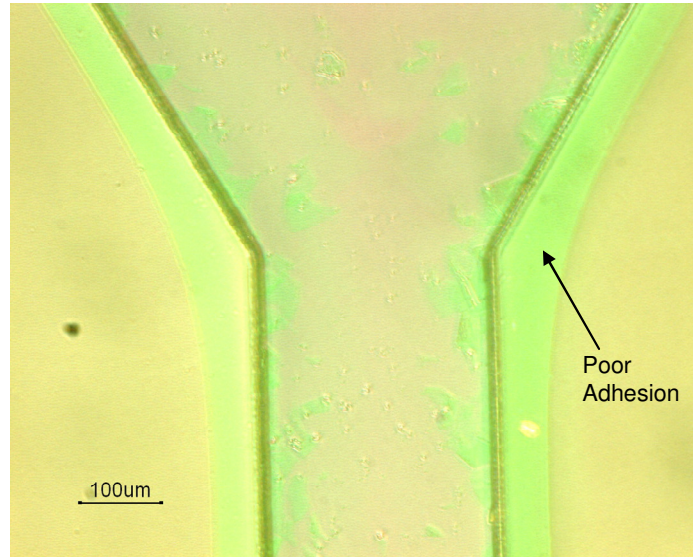


Figure 3.3: Discoloration around the edges of the SU-8 signifies poor adhesion.

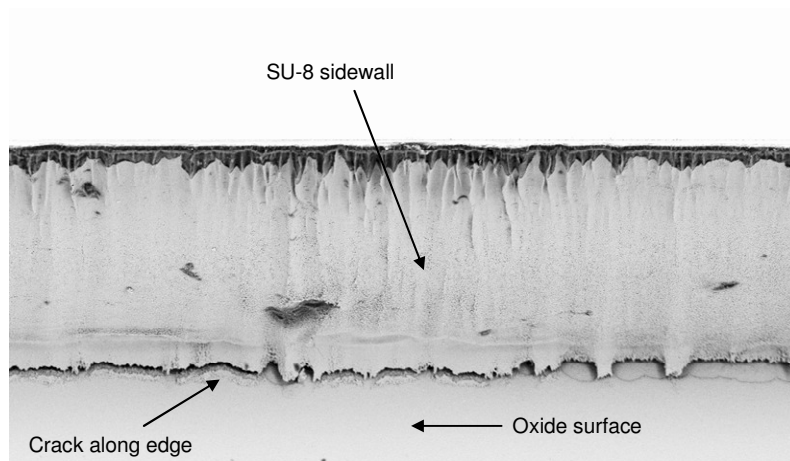


Figure 3.4: SEM image of an SU-8 sidewall displaying the adhesion crack between the resist and the wafer that has formed.

The processing steps involving the heating of the AZ9245 photoresist during the ITO patterning were also altered from the conventional recipe used for that type of resist in order to reduce the stress once again between the SU-8 and the silicon

wafer. Other than the problems with adhesion, no other common problems such as stress cracks or “T-topping” of the resist sidewalls were encountered when using this recipe.

3.4 ITO Patterning

The recipe used for spinning AZ9245 photoresist so that it adequately covers the sidewall channels was first developed in [81], but the heating conditions were changed for these devices to promote better adhesion. The exposure dose is extremely high for a resist with a typical thickness of about 9 μm because the resist can get as thick as 100 μm in vertical height as it covers the SU-8 sidewalls. The processing recipe is given below in table 3.5.

Table 3.5: Recipe for AZ9245 photoresist and ITO patterning

Step	Parameters	Description
Spin resist	RPM: 350 Time: 5 sec RPM: 1000 Ramp: 3 sec Time: 40 sec	Apply AZ9245 evenly across the entire wafer before spinning
Bake	75 C Ramp: 300 C/hr Time: 45 min	Allow wafer 2 hours to cool afterward
Expose	3780 mJ/cm ² @ 405 nm	Expose using Mask 3 (Appendix A)
Develop	3:1 DI:AZ400K, 5 min	
Etch ITO	1:1 HCl:DI, 30 sec	Check wafer every 10 sec
Strip resist		Rinse with Acetone, Methanol, IPA

3.4.1 AZ9245 Sidewall Profile

It was important during the first fabrication runs to ensure that the photoresist was adequately covering the sidewall and that it was not beginning to peel off of any areas. The concern arises from the fact that the temperature for baking the resist was drastically lowered from the conventional 110 °C to 65 °C for an extended period of time. Thus, if the solvent was not fully evaporated, it would have a negative effect on the consistency of the resist after patterning. In order to achieve better views of the resist after spinning, SEM images were taken of the sidewalls as shown in figure 3.5 after the AZ9245 photoresist has been patterned. Figure 3.6 displays the etched ITO after the resist has been stripped.

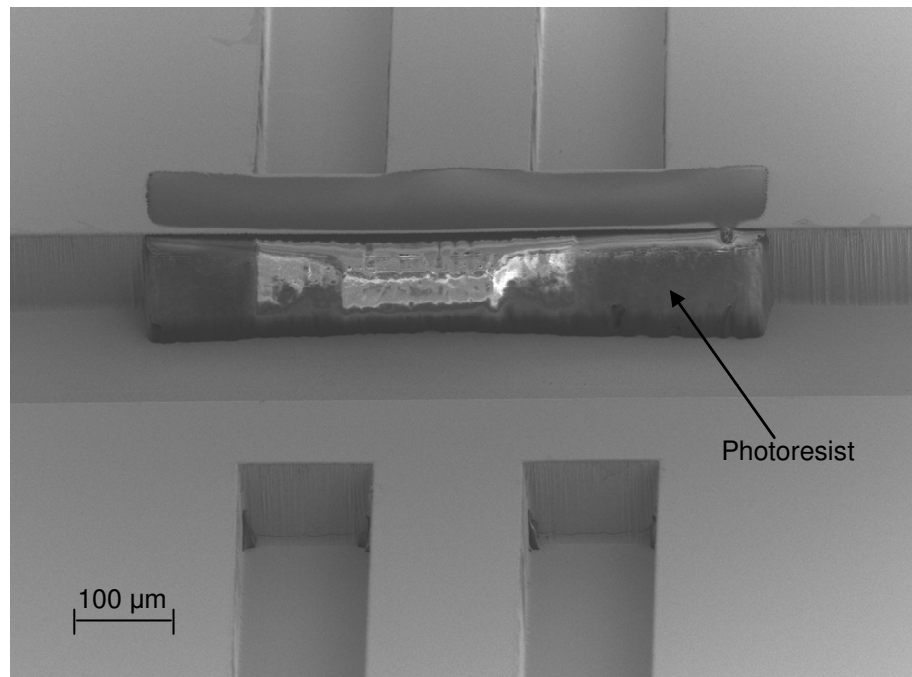


Figure 3.5: SEM displaying patterned photoresist on the sidewall.

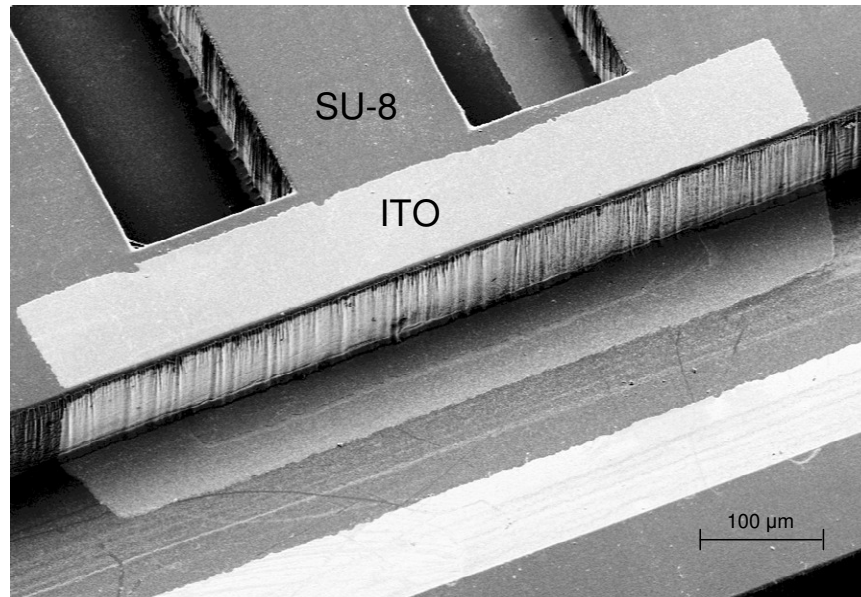


Figure 3.6: SEM image of ITO patterned on the SU-8 sidewall.

The ITO film is also present on the top of the SU-8 as seen in the figure but does not make electrical connection to the sidewall since the resist does not adequately cover the convex angle at the top edge of the SU-8. The mask covers this area in order to ensure that the photoresist on the sidewall is protected from any stray UV light during the long exposure.

3.4.2 ITO Conductivity

In order to measure the conductivity of the ITO, test structures were patterned on the wafer which consisted of 3 gold contact pads connected by ITO strips of varying width to validate the calculated conductivity data. More important was the discovery of whether or not the presence of the adhesion promoter (AP300) caused too much resistance between the gold and ITO. Although residues of the AP300 are baked off during processing, nanoparticles of TiO_2 still remain and may cause an open circuit between the gold working electrode and the ITO patterned up the

sidewall. To test the effect that the adhesion promoter has on the conductivity, two wafers were fabricated, one in which the TiO_2 was etched away using BOE 50:1 as detailed in the processing steps from table 3.4, and another wafer which did not include the etch step for the TiO_2 . The voltage between gold contact pads connected by the ITO strips was measured for various applied currents and the results for both wafers are shown in figure 3.7.

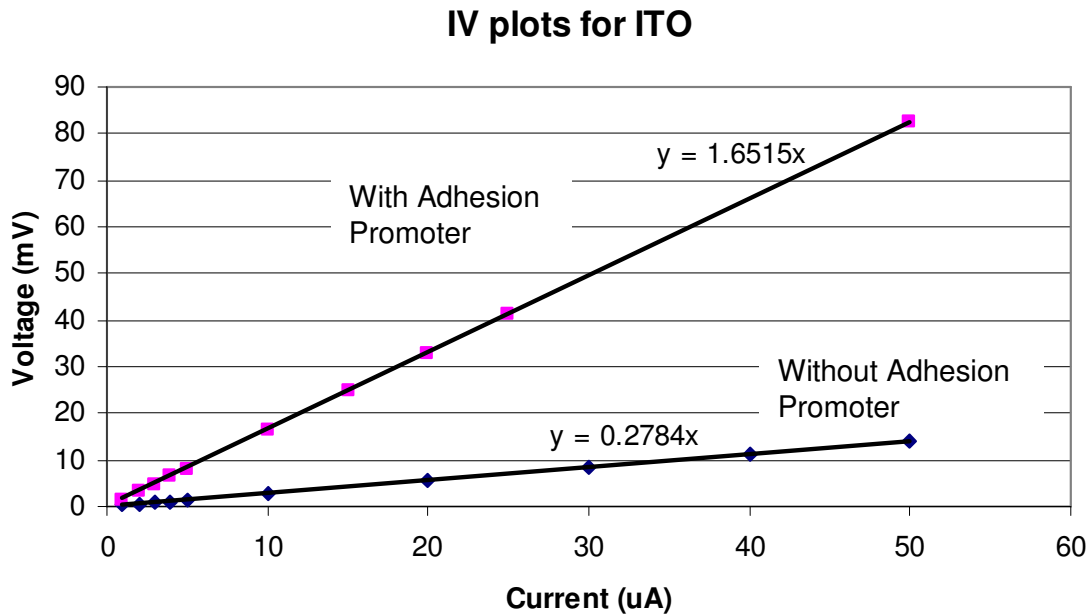


Figure 3.7: IV plots for ITO strips $240\ \mu\text{m} \times 2000\ \mu\text{m}$ with and without the adhesion promoter present on the wafer.

The given slopes of each line designate the measured resistance between the contact pads. It is clear that the resistance is much higher for the wafer which still had the adhesion promoter on it before the ITO was deposited. A better comparison is the measured sheet resistivity between the ITO on the two wafers. The sheet resistivity is calculated from knowing the resistance and dimensions of the film strip as shown in equation 3.2.

$$\rho_s = \frac{R * W}{L} \quad (3.2)$$

Where R is the measured resistance from the IV plot, W is the width of the ITO strip and L is the length of the ITO strip. Taking the dimensions of the ITO as 240 μm x 2000 μm , the measured sheet resistivity of the ITO is 198.18 Ω/\square and 33.41 Ω/\square for wafers with and without the adhesion promoter respectively. The sheet resistivity of the ITO appears to increase on the wafer with the adhesion promoter due to an increase in the contact resistance caused by the TiO_2 nanoparticles. It is clear that the presence of the adhesion promoter does cause an unwanted voltage drop to occur which can cause problems with both the chitosan deposition and oxidation of the catechol. This is why it is important to include the extra etching step of the adhesion promoter after patterning the SU-8. A sheet resistivity of 33.41 Ω/\square is close to what has been previously reported in literature for ITO films of similar thickness [98].

3.5 Die-level Processes

After the patterning of the ITO has been completed, the six individual dies on the wafer were diced using an automated dicing saw for testing. The final steps taken to complete the device including the chitosan deposition, PDMS bonding and fiber attachment were all easier to perform at the die level.

3.5.1 Chitosan Deposition

Chitosan can be a complicated compound to work with because it is very difficult to achieve repeatable results from trial to trial. This can be attributed to the

rather amorphous polymer structure of the material and to the fact that every batch of chitosan can respond differently to applied stimuli. Furthermore, with these devices the electrode surface is not uniform due to the roughness of the SU-8 sidewall on which the ITO is deposited. Also, the 90° angle made from the ITO sidewall to the working electrode patterned in the channel creates a highly non-uniform electric field which causes more chitosan to deposit in the corner than further up the sidewall.

Nonetheless, the goal was to achieve a chitosan thickness on the sidewall of about 10 μm . In order to find the correct current density to apply in order to achieve a good deposition, chitosan droplets were applied over the test channels around the outside of the device and currents of varying amplitudes were applied for 10 minutes each. The chitosan was prepared with the help of Angela Lewandowski from Dr. Bentley's lab at the University of Maryland in order to create a 0.5% W/V solution at a starting pH of 5.3. A droplet of the chitosan solution was placed over the control and sensing electrodes using a 10 μl syringe prior to the different currents being applied. Applied currents of 0.35, 0.5, 1 and 1.5 μA were applied to four different sets of electrodes and the resulting sidewall depositions of chitosan are shown in the SEM images shown in figure 3.8.

It is clear that the geometry causes very non-uniform depositions. Applying a current of 0.35 μA corresponds to a current density of 4 A/m^2 given the electrode dimensions in the channel. A 4 A/m^2 current density has been previously shown to result in uniform thin film deposition of chitosan [100]. The thicker depositions which occur for 0.5 and 1 μA of applied current could be problematic if the crosslinking of the chitosan chains due to the catechol oxidation causes the chitosan

to shrink thus changing its surface morphology by a great amount. The increased current ($1.5\ \mu\text{A}$) is clearly too high since bubble formation due to the formation of hydrogen gas at the cathode has disrupted the deposition of the chitosan and formed the “cave-like” structure of chitosan as shown.

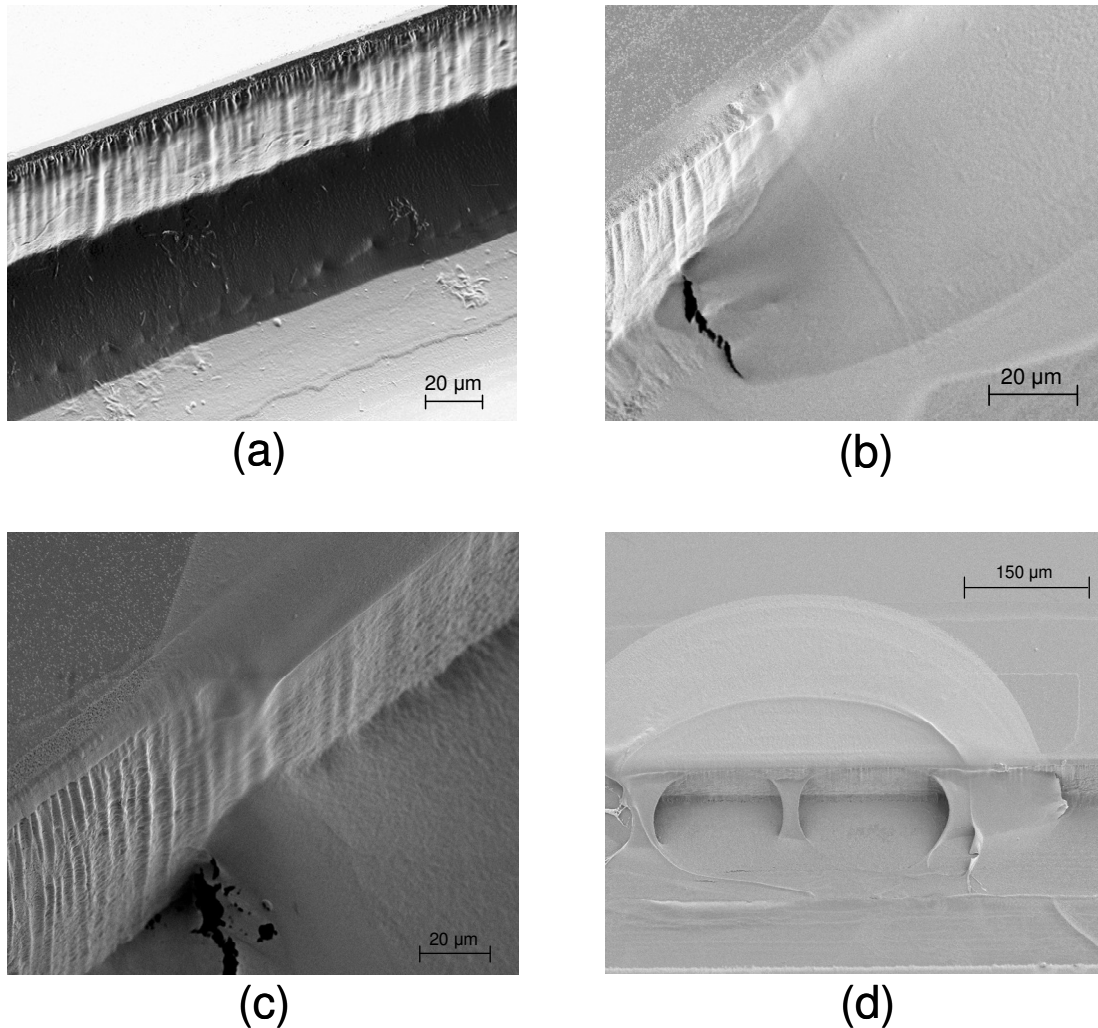


Figure 3.8: SEM images of chitosan deposition with an applied current of (a) $0.35\ \mu\text{A}$, (b) $0.5\ \mu\text{A}$, (c) $1.0\ \mu\text{A}$ and (d) $1.5\ \mu\text{A}$ for a 10 minute reaction time.

After performing the chitosan deposition tests, $0.35\ \mu\text{A}$ was used to deposit all of the chitosan films for the actual testing with the catechol. When applying these films, a microscope could be used in some cases to actually see the sidewall of

chitosan as shown in figure 3.9. After every deposition, the remaining chitosan solution was washed away with DI water and the film was neutralized in a 1 M solution of sodium hydroxide.

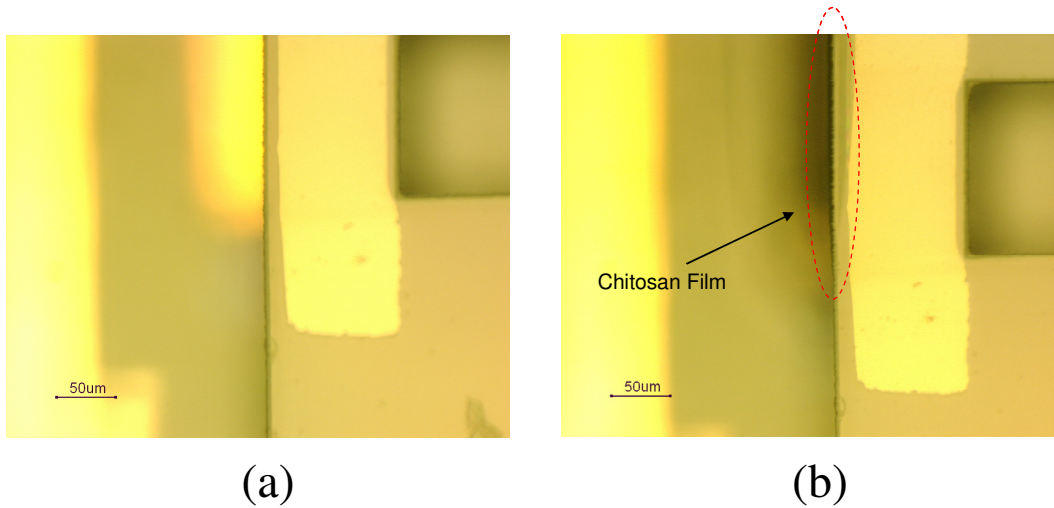


Figure 3.9: Microscope image of sidewall focused at the top of the SU-8 resist (a) before and (b) after chitosan deposition.

3.5.2 PDMS Bonding

Thick PDMS at least 1 mm in height is formed through the mixing of a Sylgard silicone elastomer and curing agent both purchased from Dow Corning. The two materials are mixed in a 1:10 ratio of curing agent to elastomer for about 3 minutes in a 40 mL beaker. After mixing, all of the trapped gas is removed from the solution by placing the beaker in a vacuum bell jar. This process takes about 30 minutes to thoroughly expel all of the trapped air.

The mixed solution is poured onto a flat plate and placed in a box furnace for 25 minutes at 80 °C in order to cure the PDMS. After the furnace has cooled to room temperature, the PDMS is removed and can be cut into smaller pieces using a razor blade. In order to bond the piece of PDMS to the device, both surfaces are thoroughly

cleaned with acetone, methanol and IPA then blown dry with nitrogen. After the cleaning, methanol is applied to one side of the PDMS which is then placed over the device. The methanol allows for the PDMS to be slid into the correct position and then can evaporate out through the permeable PDMS layer. Once evaporated, the PDMS is bonded weakly to the SU-8, however, the bond is still strong enough to withstand the liquid pressures generated in the microfluidic channel.

3.5.3 Optical Fiber Preparation

Multimode optical fibers with core diameter of 62.5 μm and outer diameter of 125 μm are first prepared by stripping about 4 inches of the buffer layer off of the end. The exposed bare fiber is wiped with IPA to remove any pieces of the buffer material which may still cling to the fiber. Once cleaned, the fiber is placed in a manual fiber cleaving device and cleaved to leave only 12 mm of the bare fiber at the end. The fiber is carefully placed into the fiber clamp structures of the device under a stereomicroscope and secured with a single piece of tape.

Originally, UV cured epoxy was used to secure the fibers, but this was changed to using tape for two reasons. First, the epoxy could easily flow between the fiber facet and the waveguide facet which could scatter the light if any bubbles were present in the glue. Secondly, the bonding of the fibers with the glue was permanent and any misalignment prevented the device from being reused.

4 Testing and Results

Testing the effects of the catechol oxidation on the absorbance through the chitosan film was divided into two main procedures. The first was to use chitosan films cast onto glass slides and measure the absorbance change using a benchtop UV-VIS spectrophotometer. The second was to deposit chitosan films in the MEMS device and measure the absorbance change using light coupled through the SU-8 waveguides. The experiments using slides allowed for a better understanding of how parameters such as time and catechol concentration affected the final absorbance measurement. These results could then be compared to those achieved with the MEMS device.

4.1 Slide Absorbance

4.1.1 Testing Apparatus

All of the experiments using chitosan cast onto slides were performed at the MEMS Sensors and Actuators Lab while the absorption spectrums were analyzed using a GENESYS2 spectrophotometer from Dr. Payne's laboratory (Biochemical Engineering Lab) at the University of Maryland. The catechol flakes were purchased from Sigma Aldrich (part #C9510) and dissolved in a 20mM phosphate buffer solution at a pH of 5.3 in order to create the catechol solutions for testing. A 0.1 M solution of catechol was created by adding 0.22 g of catechol to 20 mL of buffer and mixing thoroughly. Lower concentration solutions of catechol were created by diluting a small amount of the 0.1 M catechol solution with more buffer solution.

Chitosan films were cast onto ITO coated slides. The ITO allows a current to oxidize the catechol molecules in proximity to the chitosan film while also allowing for optical transparency in the visible region. Chitosan with a W/V of 1.6% was used to cast the films in order to cast a thicker film on the order of about 10 μm . The casting procedure involved placing chitosan solution onto the ITO slides using a pipette and allowing the chitosan to dry on a hotplate set to 40 $^{\circ}\text{C}$. Once dry, the films were neutralized in a 1 M solution of sodium hydroxide for 5 minutes. The film on an ITO slide is seen in figure 4.1a

The testing setup involves clipping the chitosan coated ITO slide and a gold electrode using alligator clips into the beaker filled with the catechol solution as shown in figure 4.1b. The current is applied to the electrodes using a Keithley programmable current source and is set to apply a current density of 4 A/m^2 .

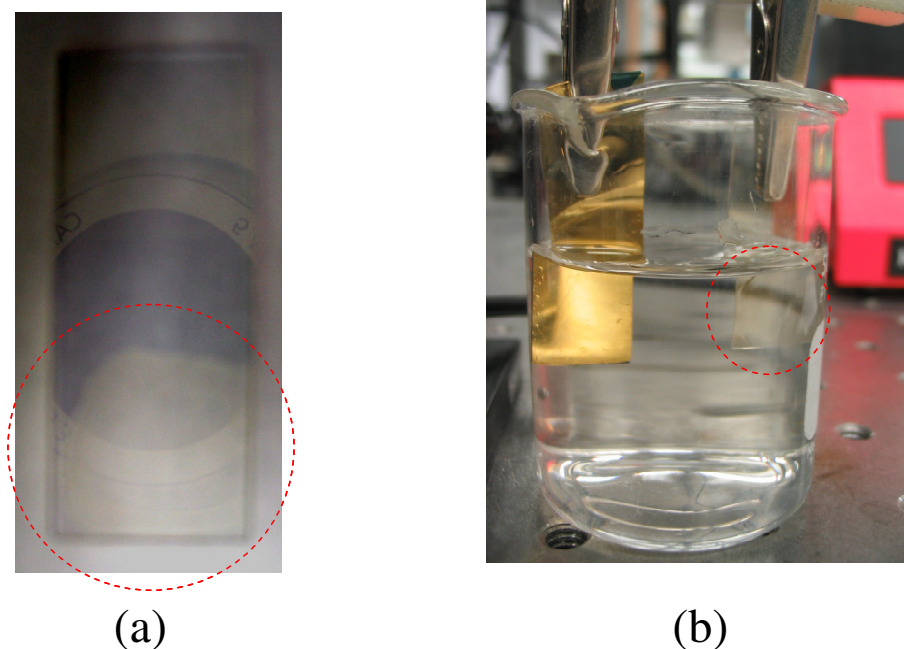


Figure 4.1: Red circles indicate the location of the chitosan film on both (a) the ITO slide and (b) within the full testing setup.

It was discovered through testing that attempting to oxidize lower concentrations of catechol (below about 10 mM) resulted in the destruction of the ITO film. It is believed that the ITO itself was being consumed in the oxidation reaction in the absence of the electrons being donated from the catechol molecules. In order to avoid this problem, chitosan was cast onto plain glass slides and clipped to a gold anode electrode so that it is in very close proximity to the anode where the catechol is being oxidized, but no longer relies on the integrity of ITO.

4.1.2 Slide Absorbance Results

Initial experiments kept the catechol concentration constant at 0.1 M and the current density at 4 A/m², varying only the time of the reaction to measure how the absorbance is affected over time. The result is shown in figure 4.2 using a blank glass slide as a reference for the absorbance measurements.

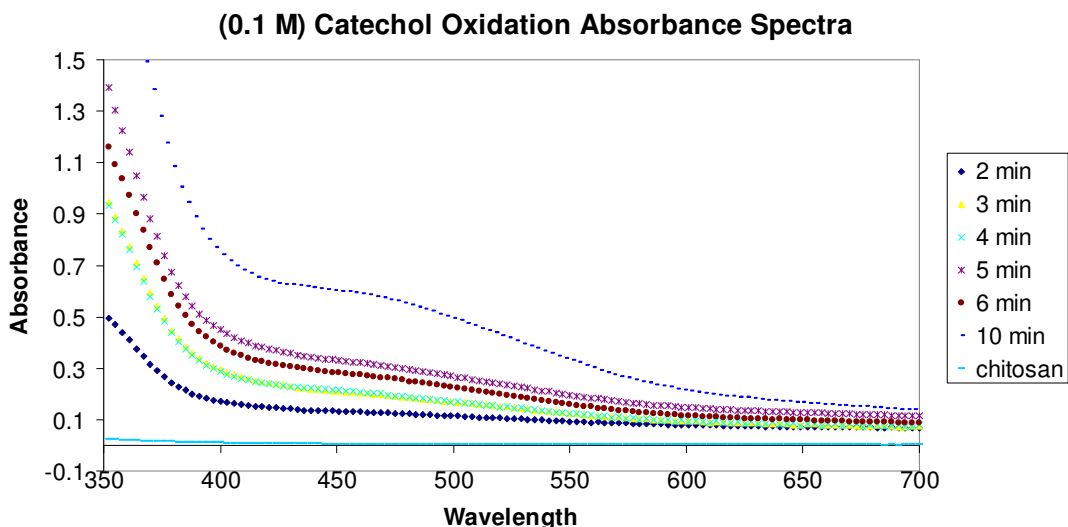


Figure 4.2: Absorbance spectra taken through chitosan films conjugated with o-quinones from catechol oxidation for various times.

As expected, the absorbance through the chitosan generally increases for an increasing reaction time and the absorbance is shown to be the highest in the UV and near UV range. Conversely, a control film of unreacted chitosan shows very little absorbance. The wavelength to be used is 472 nm due to availability of laser sources in the near UV spectral range. Figure 4.3 displays the absorbance vs. reaction time measurements only for a wavelength of 472 nm.

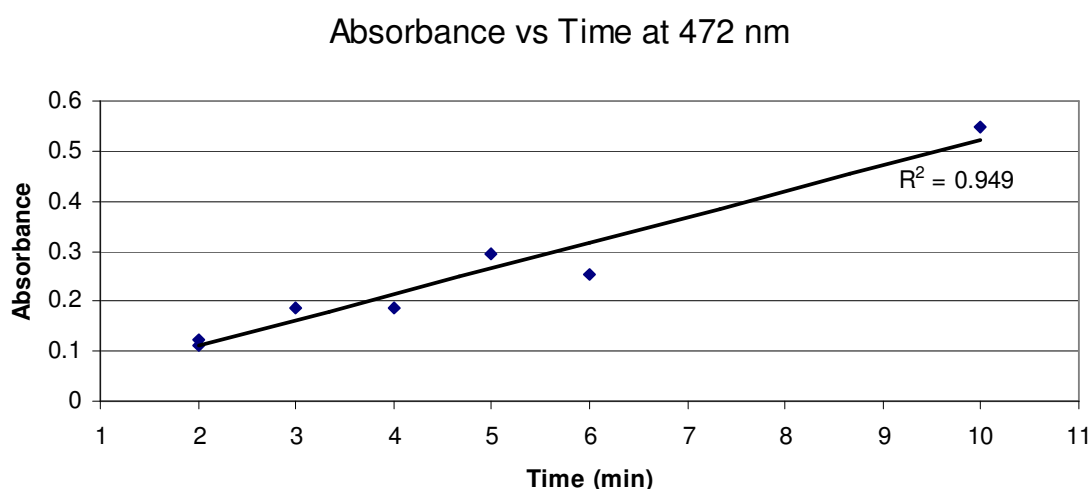


Figure 4.3: Absorbance through chitosan film for different reaction times at a wavelength of 472 nm.

The relationship of the absorbance with reaction time is nearly linear at a wavelength of 472 nm. This demonstrates that the chitosan amine groups are not saturating for reaction times lower than 10 minutes and that the accumulation of the generated *o*-quinones on the chitosan is fairly linear with time. Since a rather significant absorbance change is measured for a reaction time of 10 minutes without any noticeable saturation of the chitosan amine groups, I used this time for the rest of the experiments including those that are performed with the MEMS device.

The next experiment varied the concentration of the catechol in the solution while keeping the applied current density and reaction time constant. Chitosan films were subjected to various concentrations of oxidized catechol and the results from the spectrophotometer are shown in figure 4.4.

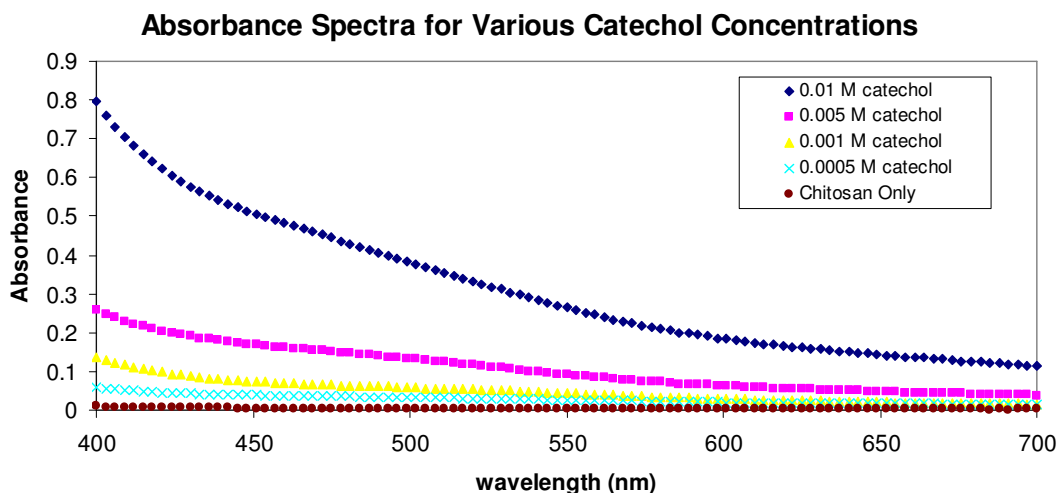


Figure 4.4: Absorbance spectra through chitosan films subjected to various catechol concentrations.

It is clear that increasing catechol concentration results in a higher absorbance as expected, particularly in the UV range. Figure 4.5 plots the absorbance vs. concentration at the chosen wavelength of 472 nm. This result shows that the absorbance increases linearly with concentration. This is consistent with the Beer-Lambert law which states that absorption is linearly proportional to the concentration of the absorbing species and should remain a linear relationship assuming that the free amine groups of the chitosan are not saturated. If saturation were to occur, the absorbance would reach a maximum state and not increase any further. Theoretically, since the thickness of the chitosan is the same for each trial ($\sim 10 \mu\text{m}$), after some long reaction time ($>10 \text{ min}$) all of the amine groups will be conjugated with *o*-

quinones and the absorbance through the chitosan films should become the same regardless of the starting catechol concentration.

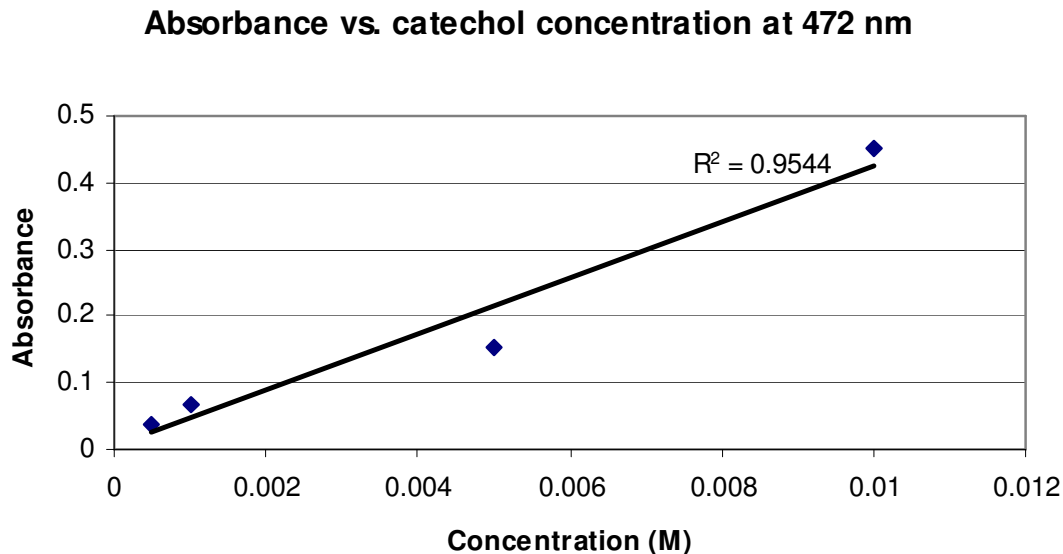


Figure 4.5: Absorbance vs catechol concentration at 472 nm displaying a linear-like response.

4.2 MEMS Sensor Testing

4.2.1 Testing Apparatus

Critical to the absorbance testing was a blue laser from Lasermate Group Inc. (part #BML-30F0-A) which provides a continuous wave (CW) beam centered at 472 nm with a maximum output power of 30 mW which was sufficient for our application. The laser was secured to a floating optical table to reduce vibrations and coupled into the cleaved end of a multimode fiber with core diameter of 62.5 μm using a manual xyz fiber alignment stage. A syringe pump (GENIE Plus) from Kent Scientific delivered the liquid samples at a set flow rate while two probes made electrical connection to the anode and cathode in the microfluidic channel. Measuring

the light intensity from the output fiber was performed with a USB2000 spectrophotometer from Ocean Optics connected to a computer for data acquisition. A block diagram of the entire testing system is displayed in figure 4.6 while figure 4.7 gives a photograph of the test setup.

For each experiment catechol was prepared in exactly the same way as described for the glass slide experiments from section 4.1.1. A 100 μl syringe from Cole-Parmer was used in the pump to administer the catechol solutions. Notice in figure 4.7 that the waste solution from the device was simply collected in a beaker downstream. Samples were taken every 50 ms and displayed the intensity vs. wavelength results with an integration over 10 collected samples.

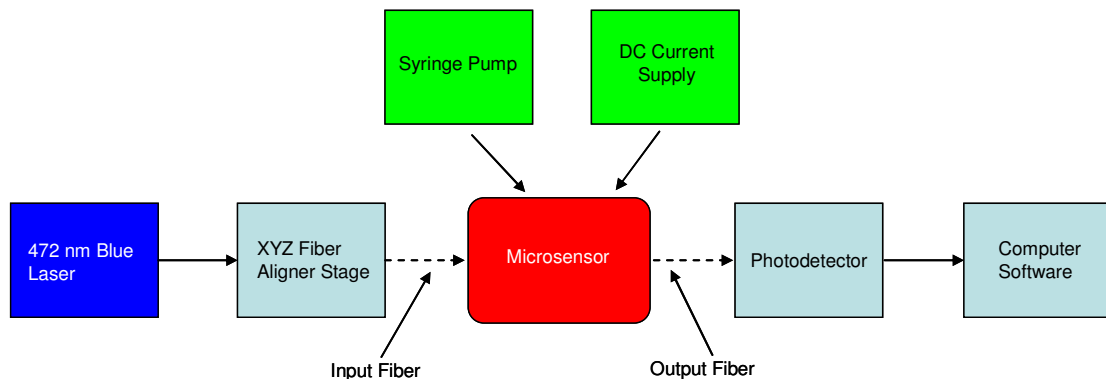


Figure 4.6: Block diagram of testing setup for the MEMS sensor.

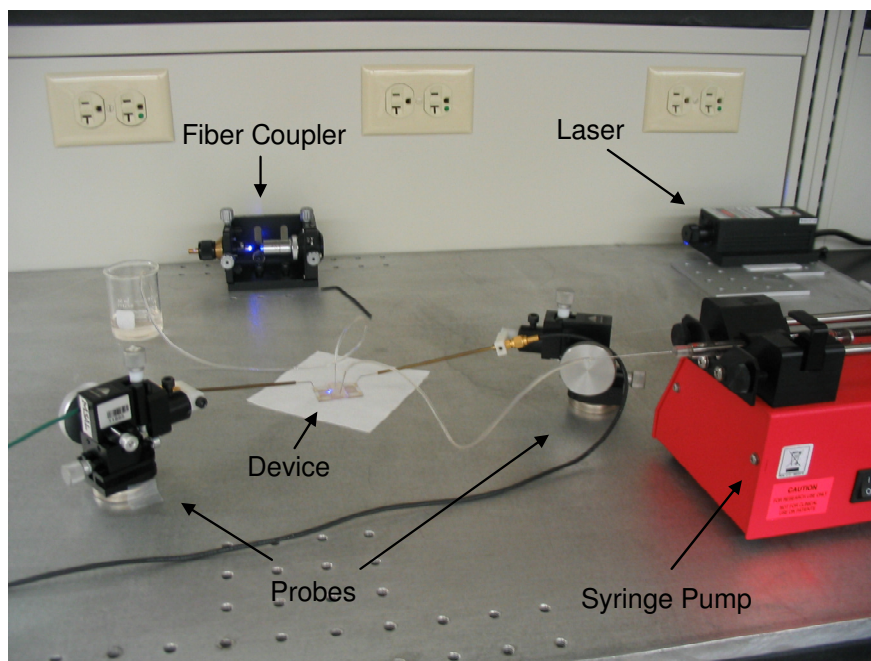


Figure 4.7: Photo showing full testing setup.

4.2.2 Total Optical Loss

Once the devices were fabricated, the total optical loss through the patterned waveguides could be calculated. The total can be used to estimate the loss due to the roughness of the waveguide facets since the other loss mechanisms have been previously calculated based on optical theory in chapter 2. The total loss was determined by first calculating the intensity measured through just the optical fiber alone. Using the alignment stage to couple as much power as possible, the total optical power through a single multimode fiber at 472 nm was measured to be 90 μW using a Newport optical power meter. This is many times lower than what can be coupled using red laser light at 633 nm ($\sim 5 \text{ mW}$) since the lower wavelengths are more prone to scattering.

The same optical fiber was coupled to four different devices while the intensity of the output light from another coupled fiber was measured. The total loss through the four devices was found to be -63.84 dB, -65.54 dB, -64.7 dB and -65.69 dB for an average of -64.94 dB. It is interesting to note that the loss from all four devices was essentially the same. This suggests that the roughness from the facets averages out to be about the same loss even if the exact pattern of the roughness is different.

With the total loss determined, we can now add up all of the loss mechanisms through the device and estimate the effect which facet roughness plays in the overall picture. Table 4.1 gives a complete overview of the different sources of loss through the device.

Table 4.1: Power budget through the device.

Mechanism	Loss
Reflection	0.73 dB
Divergence	0.044 dB
ITO Absorption	0.087 dB
Waveguide Loss	25.38 dB
<i>Facet Roughness</i>	<i>38.67 dB</i>
TOTAL	64.94 dB

When adding up all of the loss mechanisms previously calculated, the loss due to the facet roughness can be approximated to be about 38.67 dB making it the most lossy component of the device. A loss of 64.94 dB translates to an output optical power of about 30 pW. This collected power is sufficient when using an integration time of 50 ms at the detector. It is important to compare the intensity of the output to the noise of the detector. As will be seen in the proceeding section, the noise from the

measured intensity using the USB2000 spectrophotometer is very low compared to the signal intensity leading to a relatively high signal to noise ratio.

4.2.3 Preliminary Optical Testing

The USB2000 device collects light at all visible wavelengths and displays the intensity vs. the wavelength. To take the absorbance measurements, we analyzed the intensity only at 472 nm over time to determine the change in intensity and thus calculate the absorbance. Figure 4.8 shows an example of the collected data.

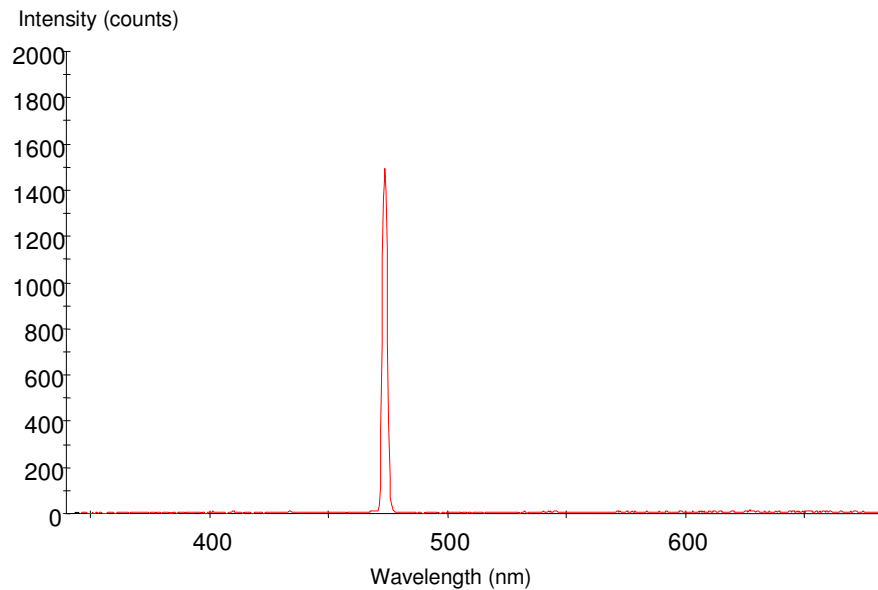


Figure 4.8: Intensity of the blue laser is shown as a clear peak with a narrow spectral width centered at 472 nm.

The computer software was used to analyze the change in intensity at the peak of the emission and plot this change over time. This is the procedure used for every time resolved intensity measurement taken for this experiment.

Typically, all laser sources have some sort of drift associated with the output intensity due to numerous possible effects such as heating of the semiconductor.

Noise in the output can be attributed to either spontaneous emission or shot noise caused by electron-hole recombination. It is important to know how much the laser drift will affect the measured intensity over time during the absorbance measurements and whether or not the noise is high enough to be a concern. Figure 4.9 shows the intensity results for the laser coupled through the device directly after the laser has been turned on and for one hour afterward.

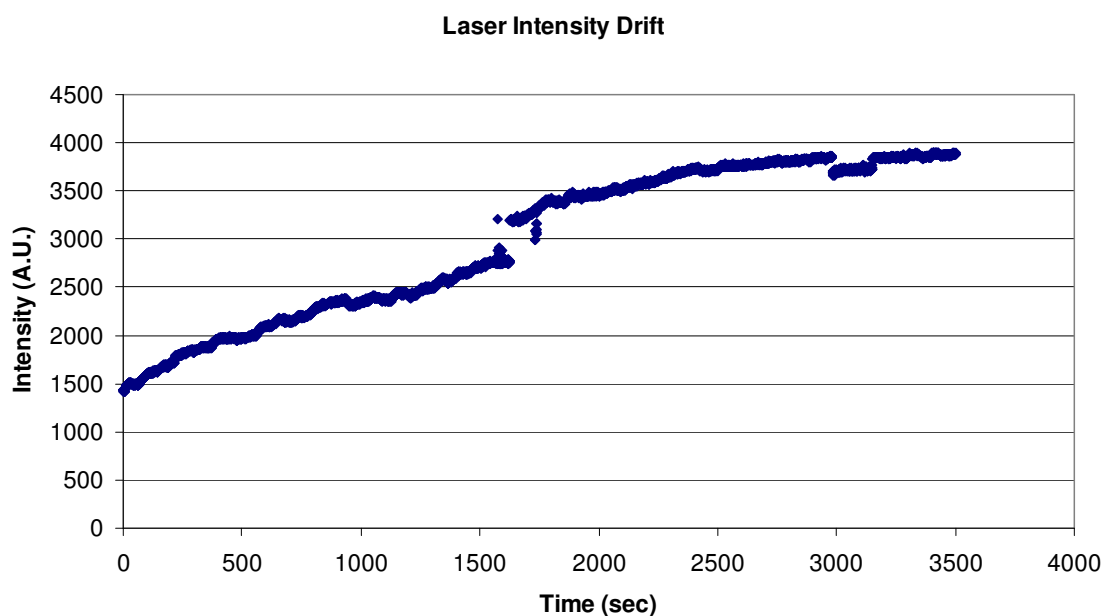


Figure 4.9: Intensity of laser over one hour period after laser has been switched on.

The datasheet provided with the laser source describes the warm up time for the laser as being only 15 minutes. However, I determined it to be much longer as shown in the figure. The laser intensity drifts upward almost for a full hour after being turned on. This is consistent with the assumption that the laser is heating up while operating. After about 55 minutes, the intensity appears to level out with very minor fluctuations. Considering that the absorbance measurement with the device for our lowest measured concentration of 1 mM is expected to cause intensity changes on

the order of about 500 A.U. over a 10 minute timeframe, the drift displayed here is far enough below this value. Signal to noise ratio is estimated to be about 26 dB. Attempting to measure intensity changes for concentrations much smaller than 1 mM will have a reduced S/N ratio.

Another consideration to test was whether the unoxidized catechol molecules themselves contributed any change to the optical absorbance at 472 nm. If they did, then the final absorbance measurements may not only be due to the accumulated *o*-quinones on the chitosan, but also to the catechol molecules themselves in the solution. A flow test was performed using buffer solution without catechol, and then with buffer solution containing 0.1 M catechol. The liquids were administered at a flow rate of 100 $\mu\text{l/hr}$ and the results are displayed in figure 4.10.

The intensity is steady before any liquids have been administered then nearly doubles the moment buffer solution fills the channel. This is due to the fact that the solution has a higher index of refraction (1.33) than the air (~ 1) and is more closely matched to the SU-8 index, thus there is less refraction of the light as it leaves the waveguide and enters the microfluidic channel.

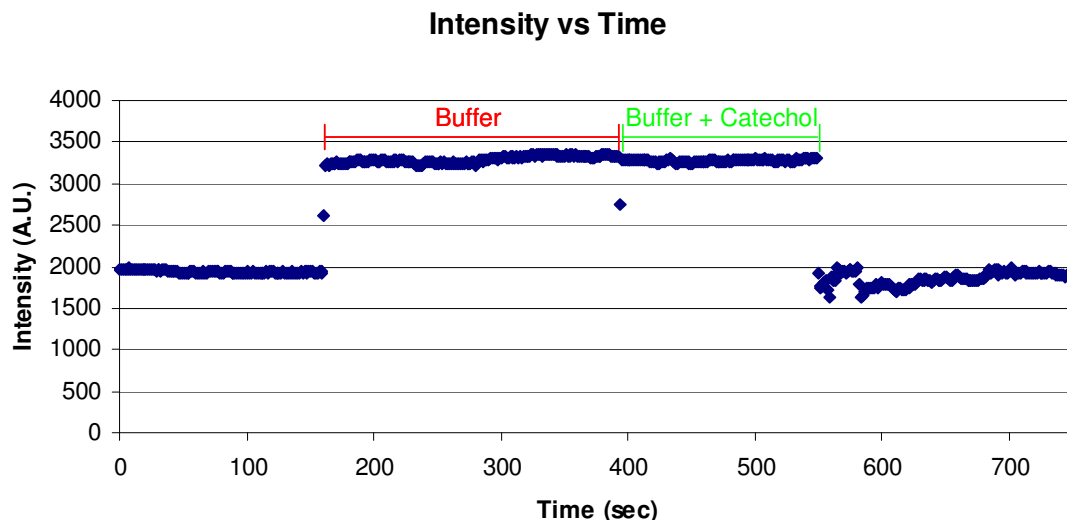


Figure 4.10: Measured intensity through device showing no difference between buffer solutions with and without catechol.

The measured intensity shows no noticeable change between the buffer solution and the solution containing a high concentration of catechol. This suggests that the catechol molecules themselves do not cause any absorbance change and that the change is entirely due to the generated *o*-quinones upon catechol oxidation. When air is pumped back through the channel, the intensity returns to its original value of 2000.

4.2.4 Catechol Detection Results

Concentrations of 100, 10 and 1 mM catechol were prepared in buffer solution for performing the tests with the MEMS sensor. The concentrations vary by an order of magnitude each to demonstrate the large dynamic sensing range of the device. Each sample was administered at a flow rate of 100 $\mu\text{l/hr}$ while an oxidizing current of 0.35 μA was applied to the electrodes in order to achieve a current density of 4 A/m^2 . The intensity of the output light was monitored over a 10 minute period

starting after the current is turned on. The absorbance was calculated by taking the log of the difference in intensity and the results are shown in figure 4.11.

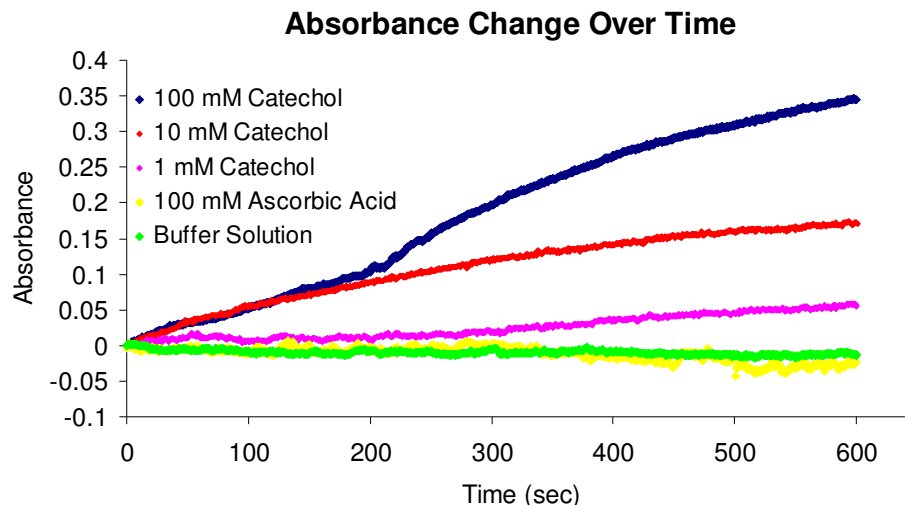


Figure 4.11: Absorbance over time results for various catechol concentrations and control solutions.

It is clear that the absorbance is greater for higher concentrations of catechol. The absorbance for the solutions containing catechol appears to rise at the same rate for the first 30 seconds. This could be due to the fact that the catechol is concentrated at the vicinity of the anode initially, but over time, the catechol must diffuse through the chitosan matrix to reach the anode in order to be oxidized. This diffusion rate and the amount that will then reach the anode over time are directly related to the concentration of the diffusing species. In these experiments two different control solutions were used. Buffer solution without catechol present displays no appreciable absorbance change over the 10 minute time span. Likewise, a high concentration (100 mM) of ascorbic acid also displays no measurable absorbance change. The pH of the ascorbic acid solution was adjusted using droplets of NaOH since its high acidity could potentially degrade the chitosan matrix. The ascorbic acid is easily oxidized by

the electrochemical reaction, but the reduced state does not contribute to any change in absorbance in the visible range of the spectrum. This selectivity is important for samples which may contain other easily oxidized species along with the catechol. However mixtures of numerous compounds with different oxidation potentials may not all oxidize at the same rate. This involves future work that needs to be performed with the device and is covered in more detail in the final chapter of this thesis.

The overall decrease in laser intensity after 10 minutes of oxidation is displayed in a bar graph in figure 4.12. Data is shown from experiments both with and without the chitosan film in the channel. The intensity change is clearly much higher in the experiments with the chitosan film. The control solutions are unaffected by the presence of the chitosan.

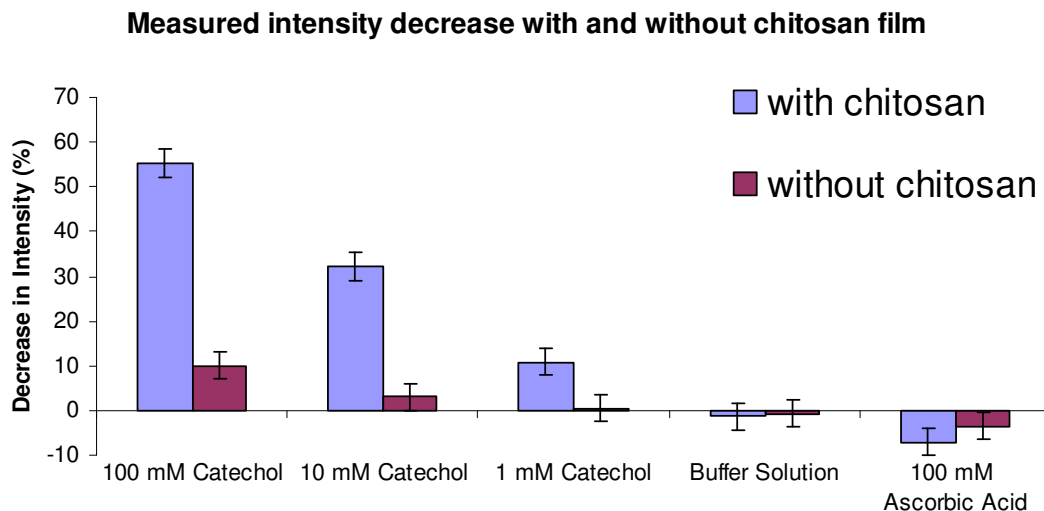


Figure 4.12: Decrease in laser intensity after 10 minute oxidation reaction. Note the difference chitosan makes for the catechol solutions while the control solutions are unaffected.

The slight increase in intensity for the control solutions is most likely due to laser drift. The error bars from both figures 4.10 and 4.11 were calculated based on the noise variations of the laser and detector. The absorbance calculated using the

MEMS sensor does not display the same linear relationship with catechol concentration that the slide experiments showed. Figure 4.13 demonstrates the seemingly logarithmic relationship between absorbance and measured concentration after the same amount of time. This discrepancy is discussed in more detail in the next chapter.

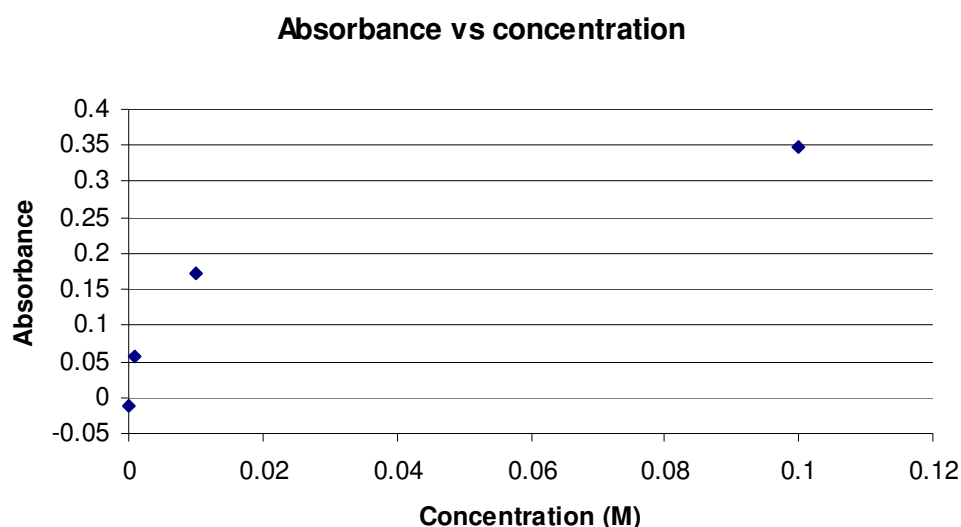


Figure 4.13: Absorbance vs. concentration plot displaying the non-linear relationship between the two.

For the experiments without the chitosan film in the channel, catechol is oxidized at the bare electrode and the *o*-quinones are left to float in the solution between the waveguides. This is done to illustrate the absorbance increase facilitated by the chitosan film.

In order to measure any appreciable change in the output intensity due to the generated *o*-quinones, the liquid flow must be halted while the current is being applied to the bare electrodes. Any applied flow rate will sweep away the *o*-quinones and no accumulation between the waveguides can occur in the channel.

The measurements taken without the chitosan film were highly repeatable as demonstrated in figure 4.14. The same current is applied throughout while the flow rate alternates between 100 $\mu\text{L/hr}$ and being turned off completely. During the times when the flow is off, the intensity drops due to the accumulation of the *o*-quinones. The intensity decreases exponentially and then approaches a steady state. This leveling off is most likely due to an equilibrium being reached between the generation of the *o*-quinones at the anode, and their diffusion away from the sensing area.

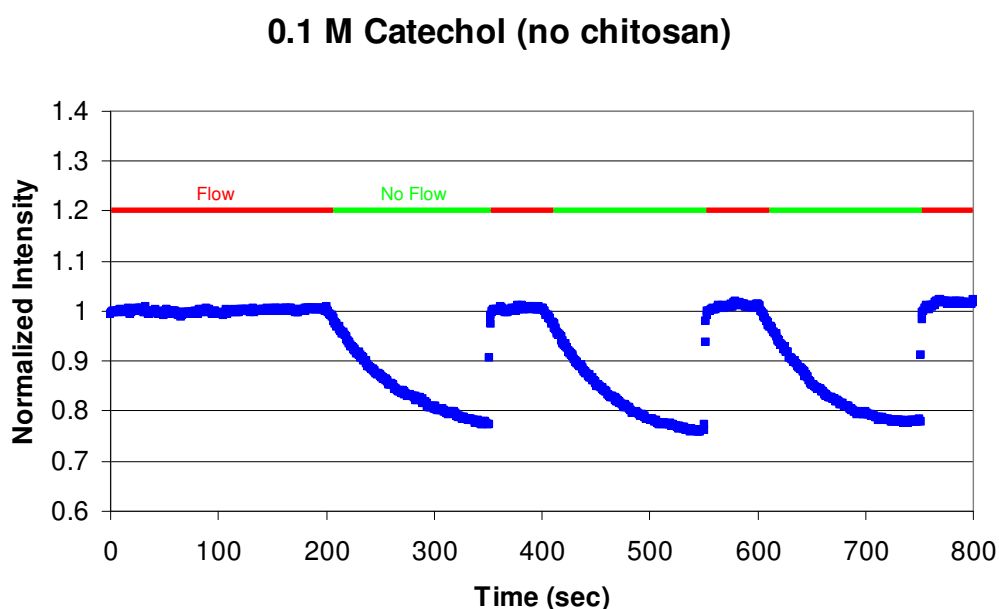


Figure 4.14: Intensity change from the oxidation of 0.1 M catechol in the absence of chitosan. The detection displays high repeatability.

The repeatable measurements suggest that the catechol is dissolved evenly throughout the buffer solution and that the rate of the oxidation reaction itself does not change appreciably from trial to trial. Once again, the stability of the optical measurements is demonstrated as the intensity returns to its original position instantly after the flow has swept the *o*-quinones away.

Figure 4.15 shows the absorbance measurements over time for the same three concentrations of catechol, and with using a slightly higher applied current of 1 μA in order to see the absorbance increase more clearly. Each absorbance saturates after only 100 seconds, and the final value is much less than that obtained from the experiments which not only used the chitosan film but a lower applied current as well. Also, 1 mM of catechol displays no measurable absorbance change in the absence of the chitosan film. The chitosan is thus necessary in order to measure lower concentrations of catechol with these devices.

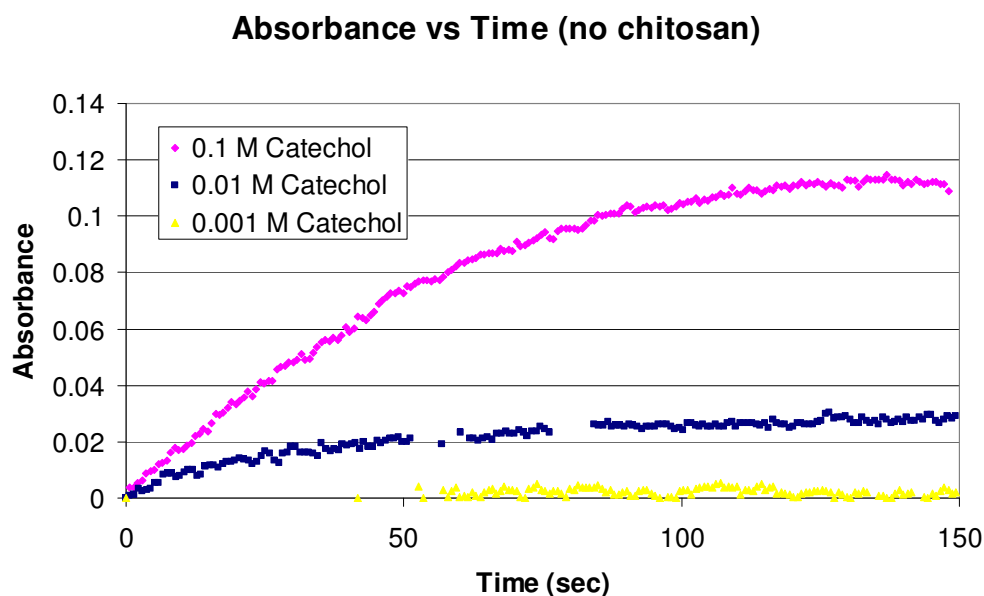


Figure 4.15: Absorbance over time using devices without the chitosan film for various catechol concentrations.

5 Discussion

This chapter will take a closer look at the data obtained with the MEMS sensor and compare it with the data from the slide experiments. Furthermore, a brief overview of how this sensor fits into the current sensing technology for phenols such as catechol will be discussed.

5.1 Data Discrepancies

5.1.1 Electrode Area Variations

As demonstrated from the plotted data in figures 4.5 and 4.12, the absorbance varies linearly with concentration in the slide experiments but does not when using the MEMS sensor. This is most likely due to the inherent variations which exist between devices relating to the size of the electrode surface areas. A transparency mask is used for patterning the gold electrodes, and this makes it very difficult to align the electrodes in exactly the same place for every device on the wafer. Due to this alignment issue, the electrode size in the channel can vary slightly from device to device. Furthermore, the sidewall roughness of the SU-8 which is covered with ITO is not known and the surface area can only be approximated based on the height and width of the ITO section.

These variations in the surface area impact the device performance in two major ways. First, the chitosan deposition rate will vary resulting in slightly different thicknesses of chitosan for each device. Second, the oxidation rate of the catechol will change if the surface area of the anode and cathode exposed to the solution is

different. The thickness of chitosan may have an effect on the diffusion rates of the catechol since the molecules must spend more time diffusing through a thicker polymer matrix. Further optimization of the fabrication procedure can help to reduce this variability, and the future work section in the next chapter offers some suggestions of design changes that may help to achieve more repeatable results.

5.1.2 Flow Rate Dependence

Another important difference between the slide experiments and those performed with the MEMS sensor is the addition of a flow rate of the catechol solution past the electrodes in the MEMS device. The solution was stagnant around the electrodes for the slide experiments which may have allowed for greater *o*-quinone attachment to the chitosan amine groups over a certain period of time. A flow rate was used for the MEMS device in order to continuously supply the sensing area of the channel with fresh catechol solution since the path length for diffusion is greatly restricted in the microfluidic channel. However, the flow rate may also be sweeping the catechol molecules too quickly past the electrodes, preventing a significant portion from oxidizing. The extreme of this effect is noticed when no chitosan is present in the channel and the flow rate actually has to be stopped in order for an appreciable absorbance change as seen from figure 4.13. It is then possible that by varying the flow rate, the rate of oxidation and *o*-quinone production can be changed as well. Lower flow rates may allow for the detection of lower concentrations of catechol.

A possible way to examine this effect more closely would be to apply some flow rate to a catechol solution and periodically stop the flow and start it again after a

set amount of time. The rate of absorbance change should increase during the moments when no flow is occurring and different flow rates could be applied at different times to try to correlate the flow rate with oxidation rate.

5.1.3 Metal Contamination

For some of the experiments, the chitosan films were neutralized with NaOH in a small container lined with aluminum foil. An interesting effect was noticed for those specific films that were neutralized in the aluminum foil containers. The absorbance spectra shown in figure 5.1 was measured through a chitosan film exposed to the aluminum foil using a non-exposed chitosan film as a baseline. The absorbance increases noticeably in the UV and near UV range, similar to the effect that the *o*-quinones have when attached to the chitosan. This change is attributed to either aluminum that may have become imbedded in the chitosan matrix during the neutralization process or some sort of chemical reaction between the aluminum and the NaOH. This result could potentially lead to the use of similar devices to the one described in this thesis for the detection of metal contaminants in liquids.

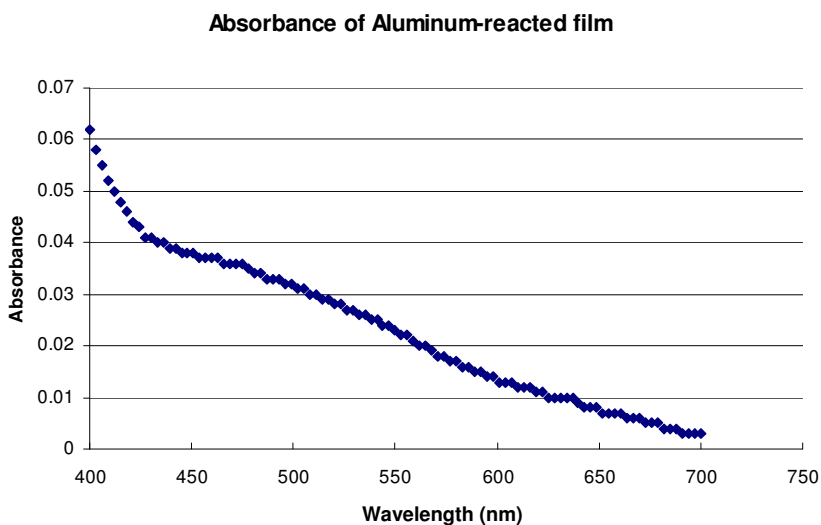


Figure 5.1: Absorbance spectra for a chitosan film neutralized in the presence of aluminum foil.

5.2 Sensor Comparison

The MEMS sensor described in this thesis has some definite advantages compared to other reported sensors for catechol detection. It has drawbacks as well, although these drawbacks are not necessarily inherent to the method used and could be overcome with further research into particular aspects of the device.

Typical electrochemical sensors are capable of detecting extremely low concentrations of catechol in the nanomolar range and also boast fast response times usually less than 15 seconds [25, 27]. In order to achieve selectivity, these sensors make use of enzymes entrapped in an immobilization matrix over the working electrode which will only oxidize phenolic compounds. One issue with these sensors is that the enzymatic activity degrades over time which can make them very difficult to calibrate and it means they must be used soon after the enzymes are entrapped. Also, the enzymatic activity is very sensitive to any changes in the pH of the solution. Our reported device does not suffer from these problems because it does not need the enzymes in order to be selective. It achieves selectivity through the use of optical absorbance measurements as opposed to current measurements.

The use of optical absorbance measurements for catechol detection has been reported, but these sensors are not integrated into an on-chip device and thus are inherently a laboratory-based procedure [33]. These reported sensors including the experiments found in [30] are very similar to the slide experiments performed in this work and require very little if any actual fabrication. The advantage of our device is that it can be packaged into a portable system capable of performing on-site analysis of very low sample volumes. Since our device uniquely allows for the collection of

time-resolved absorbance data, calibration curves can be fit to different times in order to achieve more accurate sensing of the concentration. The catechol concentrations measured from these reported sensors are not much lower than our lowest measured concentration, and in fact, they also demonstrate a non-linear response for concentrations above about 10 mM. At high concentrations, strong electrostatic interactions occur between molecules and this may cause the observed deviation from a linear relationship between absorbance and concentration [1].

6 Conclusion & Future Work

This thesis presents the design, fabrication and testing of a MEMS sensor utilizing optical measurements for the detection of the harmful phenol, catechol. The biophotonics platform has evolved over the years and has reached the point of becoming a fully sealed and packaged device. Many changes were made to the original design to meet the needs for the absorbance measurements and for the encapsulation of the microfluidic channel. The power budget was broken down to understand all the sources of optical loss through the device and the fabrication procedure was improved in order to avoid delamination problems with the SU-8 material. The results obtained from test chips demonstrated the need for changing the electrode design in the channel to decrease the amount of chitosan away from the ITO sidewall. The sidewall deposition of chitosan was analyzed using SEM imaging to find the optimal deposition conditions. This work then demonstrated the dynamic detection range of the MEMS sensor by detecting catechol concentrations ranging from 100 to 1 mM with a distinct increase in absorbance change for higher concentrations. Control solutions such as buffer and ascorbic acid contributed no absorbance change, demonstrating the selectivity of the device. Finally, an analysis of the sensor data as compared to data obtained with more traditional absorbance detection techniques was used to understand and explain discrepancies. To the best of our knowledge, this device is the first demonstration of catechol detection using optical measurements on-chip.

While the measured data is a great first step in demonstrating the usefulness of an optical sensor for on-chip catechol detection, there is further work that can be done

to improve on what has been accomplished. Improving the variations between devices should be the primary goal. Using chrome masks for patterning the gold and ITO sections would help in reducing the size variability of the electrodes in the channel. A more useful approach would be an altered design in which the chitosan film is deposited on a planar surface and thin waveguides no thicker than 2 μm are used to couple the light through the device. A schematic of this alternate design is shown in figure 6.1.

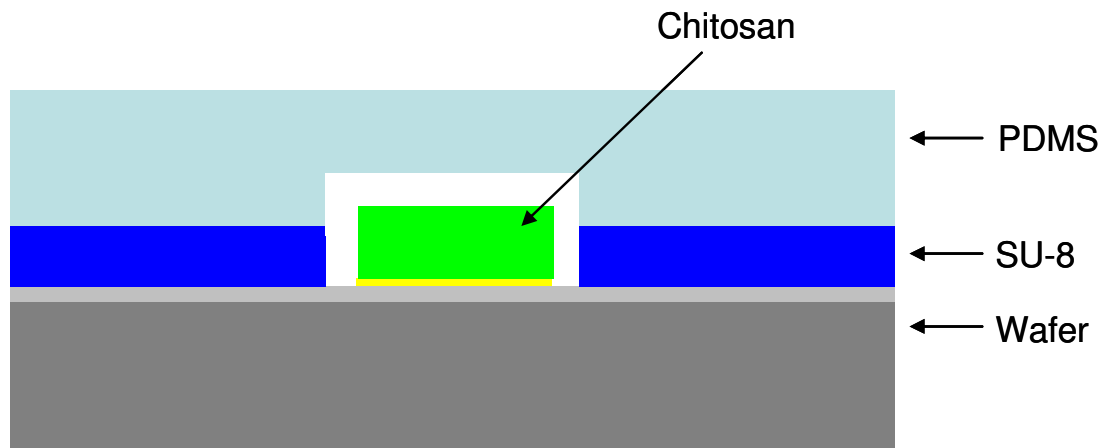


Figure 6.1: Cross section of alternate device design to reduce device variability.

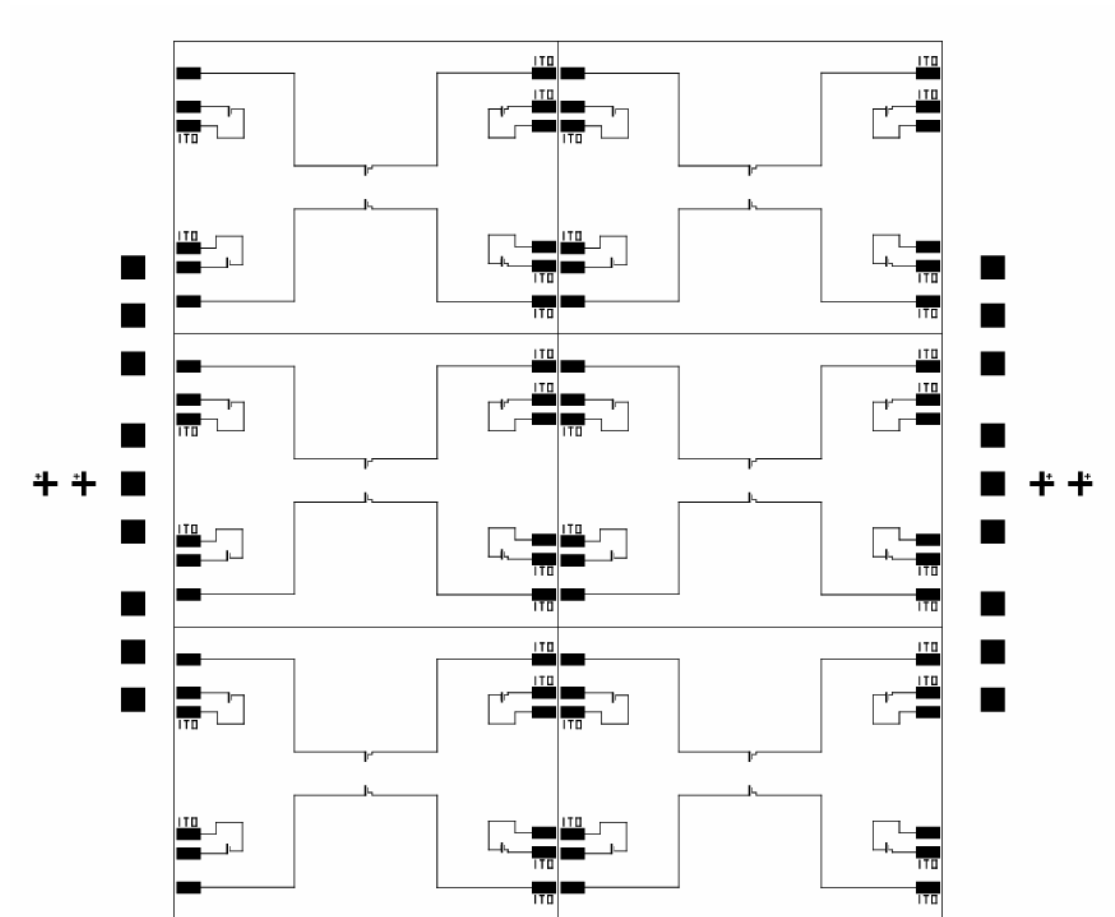
In this design, the PDMS capping layer is patterned to create the other half of the microfluidic channel and chitosan is deposited on a single planar electrode in the middle of the channel. Tapered fibers can be used to couple the light to and from the thin SU-8 waveguides. The electrode size does not vary with this design and the thickness of chitosan is always constant from device to device since it is much easier to control the thickness when using a planar electrode than when trying the deposit the chitosan on a sidewall.

Another area that would benefit from further research includes the effect that flow rate has on the catechol oxidation rate. Also, the device could be used for the detection of other phenol types besides catechol. Most oxidized phenols demonstrate some level of absorbance near the UV range so the methodology used in this work is not limited to the detection of catechol only.

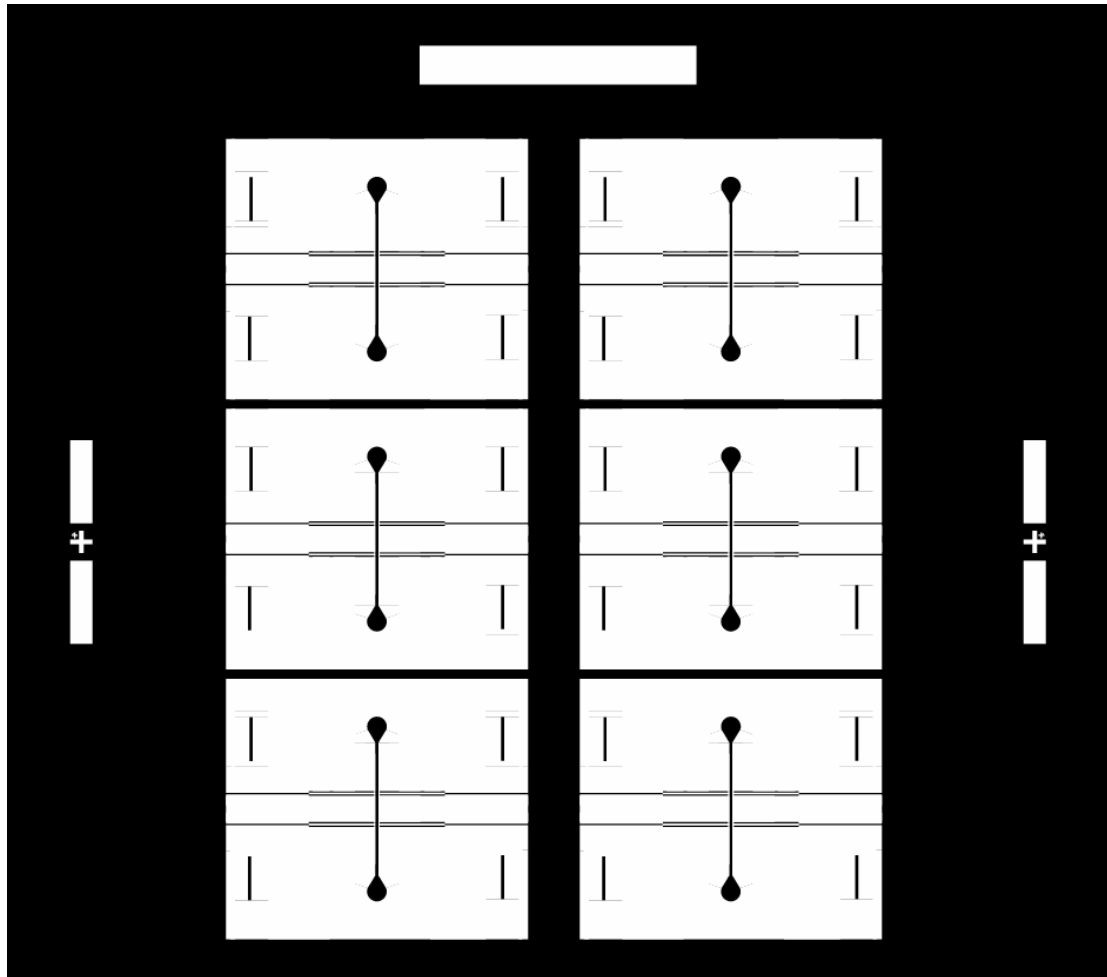
The choice of materials for the fabrication of the device was made partly to allow for the future integration of on-chip photodetectors thus removing the need for coupling the output light into an off-chip detector. This addition would help bring the device even closer to being a fully self-sufficient lab-on-a-chip system. Hopefully, the work detailed in this thesis can contribute to providing the groundwork for the development of the next generation of portable, efficient catechol sensors.

APPENDIX

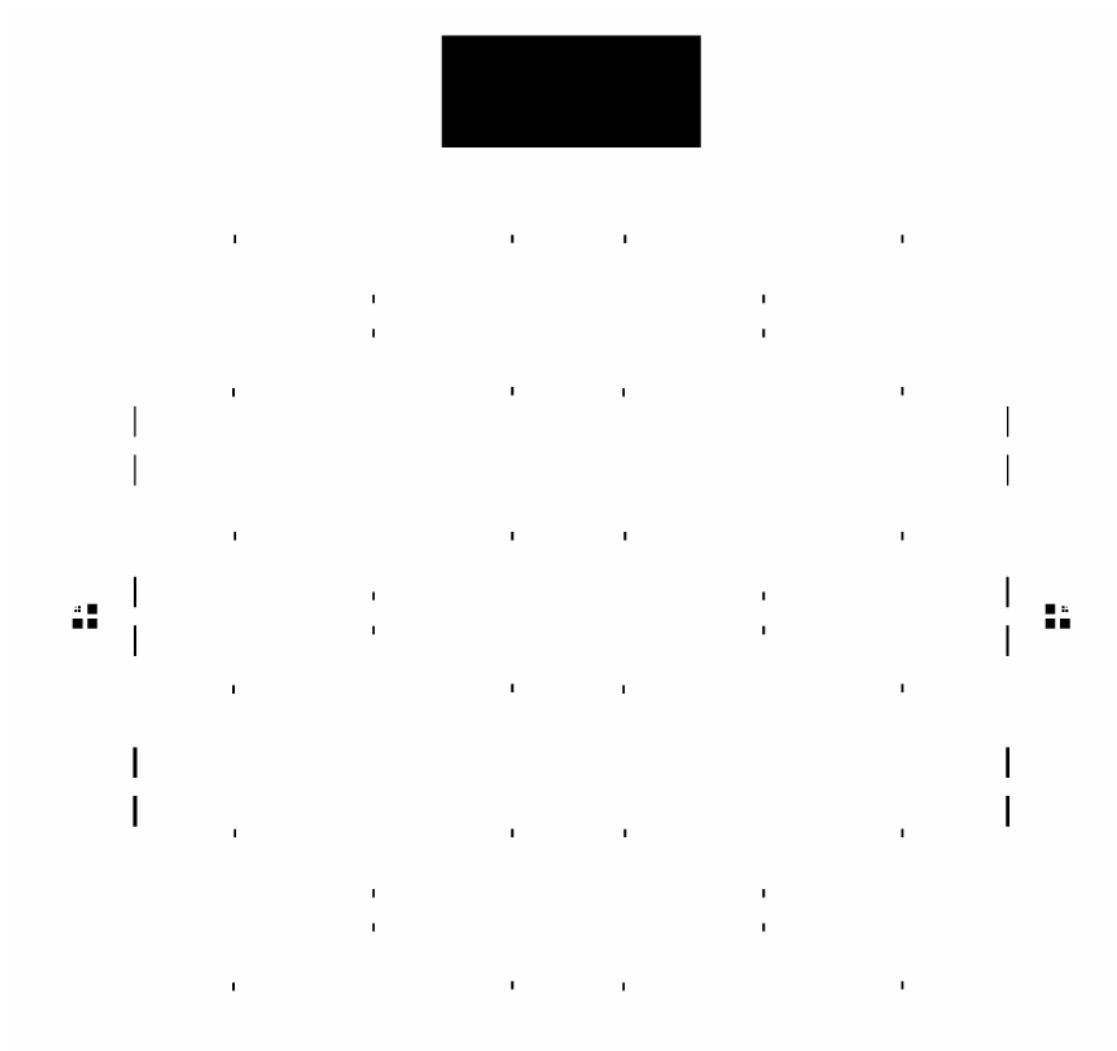
Mask #1 (Gold Mask)



Mask #2 (SU-8 Mask)



Mask #3 (ITO Mask)



REFERENCES

- [1] J. R. Lakowicz, *Principles of Fluorescence Spectroscopy*. New York: Plenum Press, 1983.
- [2] D. Davalos, J. K. Lee, W. B. Smith, B. Brinkman, M. H. Ellisman, B. Zheng, and K. Akassoglou, "Stable in vivo imaging of densely populated glia, axons and blood vessels in the mouse spinal cord using two-photon microscopy," *Journal of Neuroscience Methods*, vol. 169, pp. 1-7, 2008.
- [3] J. W. Lichtman and J.-A. Conchello, "Fluorescence Microscopy," *Nature Methods*, vol. 2, pp. 910-919, 2005.
- [4] N. Panchuk-Voloshina, R. P. Haugland, and J. Bishop-Stewart, "Alexa dyes, a series of new fluorescent dyes that yield exceptionally bright, photostable conjugates," *Journal of Histochemistry and Cytochemistry*, vol. 47, pp. 1179-1188, 1999.
- [5] S. Y. Nishimura, S. J. Lord, L. O. Klein, K. A. Willets, M. He, Z. Lu, R. J. Twieg, and W. E. Moerner, "Diffusion of Lipid-like Single-Molecule Fluorophores in the Cell Membrane," *Journal of Physical Chemistry B*, vol. 110, pp. 8151-8157, 2006.
- [6] L. Shang, C. Qin, T. Wang, M. Wang, L. Wang, and S. Dong, "Fluorescent Conjugated Polymer-Stabilized Gold Nanoparticles for Sensitive and Selective Detection of Cysteine," *Journal of Physical Chemistry C*, vol. 111, pp. 13414-13417, 2007.
- [7] B.-S. Lee, J.-G. Lee, D.-H. Shin, and Eun-Kikim, "Statistical Optimization of Bioluminescence of *Photobacterium phosphoreum* KCTC2852," *Journal of Bioscience and Bioengineering*, vol. 92, pp. 72-76, 2001.
- [8] H. Jing-Zhi, et al., "The properties of firefly luciferase from *Luciola Chinesis* L," *Chinese Journal of Luminescence*, vol. 28, pp. 770-775, 2007.
- [9] D. Milton, "Quorum sensing in vibrios: complexity for diversification," *International Journal of Medical Microbiology*, vol. 296, pp. 61-71, 2006.
- [10] A. s. F. G. I. Barrios, R. Zuo, Y. Hashimoto, L. Yang, W. E. Bentley, and T. K. Wood, "Autoinducer 2 Controls Biofilm Formation in *Escherichia coli* through a Novel Motility Quorum-Sensing Regulator (MqsR, B3022)," *Journal of Bacteriology*, vol. 188, pp. 305-316, 2006.
- [11] P. N. Prasad, *Introduction to Biophotonics*. Hoboken, New Jersey: Wiley-Interscience, 2003.
- [12] R. Marrington, T. R. Dafforn, D. J. Halsall, and A. Rodger, "Micro-Volume Couette Flow Sample Orientation for Absorbance and Fluorescence Linear Dichroism," *Biophysical Journal*, vol. 87, pp. 2002-2012, 2004.
- [13] M. K. Sezgintürk and E. Dinçkaya, "An amperometric inhibitor biosensor for the determination of reduced glutathione (GSH) without any derivatization in some plants," *Biosensors and Bioelectronics*, vol. 19, pp. 835-841, 2004.
- [14] L. Zhao, D. Wu, L.-F. Wu, and T. Song, "A simple and accurate method for quantification of magnetosomes in magnetotactic bacteria by common spectrophotometer," *Biochemical and Biophysical Methods*, vol. 70, pp. 377-383, 2007.

- [15] M. Luther, J. Parry, J. Moore, J. Meng, Y. Zhang, Z. Cheng, and L. Yu, "Inhibitory effect of Chardonnay and black raspberry seed extracts on lipid oxidation in fish oil and their radical scavenging and antimicrobial properties," *Food Chemistry*, vol. 104, pp. 1065-1073, 2007.
- [16] T. N. McCaig, D. Y. K. Fenn, R. E. Knox, R. M. DePauw, J. M. Clarke, and J. G. McLeod, "Measuring polyphenol oxidase activity in a wheat breeding program," *Canadian Journal of Plant Science*, pp. 507-514, 1999.
- [17] L. Su, J.-J. Yin, D. Charles, K. Zhou, J. Moore, and L. Yu, "Total phenolic contents, chelating capacities, and radical-scavenging properties of black peppercorn, nutmeg, rosehip, cinnamon and oregano leaf," *Food Chemistry*, vol. 100, pp. 990-997, 2005.
- [18] K. Zhou, J.-J. Yin, and L. Yu, "ESR determination of the reactions between selected phenolic acids and free radicals or transition metals," *Food Chemistry*, vol. 95, pp. 446-457, 2006.
- [19] Liangli Yu, *Private Communication*
- [20] C. T. Jung, R. R. Wickett, P. B. Desai, and R. L. Bronaugh, "In vitro and in vivo percutaneous absorption of catechol," *Food and Chemical Toxicology*, vol. 41, pp. 885-895, 2003.
- [21] A. Starek, "Estrogens and Organochlorine Xenoestrogens and Breast Cancer Risk," *International Journal of Occupational Medicine and Environmental Health*, vol. 16, pp. 113-124, 2003.
- [22] D.-P. Yang, H.-F. Ji, G.-Y. Tang, W. Ren, and H.-Y. Zhang, "How Many Drugs Are Catecholics," *Molecules*, vol. 12, pp. 878-884, 2007.
- [23] R. W. Bosch, D. Feron, and J. P. Celis, *Electrochemistry in Light Water Reactors*: CRC Press, 2007.
- [24] D. J. G. Ives and G. J. Janz, *Reference Electrodes, Theory and Practice*. New York: Academic Press, 1961.
- [25] D. Shan, M. Zhu, E. Han, H. Xue, and S. Cosnier, "Calcium carbonate nanoparticles: A host matrix for the construction of highly sensitive amperometric phenol biosensor," *Biosensors and Bioelectronics*, vol. 23, pp. 648-654, 2007.
- [26] S. M. Strawbridge, S. J. Green, and J. H. R. Tucker, "Electrochemical detection of catechol and dopamine as their phenylboronate ester derivatives," *Chemistry Communication*, pp. 2393-2394, 2000.
- [27] J. K. Mbouguen, E. Ngameni, and A. Walcarius, "Quaternary ammonium functionalized clay film electrodes modified with polyphenol oxidase for the sensitive detection of catechol," *Biosensors and Bioelectronics*, vol. 23, pp. 269-275, 2007.
- [28] M. J. Schöning, M. Jacobs, A. Muck, D.-T. Knobbe, J. Wang, M. Chatrathi, and S. Spillmann, "Amperometric PDMS/glass capillary electrophoresis-based biosensor microchip for catechol and dopamine detection," *Sensors and Actuators B*, vol. 108, pp. 688-694, 2005.
- [29] V. Zucolotto, A. P. A. Pinto, T. Tumolo, M. L. Moraes, M. S. Baptista, A. Riul Jr., A. P. U. Araújo, and O. N. Oliveira Jr., "Catechol biosensing using a nanostructured layer-by-layer film containing Cl-catechol 1,2-dioxygenase," *Biosensors and Bioelectronics*, vol. 21, pp. 1320-1326, 2006.

- [30] G. F. Payne, M. V. Chaubal, and T. A. Barbari, "Enzyme-catalysed polymer modification: reaction of phenolic compounds with chitosan films," *Polymer*, vol. 37, pp. 4643-4648, 1996.
- [31] L.-Q. Wu, R. Ghodssi, Y. A. Elabd, and G. F. Payne, "Biomimetic Pattern Transfer," *Advanced Functional Materials*, vol. 15, pp. 189-195, 2005.
- [32] L.-Q. Wu, M. K. McDermott, C. Zhu, R. Ghodssi, and G. F. Payne, "Mimicking Biological Phenol Reaction Cascades to Confer Mechanical Function," *Advanced Functional Materials*, vol. 16, pp. 1967-1974, 2006.
- [33] J. Abdullah, M. Ahmad, L. Y. Heng, N. Karuppiyah, and H. Sidek, "An Optical Biosensor based on Immobilization of Laccase and MBTH in Stacked Films for the Detection of Catechol," *Sensors*, vol. 7, pp. 2238-2250, 2007.
- [34] J. Abdullah, M. Ahmad, N. Karuppiyah, L. Y. Heng, and H. Sidek, "Immobilization of tyrosinase in chitosan film for an optical detection of phenol," *Sensors and Actuators B*, vol. 114, pp. 604-609, 2006.
- [35] X. J. Wu, M. M. F. Choi, and X. M. Wu, "An organic-phase optical phenol biosensor coupling enzymatic oxidation with chemical reduction," *The Analyst*, vol. 129, pp. 1143-1149, 2004.
- [36] S. D. Senturia, *Microsystem Design*: Kluwar Academic Publishers, 2004.
- [37] M. Bozzetti, G. Calò, A. D'Orazio, M. D. Sario, L. Mescia, V. Petruzzelli, and F. Prudeniano, "Integrated Optical Sensor for Environment Monitoring," presented at International Conference on Transparent Optical Networks, Sousse, Tunisia, 2007.
- [38] R. Narayanaswamy, "Optical Sensors," presented at Asian Conference on Sensors and the International Conference on New Techniques in Pharmaceutical And Biomedical Research Proceedings, Kuala Lumpur, Malaysia, 2005.
- [39] S. Balslev, A. M. Jorgensen, B. Bilenberg, K. B. Mogensen, D. Snakenborg, O. Geschke, J. P. Kutter, and A. Kristensen, "Lab-on-a-chip with integrated optical transducers," *Lab on a Chip*, vol. 6, pp. 213-217, 2005.
- [40] D. Nilsson, S. Balslev, and A. Kristensen, "Polymer microcavity dye laser based on a single-mode SU-8 planar waveguide," *Solid State Lasers XIV*, vol. 5707, pp. 208-216, 2005.
- [41] Z. Li and D. Psaltis, "Optofluidic Distributed Feedback Dye Lasers," *IEEE Journal of Selected Topics in Quantum Electronics*, vol. 13, pp. 185-193, 2007.
- [42] L. Jiang and S. Pau, "Integrated waveguide with a microfluidic channel in spiral geometry for spectroscopic applications," *Applied Physics Letters*, vol. 90, 2007.
- [43] N. Siwak, X. Z. Fan, D. Hines, S. Kanakaraju, E. Williams, N. Goldsman, and R. Ghodssi, "Indium Phosphide MEMS Cantilever Resonator Sensors Utilizing a Pentacene Absorption Layer," *Journal of Microelectromechanical Systems (under review)*, 2008.
- [44] Z. Wang, A. Sekulovic, J. P. Kutter, D. D. Bang, and A. Wolff, "Towards a portable microchip system with integrated thermal control and polymer waveguides for real-time PCR," *Electrophoresis*, vol. 27, pp. 5051-5058, 2006.

- [45] M.-H. Wu, H. Cai, X. Xu, J. P. G. Urban, Z.-F. Cui, and Z. Cui, "A SU-8/PDMS Hybrid Microfluidic Device with Integrated Optical Fibers for Online Monitoring of Lactate," *Biomedical Microdevices*, vol. 7, pp. 323-329, 2005.
- [46] C. Liu, "Recent Developments in Polymer MEMS," *Advanced Materials*, vol. 19, pp. 3783-3790, 2007.
- [47] A. Borreman, S. Musa, A. A. M. Kok, M. B. J. Diemeer, and A. Driessen, "Fabrication of Polymeric Multimode Waveguides and Devices in SU-8 Photoresist Using Selective Polymerization," presented at IEEE/LEOS Symposium, Amsterdam, 2002.
- [48] J.-N. Kuo, C.-C. Hsieh, S.-Y. Yang, and G.-B. Lee, "An SU-8 microlens array fabricated by soft replica molding for cell counting applications," *Journal of Micromechanics and Microengineering*, vol. 17, pp. 693-699, 2007.
- [49] M. Nordström, D. A. Zauner, A. Boisen, and J. Hübner, "Single-Mode Waveguides With SU-8 Polymer Core and Cladding for MOEMS Applications," *Journal of Lightwave Technology*, vol. 25, pp. 1284-1289, 2007.
- [50] G. P. Agrawal, *Fiber-Optic Communication Systems*. New York: John Wiley & Sons, Inc., 2002.
- [51] M. Z. Hossain and M. Q. Huda, "Analytical study of erbium-doped silicon lasers," presented at 4th International Conference on Electrical and Computer Engineering, Dhaka, Bangladesh, 2006.
- [52] J. Toudert, S. Núñez-Sánchez, R. Serna, and M. J. d. Castro, "Enhanced photoluminescence of nanostructured Er³⁺-doped a-Si/a-Al₂O₃ thin films prepared by PLD," *Materials Science and Engineering B*, vol. 146, pp. 141-145, 2008.
- [53] N. G. Portney and M. Ozkan, "Nano-oncology: drug delivery, imaging, and sensing," *Analytical and Bioanalytical Chemistry*, vol. 384, pp. 620-630, 2006.
- [54] X.-X. Zhu, et al., "Optical encoding of microbeads based on silica particle encapsulated quantum dots and its applications," *Nanotechnology*, vol. 19, pp. 1-8, 2008.
- [55] N. Nashida, W. Satoh, J. Fukuda, and H. Suzuki, "Electrochemical immunoassay on a microfluidic device with sequential injection and flushing functions," *Biosensors and Bioelectronics*, vol. 22, pp. 3167-3173, 2007.
- [56] L. Wang, L. Flanagan, and A. P. Lee, "Side-Wall Vertical Electrodes for Lateral Field Microfluidic Applications," *Journal of Microelectromechanical Systems*, vol. 16, pp. 454-461, 2007.
- [57] R. Osellame, V. Maselli, R. M. Vazquez, R. Ramponi, and G. Cerullo, "Integration of optical waveguides and microfluidic channels both fabricated by femtosecond laser irradiation," *Applied Physics Letters*, 2007.
- [58] J. Vieillard, R. Mazurczyk, L.-L. Boum, A. Bouchard, Y. Chevolot, P. Cremillieu, B. Hannes, and S. Krawczyk, "Integrated microfluidic-microoptical systems fabricated by dry etching of soda-lime glass," *Microelectronic Engineering*, vol. 85, pp. 465-469, 2008.
- [59] S. K. Sia and G. M. Whitesides, "Microfluidic devices fabricated in poly(dimethylsiloxane) for biological studies," *Electrophoresis*, vol. 24, pp. 3563-3576, 2003.

- [60] G. M. Whitesides and J. C. Love, "The art of building small," *Scientific American*, vol. 285, pp. 39-47, 2001.
- [61] J. M. K. Ng, I. Gitlin, A. D. Stroock, and G. M. Whitesides, "Components for integrated poly(dimethylsiloxane) microfluidic systems," *Electrophoresis*, vol. 23, pp. 3461-3473, 2002.
- [62] O. C. Jeong and S. S. Yang, "Fabrication and test of a thermopneumatic micropump with a corrugated p+ diaphragm," *Sensors and Actuators A*, vol. 83, pp. 249-255, 2000.
- [63] M. Koch, N. Harris, A. G. R. Evans, N. M. White, and A. Brunnschweiler, "A novel micromachined pump based on thick-film piezoelectric actuation," *Sensors and Actuators A*, vol. 70, pp. 98-103, 1998.
- [64] R. Zengerle, J. Ulrich, S. Kluge, M. Richter, and A. Richter, "A bidirectional silicon micropump," *Sensors and Actuators A*, vol. 50, pp. 81-86, 1995.
- [65] G. B. Pier, J. B. Lyczak, and L. M. Wetzler, *Immunology, Infection, and Immunity*: ASM Press, 2004.
- [66] L. J. Lucas, J.-H. Han, J. Chesler, and J.-Y. Yoon, "Latex immunoagglutination assay for a vasculitis marker in a microfluidic device using static light scattering detection," *Biosensors and Bioelectronics*, vol. 22, pp. 2216-2222, 2007.
- [67] Q. Ma, T.-Y. Song, X.-Y. Wang, Y.-B. Li, Y.-H. Shi, and X.-G. Su, "Quantum Dots as Fluorescent Labels for Use in Microsphere-Based Fluoroimmunoassays," *Spectroscopy Letters*, vol. 40, pp. 113-127, 2006.
- [68] K.-H. Lee, Y.-D. Sua, S.-J. Chena, F.-G. Tseng, and G.-B. Lee, "Microfluidic systems integrated with two-dimensional surface plasmon resonance phase imaging systems for microarray immunoassay," *Biosensors and Bioelectronics*, vol. 23, pp. 466-472, 2007.
- [69] F. Mizutani, "Biosensors utilizing monolayers on electrode surfaces," *Sensors and Actuators B*, vol. 130, pp. 14-20, 2007.
- [70] A. E. Pusateri, S. J. McCarthy, K. W. Gregory, R. A. Harris, L. Cardenas, A. T. McManus, and C. W. Goodwin, "Effect of a chitosan-based hemostatic dressing on blood loss and survival in a model of severe venous hemorrhage and hepatic injury in swine," *Journal of Trauma*, vol. 4, pp. 177-182, 2003.
- [71] I. Zhitomirsky and A. Hashambhoy, "Chitosan-mediated electrosynthesis of organic-inorganic nanocomposites," *Journal of Materials Processing Technology*, vol. 191, pp. 68-72, 2007.
- [72] H. Yi, L.-Q. Wu, W. E. Bentley, R. Ghodssi, G. W. Rubloff, J. N. Culver, and G. F. Payne, "Biofabrication with chitosan," *Biomacromolecules*, vol. 6, pp. 2881-2894, 2005.
- [73] J. C. Cheng and A. P. Pisano, "Photolithographic Process for Integration of the Biopolymer Chitosan Into Micro/Nanostructures," *Journal of Microelectricalmechanical Systems*, vol. 17, pp. 402-409, 2008.
- [74] I. Park, J. Cheng, A. P. Pisano, E.-S. Lee, and J.-H. Jeong, "Low temperature, low pressure nanoimprinting of chitosan as a biomaterial for bionanotechnology applications," *Applied Physics Letters*, vol. 90, 2007.

- [75] H. Yi, L.-Q. Wu, R. Ghodssi, G. W. Rubloff, G. F. Payne, and W. E. Bentley, "Signal-Directed Sequential Assembly of Biomolecules on Patterned Surfaces," *Langmuir*, vol. 21, pp. 2104-2107, 2005.
- [76] R. A. Zangmeister, J. J. Park, G. W. Rubloff, and M. J. Tarlov, "Electrochemical Study of chitosan films deposited from solution at reducing potentials," *Electrochimica Acta*, vol. 51, pp. 5324-5333, 2006.
- [77] S. T. Koev, M. A. Powers, H. Yi, L.-Q. Wu, W. E. Bentley, G. W. Rubloff, G. F. Payne, and R. Ghodssi, "Mechano-transduction of DNA hybridization and dopamine oxidation through electrodeposited chitosan network," *Lab on a Chip*, vol. 7, pp. 103-111, 2006.
- [78] X. Luo, A. T. Lewandowski, H. Yi, G. F. Payne, R. Ghodssi, W. E. Bentley, and G. W. Rubloff, "Programmable assembly of a metabolic pathway enzyme in a pre-packaged reusable bioMEMS device," *Lab on a Chip*, vol. 8, pp. 420-430, 2008.
- [79] J. J. Park, X. Luo, H. Yi, T. M. Valentine, G. F. Payne, W. E. Bentley, R. Ghodssi, and G. W. Rubloff, "Chitosan-mediated *in situ* biomolecule assembly in completely packaged microfluidic devices," *Lab on a Chip*, vol. 6, pp. 1315-1321, 2006.
- [80] A. T. Lewandowski, H. Yi, X. Luo, G. F. Payne, R. Ghodssi, G. W. Rubloff, and W. E. Bentley, "Protein Assembly Onto Patterned Microfabricated Devices Through Enzymatic Activation of Fusion Pro-Tag," *Biotechnology and Bioengineering*, vol. 99, pp. 499-507, 2007.
- [81] M. A. Powers, *Design, fabrication, and testing of a chitosan based optical biosensor*, Masters Thesis, University of Maryland, 2006
- [82] V. Badilita, I. Shamim, H. Yi, S. T. Koev, K. Gerasopoulos, and R. Ghodssi, "Chitosan-mediated biomems platform for optical sensing," presented at Transducers, Lyon, France, 2007.
- [83] M. A. Powers, et al., "A fabrication platform for electrically mediated optically active biofunctionalized sites in BioMEMS," *Lab on a Chip*, vol. 5, pp. 583-586, 2005.
- [84] C. L. Bliss, J. N. McMullin, and C. J. Backhouse, "Integrated wavelength-selective optical waveguides for microfluidic-based laser-induced fluorescence detection," *Lab on a Chip*, vol. 8, pp. 143-151, 2007.
- [85] T. C. Sum, A. A. Bettiol, J. A. van Kan, F. Watt, E. Y. B. Pun, and K. K. Tung, "Proton beam writing of low-loss polymer optical waveguides," *Applied Physics Letters*, vol. 83, pp. 1707-1709, 2003.
- [86] W.-S. Tsai, L.-Y. Chen, and W.-S. Wang, "Study of the Fabrication of BCB Waveguide Devices by Ultraviolet Pulsed-Laser Illumination," *IEEE Photonics Technology Letters*, vol. 20, pp. 84-86, 2008.
- [87] D. A. Zauner, A. M. Jorgensen, T. A. Anhoj, and J. Hübner, "High-density multimode integrated polymer optics," *Journal of Optics A: Pure and Applied Optics*, vol. 7, pp. 445-450, 2005.
- [88] Microchem Corp., "SU-8 Photoresist Product Line," http://www.microchem.com/products/su_eight.htm.

- [89] Dow Chemical Corp., "CYCLOTENE Advanced Electronics Resins," <http://www.dow.com/cyclotene/prod/402235.htm>
- [90] B. E. A. Saleh and M. C. Teich, *Fundamentals of Photonics*. New York: John Wiley & Sons, Inc., 1991.
- [91] M. Bass, et al., *Handbook of Optics, Fiber Optics and Nonlinear Optics*, vol. IV, 2nd ed. Boston: Mc-Graw Hill Professional, 2000.
- [92] Z.-g. Ling, K. Lian, and L. Jian, "Improved patterning quality of SU-8 microstructures by optimizing the exposure parameters," presented at SPIE: Advances in Resist Technology and Processing XVII, Santa Clara, CA, 2000.
- [93] G. Witzgall, R. Vrijen, E. Yablonovitch, V. Doan, and B. J. Schwartz, "Single-shot two-photon exposure of commercial photoresist for the production of three-dimensional structures," *Optics Letters*, vol. 23, pp. 1745-1747, 1998.
- [94] L. Martiradonna, T. Stomeo, L. Carbone, G. Morello, A. Salhi, M. D. Giorgi, R. Cingolani, and M. D. Vittorio, "Nanopositioning of colloidal nanocrystal emitters by means of photolithography and e-beam lithography," *Physica Status Solidi*, vol. 243, pp. 3972-3975, 2006.
- [95] J. Pfitzner, "Poiseuille and his law," *Anaesthesia*, vol. 31, pp. 273-275, 1976.
- [96] R. Lu, Z. Ge, Q. Hong, and S.-T. Wu, "Transflective In-Plane Switching Liquid Crystal Display," *Journal of Display Technology*, vol. 3, pp. 15-21, 2007.
- [97] J.-M. Moon, et al., "Enhancement of hole injection using ozone treated Ag nanodots dispersed on indium tin oxide anode for organic light emitting diodes," *Applied Physics Letters*, vol. 90, 2007.
- [98] I. Zudans, et al., "Electrochemical and optical evaluation of noble metal- and carbon-ITO hybrid optically transparent electrodes," *Journal of Electroanalytical Chemistry*, vol. 565, pp. 311-320, 2003.
- [99] S. Jiguet, M. Judelewicz, S. Mischler, A. Bertch, and P. Renaud, "Effect of filler behavior on nanocomposite SU8 photoresist for moving micro-parts," *Microelectronic Engineering*, vol. 83, pp. 1273-1276, 2006.
- [100] R. Fernandez, L.-Q. Wu, T. Chen, H. Yi, G. W. Rubloff, R. Ghodssi, W. E. Bentley, and G. F. Payne, "Electrochemically Induced Deposition of a Polysaccharide Hydrogel onto a Patterned Surface," *Langmuir*, vol. 19, pp. 4058-4062, 2003.